Optimalisaties van een biosensorplatform met ringresonatoren voor toepassingen in DNA-detectie

Optimizations of a Ring Resonator Biosensor Platform for Applications in DNA Detection

Sam Werquin

Promotoren: prof. dr. ir. P. Bienstman, prof. dr. P. Dubruel
Proefschrift ingediend tot het behalen van de graad van
Doctor in de Ingenieurswetenschappen: Fotonica

Vakgroep Informatietechnologie
Voorzitter: prof. dr. ir. D. De Zutter
Faculteit Ingenieurswetenschappen en Architectuur
Academiejaar 2014 - 2015

UNIVERSITEIT GENT

ISBN 978-90-8578-760-0
NUR 959, 954
Wettelijk depot: D/2015/10.500/4

Promotoren :

Prof. dr. ir. Peter Bienstman
Prof. dr. Peter Dubruel

Examencommissie :

Prof. dr. ir. R. Van de Walle (voorzitter)	Universiteit Gent, ELIS
Prof. dr. ir. Peter Bienstman (promotor)	Universiteit Gent, INTEC
Prof. dr. ir. F. Beunis (secretaris)	Universiteit Gent, ELIS
Dr. ir. T. Claes	imec
Prof. dr. P. Dubruel (promotor)	Universiteit Gent, Organische Chemie
Prof. dr. J. García-Rupérez	Universidad Politécnica de Valencia
Prof. dr. ir. N. Le Thomas	Universiteit Gent, INTEC

Universiteit Gent
Faculteit Ingenieurswetenschappen en Architectuur

Vakgroep Informatietechnologie
Sint-Pietersnieuwstraat 41, B-9000 Gent, België

Tel. : +32-9-264.89.33
Fax. : +32-9-331.35.93

Dit werk kwam tot stand in het kader van een beurs van
het Bijzonder Onderzoeksfonds (BOF) van de
Universiteit Gent.

Dankwoord

Het afronden van dit doctoraatsonderzoek biedt een uitgelezen kans om alle mensen te bedanken die me op verschillende manieren geholpen hebben tijdens de voorbije jaren.

In de eerste plaats wil ik mijn promotor Peter Bienstman bedanken. Bedankt om me na mijn master-thesis de kans te geven een doctoraatsonderzoek te starten. Tijdens mijn onderzoek was je steeds bereikbaar als ik met vragen of problemen zat en je positieve ingesteldheid en steun waren erg belangrijk. Uiteraard wil ik ook mijn co-promotor Peter Dubruel bedanken, je was de broodnodige link met de onderzoeksgroep Polymer Chemistry and Biomaterials. Doordat je het onderzoek vanuit een ander perspectief zag, leverde dat steeds verfrissende inzichten op.

Ik wil ook de andere professoren van de Photonics Research Group bedanken. Roel, Dries, Günther, Geert, Wim en Nicolas, jullie zijn samen verantwoordelijk voor de vruchtbare onderzoeksomgeving in de groep.

Arne en Anabelle, zonder jullie hulp bij de functionalisatie van de sensoren zou ik dit dankwoord waarschijnlijk nu niet aan het schrijven zijn. Jullie waren onmisbaar voor dit onderzoek dankzij de steun die jullie gegeven hebben bij de metingen in de cleanroom. Het is zelfs moeilijk voor te stellen, de uren die we samen in de cleanroom doorgebracht hebben. En dan nog zonder nauwelijks één positief resultaat tijdens de eerste jaren. Gelukkig keerden de kansen naar het einde toe. Uiteraard wil ik ook Els bedanken, voor de hulp die jullie ongetwijfeld aan haar hadden op de Sterre.

Peter en Michael, bedankt voor jullie hulp bij het bouwen van de meetsetup en het schrijven van het computerprogramma. Steven, Liesbet, Kasia en Parastesh, jullie wil ik bedanken voor jullie onvoorwaardelijke inzet om de cleanroom draaiende houden. Bedankt ook Ilse, Ilse, Kristien, Manu, Antonio, Bart, Bert, Eddy, Mike en Jeroen voor jullie ondersteunend werk in het Technicum.

Dan zijn er natuurlijk de collega's doctoraatsstudenten bij de Photonics Research Group. Bedankt voor de samenwerking van de voorbije jaren. Met velen

heb ik zowel professionele als vriendschappelijke relaties kunnen opbouwen. Bedankt Tom, Cristina, Elewout, Jan-Willem, Daan en Rodica voor onder andere de maandelijkse meetings van het bio-team. Uiteraard hebben we samen ook andere mooie momenten beleefd die ik me ongetwijfeld langer zal herinneren. De bureaugenoten, altijd het eerste aanspreekpunt bij het opkijken van het scherm: Kristof, Wout, Elewout, Saurav, Rodica, Sören en Alejandro. Bedankt aan de eerste drie om mij vriendelijk te ontvangen bij mijn aankomst als groentje. Thanks to the others for the good times in our small office. Bedankt aan de fietsende collega's Yannick, Thijs, Pieter en Daan voor de toffe ritten die we samen gemaakt hebben en voor de uitgebreide nabesprekingen. To Thomas, Eva, Raphaël, Amin, Leila, Andreas, Sarah, Bart, Pieter, Anton, Bendix, Pijush, Muhammad, Sarvagya, Herbert, Ashim, Frédéric, Ananth, Alexandre, Paul, Jesper, Jing, Weiqiang, John, Utsav, Sulakshna, Aditya, Alfonso, Chen, Andrew, Ashwyn, Gunay and all other colleagues, I would like to say thanks for the good memories I will keep of the positive working environment you create in Zwijnaarde and Technicum. But even more dear are the personal memories of the many occasions we had to spend time together without photonics on our minds. Als laatste in dit lijstje zijn er natuurlijk ook de ex-collega's, die ondertussen andere oorden opgezocht hebben, maar waarmee ik ook toffe momenten beleefd heb tijdens mijn dagen bij de groep: Karel, Marie, Joris, Peter, Martijn, Martin, Bram, Alban, Nannicha, Anthony, Francois, Abdoulghafar, Sukumar, Dorian, Stevan, Diedrik en Nebiyu.

Bedankt Jef, Seppe en Ruben om me te betrekken bij de organisatie van Robocyclo. Zo had ik een uitlaatklep waarmee ik me kon bezighouden op de momenten dat de fotonen me even te veel werden. Bedankt ook aan Karel, Maarten, Els, Matthew, Job, Jokke, Charlotte, Jasper, Joke, Tim, An, Cleo, Anneleen, Hanne, Dieter, Bart, Ludo, Lieven, Dries en al de anderen die regelmatig of onregelmatig eens meefietsten of meefeestten tijdens één van onze vele events om voor welkome afleiding te zorgen. Bedankt Arno, Arno, Derek, Koen en Sofie voor jullie verhalen over herkenbare situaties in andere onderzoeksgroepen en Luc en Dimi voor onder andere de sportieve momenten in Gent. En uiteraard bedankt Olivier, Heleen-Elise, Niek, Jasper, Jasper, Charlotte, Lynn, Lize, Jehan, Ine, Kristof en Nathan en Ane voor een stabiele uitvalsbasis in Mechelen en ondertussen zelfs Kopenhagen.

Dan is het moment gekomen om mijn familie en dan vooral mijn ouders en zus te bedanken voor hun steun, niet alleen tijdens de vier jaar van mijn doctoraat maar al 27 jaar lang. Bedankt Mama en Papa om me de kansen te geven te studeren wat me interesseert en me te helpen dit punt te bereiken en bedankt Maja en sinds enkele jaren ook Johan. Je voudrais aussi remercier la famille de Pauline pour leur soutien depuis Arcachon. Enfin, je veux surtout remercier Pauline. Merci pour ton soutien quotidien et ta compréhension. Tu

m'as sans aucun doute donné l'encouragement dont j'avais besoin pour finir cette thèse. Mais avant tout, merci pour ton amour et pour partager ta vie avec moi.

Gent, december 2014
Sam Werquin

Table of Contents

List of Figures

List of Tables

List of Acronyms

A

APTES	3-aminopropyltriethoxysilane

B

BCB	B-staged bis-benzocyclobutene
BCG	backward-coupling grating
BSA	bovine serum albumin

C

CCW	counterclockwise
CMOS	complementary metal-oxide-semiconductor
CW	clockwise

D

DMF	dimethylformamide
DNA	deoxyribonucleic acid

E

EtOH	ethanol

F

FWHM	full-width at half maximum
FSR	free spectral range

H

HCG	high-contrast grating
Hynic	hydrazinonicotinamide

L

LOD	limit of detection

M

MMI	multi mode interference
MZI	Mach-Zehnder interferometer

P

PA	pseudomonas aeruginosa
PBS	phosphate buffered saline
PCR	polymerase chain reaction
PDMS	polydimethylsiloxane
PECVD	plasma-enhanced chemical vapour deposition
PEG	polyethylene glycol
POC	point-of-care

Q

Q	quality factor

R

RIE	reactive-ion etching
RCA	rolling circle amplification
RCWA	rigorous coupled wave analysis
RIU	refractive index unit

S

SEM	scanning electron microscope
SOI	silicon-on-insulator
SPR	surface plasmon resonance
S-4FB	succinimidyl-4-formylbenzamide

T

TE	transverse electric
TM	transverse magnetic

V

VAP	ventilator-associated pneumonia
VCSEL	vertical-cavity surface-emitting lasers

Nederlandse samenvatting

De vooruitgang in moleculaire biologie en in het bijzonder genetica over de laatste tientallen jaren heeft geleid tot de ontwikkeling van technieken voor diagnose en prognose in de wereldwijde gezondheidszorg. Toegenomen inzicht in de functionaliteit en de sequentie van zowel menselijk als pathogeen DNA helpt de identificatie van specifieke genen die waardevolle informatie kunnen opleveren als ze herkend worden. Verbetering en miniaturisatie van DNA-versterkingstechnieken, gecombineerd met steeds toenemende gevoeligheid van detectietechnieken, maakt de snelle identificatie van infecties op basis van representatieve DNA-sequenties mogelijk. Dit biedt veel potentieel voor de verbetering van de diagnostiek in diverse medische domeinen. De steeds toenemende aanwezigheid van antibioticaresistente pathogenen bijvoordbeeld, is een belangrijke bedreiging voor de moderne gebruiken in de gezondheidszorg. Het gebruik van te veel of verkeerde antibiotica zorgt er niet alleen voor dat bacteriën zulke resistenties ontwikkelen, maar is bovendien ook niet effectief voor het verbeteren van de gezondheid van een patiënt. Daarom zouden behandelingsbeslissingen in het vroegst mogelijke stadium moeten gegidst worden door de dokters accurate informatie over de antibioticaresistentie van de vermoedelijke infectie aan te reiken. Om dit te bereiken is een snelle en meervoudige analyse nodig die vragen zoals: 'Welk pathogeen veroorzaakt de infectie' of 'Welke resistentiegenen zijn aanwezig' beantwoordt. De beschikbaarheid van zo een hulpmiddel zou de uitkomst van de behandeling significant kunnen verbeteren. Ook in de ontwikkeling van medicijnen zou de zeer hoge kost van klinische proeven, die tegenwoordig jammer genoeg de ontwikkeling van nieuwe antibiotica beperkt, gevoelig gedrukt kunnen worden. Door patiënten snel te screenen voordat ze in de proef opgenomen worden, kan men verzekeren dat enkel relevante patiënten betrokken worden in het onderzoek.

Labelvrije detectietechnieken kunnen uitstekende kandidaten zijn voor zulke point-of-care toepassingen omdat zij ogenblikkelijke kinetische en kwantitatieve bindingsinformatie over de doelmolecules bezorgen in een eenvoudig assay. Zo een labelvrij assay volgt de binding van een doelsequentie op door die te vertalen naar een veranderend uitgangssignaal van een transducer.

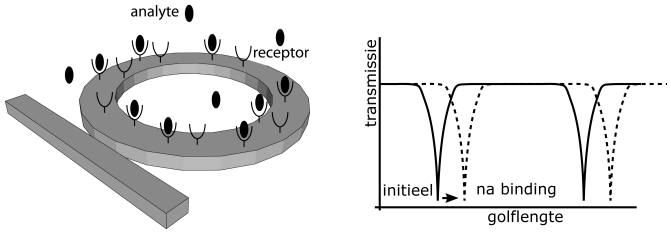

Figuur 1: Labelvrije ringresonatorsensor met chemisch gefunctionaliseerd-golfgeleider oppervlak. De doelmolecules aanwezig in het analiet binden aan de receptoren op de ring en zorgen voor een toename van de effectieve index van de optische mode in de ringgolfgeleider. Dit resulteert in een resonantieverschuiving in het uitgangssignaal. De resonantieverschuiving hangt af van de affiniteit tussen probe en doel en de concentratie van het analiet.

In dit werk onderzoeken we de toepassing van silicium-op-isolator microringresonatortransducers voor de detectie van complementaire DNA-sequenties in een lab-on-a-chip platform. Een ringresonator bestaat uit een optische golfgeleider die een lus maakt op zichzelf. Het licht opgesloten in de ringgolfgeleider propageert met zeer lage verliezen, wat resulteert in erg hoge kwaliteitsfactoren voor de resonatoren. Een of meer optische golfgeleiders zijn evanescent verbonden met de microring om licht van en naar de ring te koppelen. Op resonantie bouwt het vermogen in de microring op ten gevolge van constructieve interferentie terwijl destructieve interferentie een scherpe afname van de lichtintensiteit in de toegangsgolfgeleider veroorzaakt. Door het ringoppervlak te functionaliseren met selectieve receptormolecules meet het onmiddellijk de interactie tussen een molecule uit het analiet en de probes op de ring. Een kleine fractie van het resonante vermogen is aanwezig in de exponentieel afnemende staarten van de optische mode die zich in de mantel uitstrekken en erg gevoelig zijn voor veranderingen aan het oppervlak van de golfgeleider. Deze evanescente staarten voelen onmiddellijk een verandering in de brekingsindex als molecules aan de ring binden. Dit resulteert in een verandering in de effectieve index van de golfgeleidermode en een verandering van de resonantiegolflengte van de ring, zoals verduidelijkt in figuur 1. De golflengteverschuiving hang af van de concentratie van het analiet en zijn affiniteit voor de receptormolecules. Het tijdsverloop van het sensorantwoord voorziet informatie over de reactiekinetiek.

Door een sensorplatform te gebruiken dat de microringsensorchip van

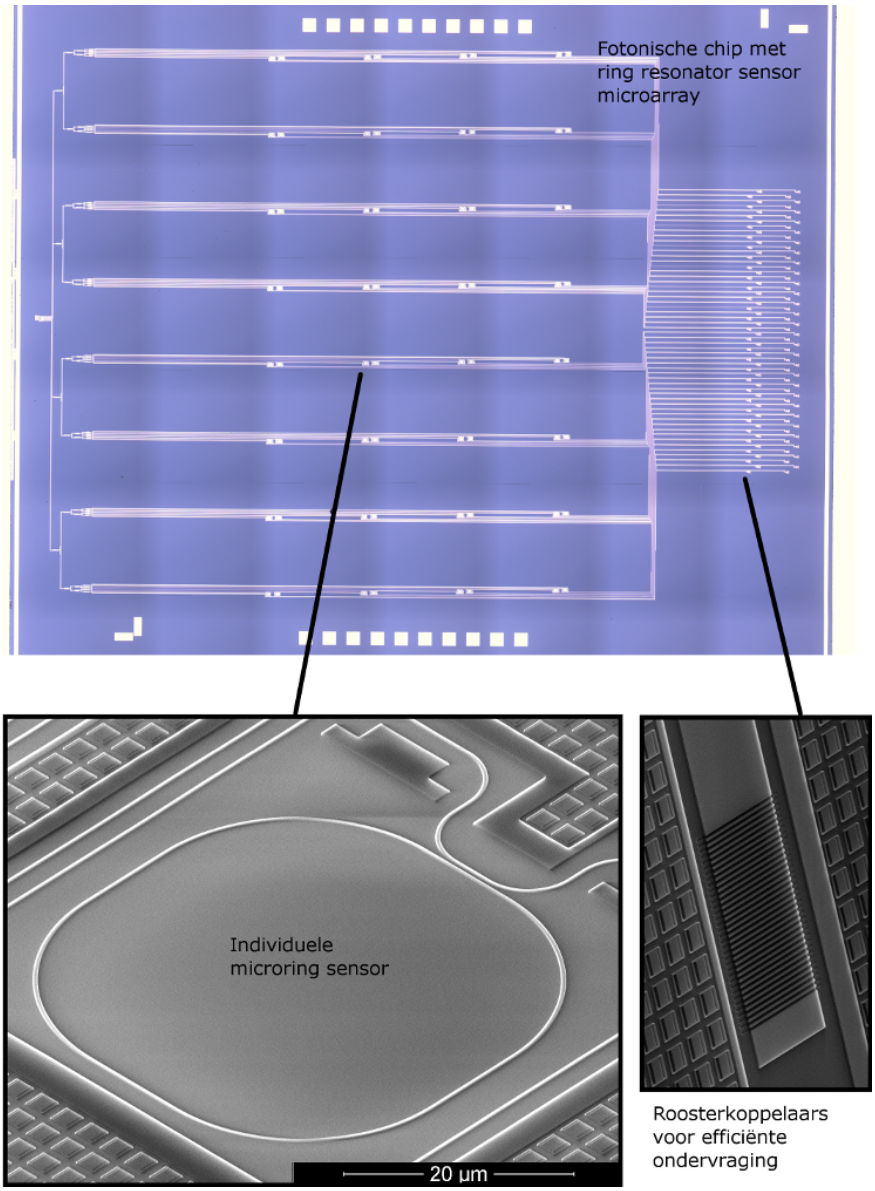

Figuur 2: Ringresonatorsensor microarray voor meervoudige detectie met 64 parallelle sensoren. Door de microringsensoren individueel te functionaliseren kan een meervoudig assay uitgevoerd worden op een enkele siliciumchip. Roosterkoppelaars op de chip staan efficiënte ondervraging van de sensorenreeks door een uitleesinstrument toe.

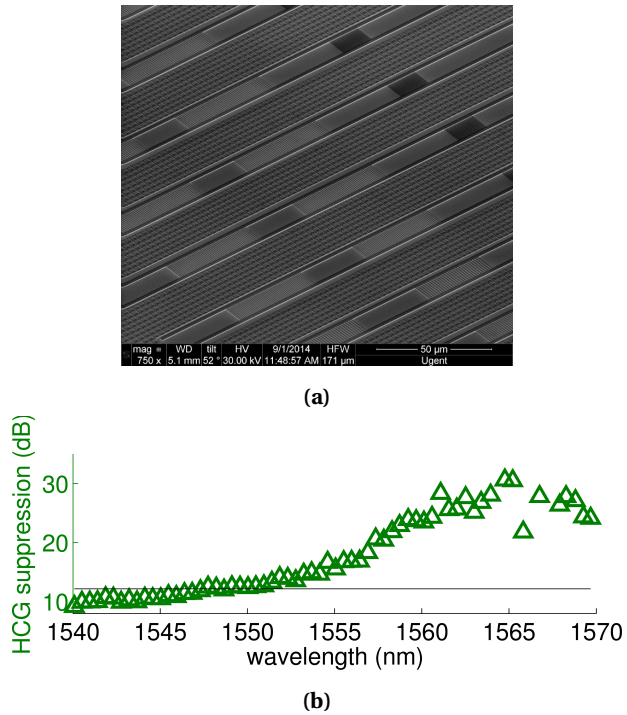

Figuur 3: (a) De implementatie van hoogcontrastroosters om parasitaire signalen in de optische chip te blokkeren resulteert in een experimenteel bepaalde onderdrukking van het parasitaire licht (b) tot 20 dB over een golflengtebereik van meer dan 20 nm.

figuur 2 combineert met microfluidische kanalen, optische uitleesinstrumenten en software voor dataverwerking hebben we de performantie van een microarray van ringresonatoren onderzocht. In samenwerking met de "polymeren en biomaterialen" onderzoeksgroep van de Universiteit Gent is de chemische functionalisatie van de sensoroppervlakken ontwikkeld om DNA-sequenties te detecteren die representatief zijn voor Pseudomonas aeruginosa, een bacterie die vaak verantwoordelijk is voor ventilator geassocieerde pneumonie in de intensievezorgafdeling van ziekenhuizen. Door experimenteel complementaire DNA-concentraties zo laag als 1 nM te detecteren stellen we een calibratiecurve voor het sensorplatform op en we slagen er ook in een detectielimiet van slechts 0.2 nM te extrapoleren, gebaseerd op de experimenteel bepaalde ruis van het sensorsysteem.

Als het sensorplatform gebruikt wordt als automatisch detectiesysteem voor

point-of-care testen dicht bij patiënten in een klinische omgeving, zijn kost, robustheid, lageruisprestaties en gebruiksgemak belangrijke karakteristieken. In ons geval is dit gedeeltelijk gerealiseerd door een fragiele optischevezelinterface van de chip te vervangen door een gecollimeerde lichtbundel. De afmetingen van de bundel staan toe licht in de sensoren te koppelen zonder strikte alignatievoorwaarden en beperken ook de effecten van omgevingstrillingen op de signaalkwaliteit. Dit robust koppelmechanisme drukt de kosten van het volledige systeem aanzienlijk en maakt de bediening door medisch personeel zonder specifieke fotonica-opleiding mogelijk. Toch zijn de sterke interferentieeffecten door parasitair licht een belangrijk nadeel van deze techniek. Dit compromitteert de prestaties van de sensoren sterk en daarom hebben we de implementatie van antitransmissieroosters om de parasitaire lichtpaden naar de optische sensorenreeks te blokkeren, onderzocht. Door het te blokkeren met hoogcontrastroosters bekomen we een efficiënte onderdrukking van het parasitaire licht tot 20 dB over een golflengtebereik van meer dan 20 nm. Deze techniek om parasitaire reflectie te eliminieren is niet beperkt tot sensortoepassingen maar kan breed toegepast worden bij elk geïntegreerd optisch circuit dat robuste en tolerante alignering nodig heeft.

De vorm en kwaliteit van de microringresonantie zijn belangrijke parameters voor alle toepassingen van geïntegreerde microringen. Dit is in het bijzonder het geval voor biosensing met microringtransducers, waar de detectielimiet afhangt van de kwaliteitsfactor van de resonanties. Resonantiesplitsing ten gevolge van reflecties op golfgeleidervariaties heeft echter een ernstige invloed op de resonantiekarakteristieken. We stellen een gedetailleerde discussie van resonantiesplisting in microringen voor en onderzoeken de implementatie van een geïntegreerd interferometrisch circuit dat toegang geeft tot de ongesplitste eigenmodes van de resonator om dit probleem op te lossen.

Hoewel het hoge indexcontrast van silicium-op-isolator golfgeleiders de microringen gevoelig maakt voor de gevolgen van reflecties, is het indexcontrast toch een belangrijk voordeel voor sensortoepassingen. Ten eerste resulteert de sterke opsluiting van de optische mode in de golfgeleiderkern in een zeer hoge gevoeligheid voor moleculaire interacties in de onmiddellijke omgeving van het ringoppervlak. Omdat het evanescent veld snel afneemt met toenemende afstand tot de sensor, is de invloed van bulk indexveranderingen beperkt in vergelijking met het effect van reacties op het oppervlak. Het hoge indexcontrast laat ook de fabricage van erg kleine sensoren toe. Deze kleine ringen zijn uitzonderlijk geschikt voor de integratie in sensorenreeksen. De ringreeks is eenvoudig schaalbaar tot een hoger multiplex niveau. Voor toepassingen met massale multiplexingniveaus, zoals DNA-sequentiëring die duizenden parallelle de-

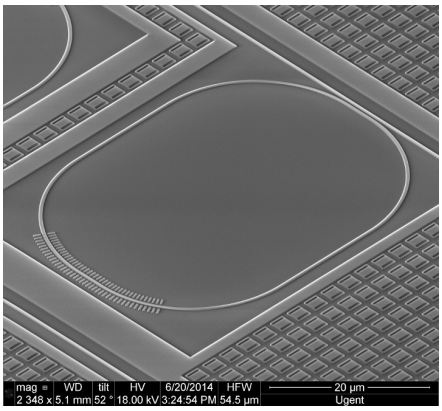

Figuur 4: Een microringresonator met een zwak rooster dicht bij de golfgeleider. Het licht gebroken door het rooster wordt makkelijk opgepikt door een camera boven de ring terwijl de resonanties een kwaliteitsfactor behouden die voldoende hoog is voor sensortoepassingen.

tecties vereist, nemen de roosterkoppelaars en golfgeleiders op het chipoppervlak echter meer plaats in dan de eigenlijke sensoren. Voor zulke hoge parallellisatie wordt de verbinding van de microringresonatoren met golfgeleiders praktisch onhaalbaar en moeten alternatieve koppelmechanismes onderzocht worden. Daarom onderzoeken we de integratie van microringsensoren met zwakke roosters die licht onmiddellijk uit de ring koppelen, zoals in figuur 4. Zo een roostergekoppelde microring is een eerste stap naar ringsensoren zonder toegangsgolfgeleiders, wat de weg opent naar ongeziene niveaus van parallelle detecties.

English summary

The advances in molecular biology and in particular genetics over the last decades have led to emerging tools for diagnosis and prognosis in healthcare worldwide. Increased insight in the functionality and the sequence of both human and pathogenic DNA helps the identification of specific genes which can provide valuable information when recognized. Improvement and miniaturization of DNA amplification methods combined with ever increasing sensitivity of detection techniques, enables the development of rapid identification of infections based on representative DNA sequences. This shows great potential for improving diagnostics in a multitude of medical fields. The increasing prevalence of antibiotics-resistant pathogens for example is an important threat to modern healthcare practices. The use of too many or wrong antibiotics not only provokes bacteria to develop such resistances, but could also be ineffective in improving a patient's health. Therefore, treatment decisions should be guided in the earliest possible stage by providing the clinicians with accurate antibiotics resistance information for the suspected infection. To accomplish this, a fast and multiplexed assay that answers questions like: 'Which pathogen causes the infection?' or 'Which resistance genes are present?' is required. The availability of such a tool could significantly improve treatment outcome. Also in the development of medicines, the very high cost related to clinical trials, which is nowadays unfortunately a limitation in the development of new antibiotics, could be significantly reduced. By fast profiling of patients before they are enrolled in the trial, it can be ensured that only relevant people are included.

Label-free detection technologies could be excellent candidates for these point-of-care applications, because they provide real-time kinetic and quantitative binding information about the target molecules in a simple assay. Such a label-free assay directly monitors the binding of a target sequence by translating it to a changing output signal of a transducer. In this work, we investigate the application of silicon-on-insulator microring resonator transducers for the detection of complementary DNA sequences in a lab-on-a-chip platform. A ring resonator consists of an optical waveguide forming a loop on itself. The light confined to the ring waveguide can propagate with very low losses, result-

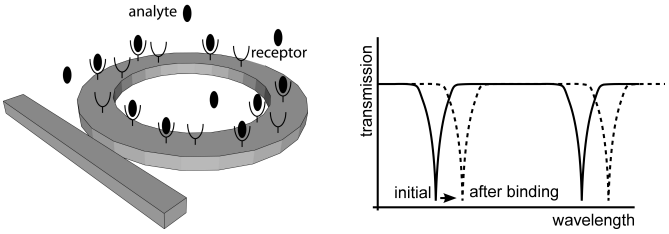

Figure 1: Label-free ring resonator sensor with chemically functionalized waveguide surface. The target molecules present in the sample bind to the receptors on the ring and increase the effecctive index of the optical mode in the ring waveguide. This results in a resonance wavelength shift in the output signal. The resonance shift depends on the affinity between probe and target and the analyte concentration.

ing in high quality factors for the resonator. One or more optical waveguides are evanescently coupled to the microring to couple light to and from the ring. On resonance, the optical power in the microring builds up due to constructive interference while destructive interference causes a sharp decrease in the light intensity in the access waveguide. By functionalizing the ring surface with selective receptor molecules, it directly measures the interaction between an analyte molecule and the probes on the ring. A small fraction of the resonating power is located in exponentially decaying tails of the optical mode that extend into the cladding regions and are very sensitive to changes on the waveguide surface. These evanescent tails immediately feel a change in the refractive index if molecules bind to the ring. This results in a change in the effective index of the waveguide mode and a changing resonance wavelength of the microring, as depicted in figure 1. The wavelength shift depends on the concentration of the analyte and its affinity to the receptor molecules. The time evolution of the sensor response provides information about the reaction kinetics.

Using a sensing platform that combines the microring sensor chip of figure 2 with microfluidic channels, optical readout equipment and software for data processing, we have analyzed the performance of a microarray of ring resonators. In collaboration with the polymers and biomaterials group of Ghent University, the chemical functionalization of the sensor surface is developed to detect a DNA sequence representative for Pseudomonas aeruginosa, a bacterium commonly responsible for ventilator-associated pneumonia in intensive care units of hospitals. By experimentally detecting complementary DNA concentrations down to 1 nM we establish a calibration curve for the sensor

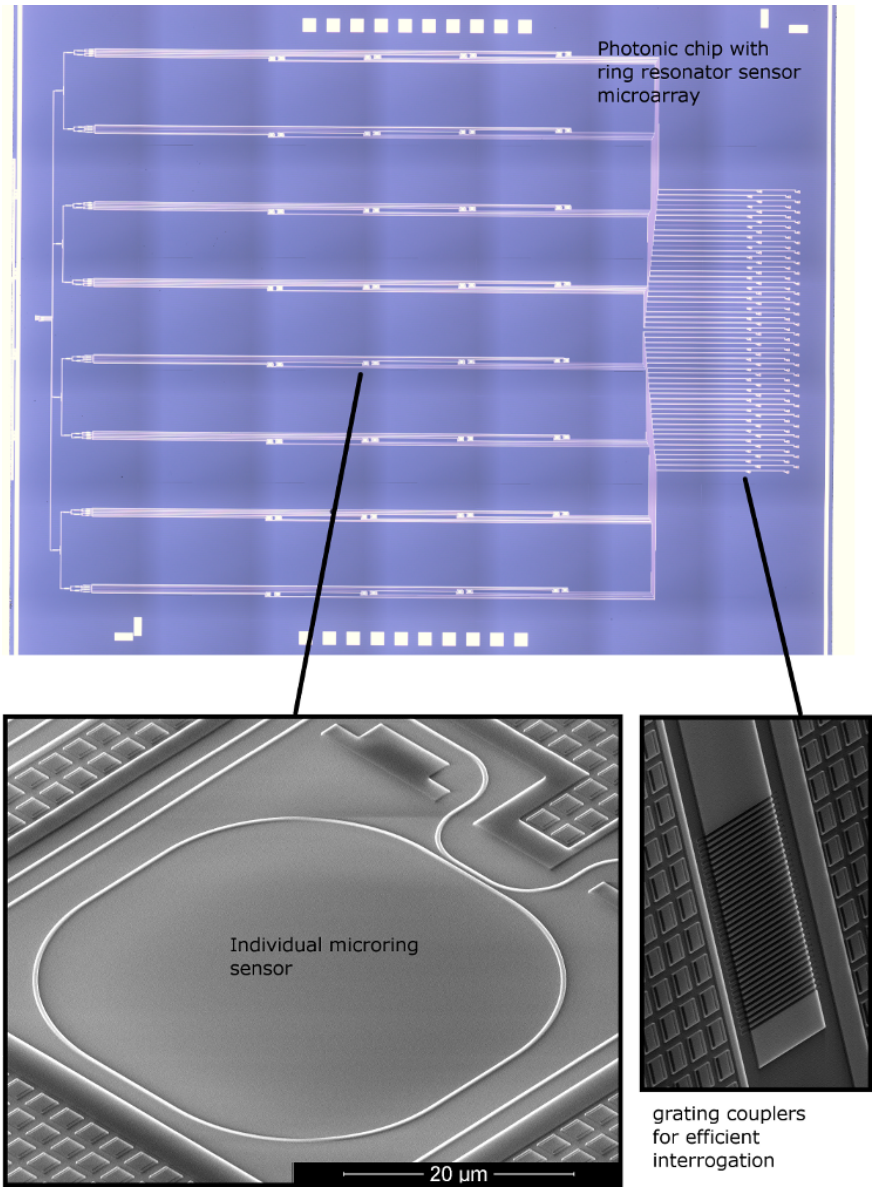

Figure 2: Ring resonator sensor microarray for multiplexed detection with 64 parallel sensors. By individually functionalizing the microring sensors, a highly multiplexed assay can be performed on a single silicon chip. On-chip grating couplers allow efficient interrogation of the sensor array by a readout instrument.

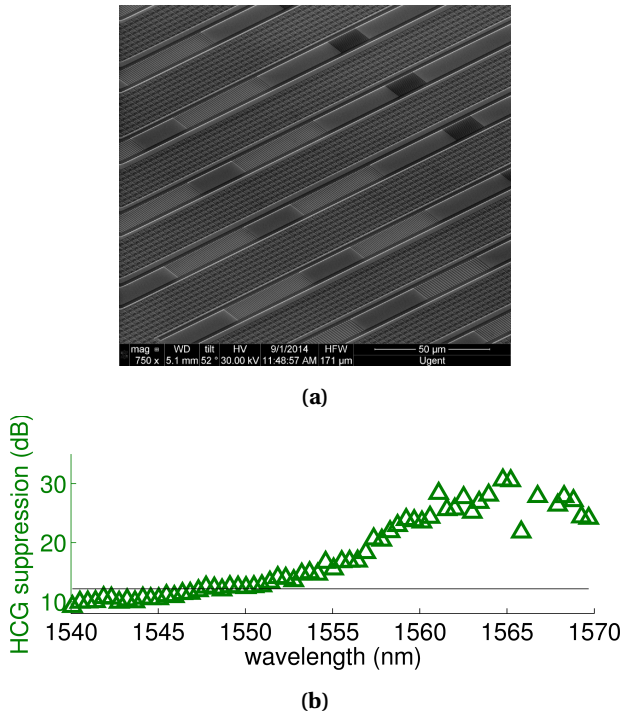

Figure 3: (a) The implementation of high-contrast gratings to block parasitic signals in the optical chip results in an experimentally determined suppression (b) of the parasitic light up to 20 dB over a wavelength range of more than 20 nm.

platform and we are also able to extrapolate a detection limit of only 0.2 nM, based on the experimentally recorded noise of the sensing system.

When the sensor platform is used as an automated detection system for point-of-care testing close to patients in a clinical setting, important characteristics are cost, robustness, low-noise performance and ease of use. In our case, this is realized in part by eliminating a fragile optical fiber interface of the chip and replacing it by a collimated light beam. The size of the beam enables light coupling to the sensors without strict alignment conditions and also limits the influence of ambient vibrations on the signal quality. This robust coupling scheme significantly reduces the cost of the complete system and also facilitates the operation by medical staff without specific photonics training. However, a drawback of this approach is the introduction of strong interference effects by parasitic light. This significantly compromises the performance of the sensors

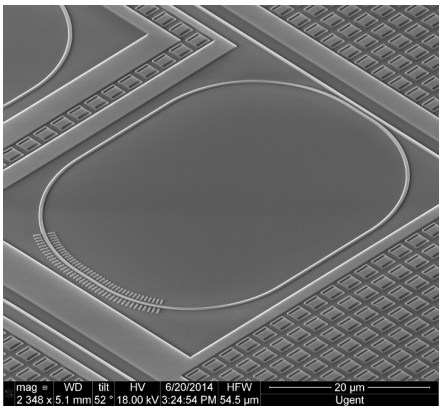

Figure 4: A microring resonator with weak grating in the vicinity of the waveguide. The light diffracted by the grating can easily be picked up by a camera above the ring while the resonances maintain a quality factor high enough for sensing applications.

and therefore we have investigated the implementation of anti-transmission gratings to eliminate the parasitic light paths to the optical sensor array. By blocking it using the high-contrast reflection gratings of figure 3, an efficient suppression of the parasitic light up to 20 dB is obtained over a wavelength range of more than 20 nm. This technique of eliminating parasitic reflections is not restricted to sensing applications and can be applied to any integrated optical circuit that requires robust and tolerant alignment.

The shape and quality of a microring resonance are important parameters for all applications of integrated microrings. This is true in particular for biosensing with microring transducers, where the detection limit depends on the quality factor of the resonances. However, resonance splitting as a result of backreflection on waveguide variations severely affects the resonance characteristics. We provide a detailed discussion of resonance splitting in microrings and also investigate the implementation of an integrated interferrometric circuit that gives access to the unsplit normal modes of the resonator to solve this issue.

While the high index contrast of the SOI waveguides makes the microrings sensitive to the effects of backreflection, the index contrast is still a significant advantage for sensing applications. First, the high confinement of the optical mode to the waveguide core results in a very high sensitivity to the molecular

interactions in the immediate vicinity of the ring surface. Because the evanescent field decays rapidly with increasing distance to the sensor, the influence of bulk index changes is low compared to the effect of reactions on the surface. The high index contrast also enables the fabrication of very small sensors. These small rings are exceptionally suited for the integration in sensor arrays. The ring array is easily scalable to higher degrees of multiplexing. However, for applications with massive degrees of multiplexing like DNA sequencing which requires several thousands of detections in parallel, the grating couplers and waveguide routing on the chip start taking up more chip surface than the actual sensors. For such high degrees of parallelization, connecting microring resonators with on chip waveguides becomes practically impossible and alternative coupling schemes to the sensors are required. Therefore, we investigate the integration of microring sensors with weak gratings that couple light directly out of the ring, like in figure 4. Such a grating coupled microring is a first step towards ring sensors without access waveguides, opening the path to unprecedented levels of parallel detection.

1 Introduction

The advances in molecular biology and in particular genetics over the last decades have led to emerging tools for diagnosis and prognosis in healthcare worldwide. Increased insight in the functionality and the sequence of both human and pathogenic DNA helps the identification of specific genes which can provide valuable information when recognized. Improvements and miniaturization of DNA amplification methods combined with ever increasing sensitivity of detection techniques, enables the development of rapid identification of infections based on representative DNA sequences. This shows great potential for improving diagnostics in a multitude of medical fields. The increasing prevalence of antibiotics-resistant pathogens for example, is an important threat to modern healthcare practices [1]. The use of too many or wrong antibiotics not only provokes bacteria to develop such resistances, but could also be ineffective in improving a patient's health. Therefore, treatment decisions should be guided in the earliest possible stage by providing the clinicians with accurate antibiotics resistance information for the suspected infection [2]. To accomplish this, a fast and multiplexed assay that answers questions like: 'Which pathogen causes the infection?' or 'Which resistance genes are present?' is required. The availability of such a tool could significantly improve treatment outcome. Also in the development of medicines, the very high cost related to clinical trials, which is nowadays unfortunately a limitation in the development of new antibiotics, could be significantly reduced. By fast profiling of patients

before they are enrolled in the trial, it can be ensured that only relevant people are included.

Several biomedical companies have developed point-of-care (POC) tests that can provide this invaluable information for a variety of infections. These assays typically rely on DNA amplification using a polymerase chain reaction (PCR) followed by the detection of the target sequences with biosensor technology. Tests like Prove-it [3], LightCycler [4, 5] or GeneXpert [6] provide the high sensitivity required in medical practice. As an example, consider the Mobidiag Prove-it assay [7] which can identify up to 80 bacteria or fungi related to sepsis on a microarray in a matter of hours. This shows the importance of a biosensor technology which can provide rapid results, over a wide dynamic range and with a high degree of multiplexing. Considering biosensing, two main categories can be identified: the label-based and label-free sensors.

1.1 Label-based biosensing

Most DNA detection techniques rely on the indirect detection of DNA hybridization by attaching easily measurable labels to the duplexes. The labels can be specific antibodies that amplify a weight-based signal [8], but mostly fluorescent dyes are used to produce a visible signal [9–11]. A typical labelled DNA detection scheme is depicted in figure 1.1. Target DNA strands bind to specific probes on the surface of beads or a detection array. After a washing step, a new solution containing the label is introduced. The label can be non-specific, like an antibody or protein binding to the immobilized DNA, but also target-specific labels can be used to introduce extra specificity. Such a target-specific label could be a short, complementary DNA strand with a fluorescent tag, that binds to the partly-hybridized target strand. Examples of non-specific labels are enzymes that initiate a reaction with a substrate, resulting in a visible signal. After another washing step, all non-bound labels are rinsed and the remaining labels can be detected.

An advantage of labelled biosensing is the very low detection limit that can generally be obtained, down to the single DNA molecule level [12] because of the intrinsic signal amplification by the label. A labelled assay can also be performed in solution, on the surface of beads for example. However labelling also has several disadvantages. Multiplexing possibilities for an assay in solution are typically quite limited when using non-specific labels. Recently, higher degrees of multiplexing have been demonstrated using target specific labels and color-coded fluorescence in different ratios [13]. Moreover, using a microarray for detection instead of an assay in solution, all multiplexing limitations can be eliminated. However, the introduction of the labels complicates a labelled assay and requires the use of additional reagents, adding significant cost and devel-

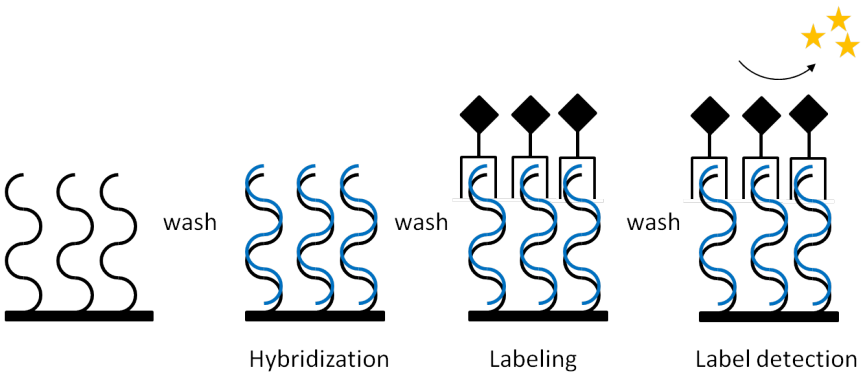

Figure 1.1: During labelled sensing, target molecules bind to receptors on the surface. After this step, a label that binds to the immobilized complexes on the surface is introduced. These labels enable the detection of the molecules on the surface, typically by emitting fluorescent light.

opment time to the assay [14]. The extra reaction steps also increase the assay time. Finally, an important limitation lies in the fact that only the label is actually monitored. No real-time information concerning the reaction kinetics of the actual target is available [15]. This significant drawback can be solved by performing label-free sensing.

1.2 Label-free biosensing

A label-free assay does not have the limitations intrinsic to labelling techniques, as the binding of a target sequence is directly monitored and translated to an output signal. This provides real-time kinetic information about the affinity between target and probe. The response can also be interpreted quantitatively. A generic label-free assay is demonstrated in figure 1.2. Here, target-specific probes are bound to the surface of a transducer. The transducer immediately translates the immobilization of target molecules on its surface to a changing output signal. This signal can be based on optical, electrical or mechanical properties of the analyte. Many label-free technologies with specific transducers are being developed [14, 16]. Label-free sensors can be multiplexed by functionalizing different transducers with different capture probes to form a microarray. Because a transducer is inherently non-specific, careful attention has to be paid to the chemical surface modifications. These have to introduce a very high specificity to the selected target, while at the same time eliminating any non-specific interaction with other molecules present in the sample.

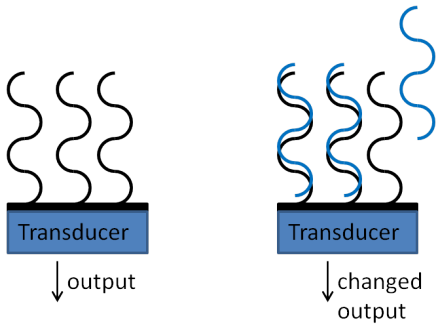

Figure 1.2: Target molecules bind to a transducer coated with receptor molecules. The properties of the target molecules change the state of the transducer which is translated to a measurable change in the output signal.

The most widespread label-free technology is surface plasmon resonance (SPR) [17, 18], which measures a change in refractive index on a gold surface using surface plasmon modes. In this research, we investigate the application of silicon photonic ring resonator sensors as transducers for DNA detection. These sensors have lately attracted a lot of attention from several research groups because of their various advantages for label-free assays. While most applications of label-free microring sensors are found in the detection of various proteins because of the additional affinity information, several DNA detection experiments have been demonstrated. A particularly interesting study that employs a key advantage of label-free sensors shows the discrimination of single-nucleotide polymorphism in DNA sequences by analysing the reaction dynamics on the surface [19]. In [20], the experimental detection limit of label-free nucleic acid detection is established at 0.5 nM. A practical detection limit of a system is not only determined by the sensitivity of the transducer or sensor, but the entire sensing protocol has an influence on this. A multitude of aspects play a role, ranging from sample collection, over sample preparation, microfluidic systems, surface chemistry and transducer sensitivity to readout equipment. All these steps and components can be combined in a single device in a so-called lab-on-a-chip.

1.3 Lab-on-a-chip

In this context, the term lab-on-a-chip describes a single chip that tries to combine microfluidics and transducers [21]. This integration has the potential of a significant cost reduction of assays. The microfluidic chip can perform sam-

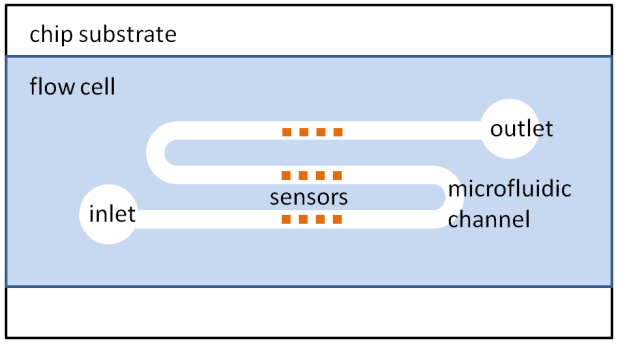

Figure 1.3: Integration of a microfluidic flow cell with an optical sensor array. The microfluidic channel brings the analyte to the transducers, where the affinity reaction on the chip surface is translated to a changing output signal.

ple preparation steps like mixing, centrifugation or upconcentration without requiring expensive laboratory equipment or highly trained staff. The automation of the steps also reduces the risk for human operating errors. Many implementations of microfluidics exist, but for our application a simple flow cell is placed over the sensor surface to bring the analyte to the functionalized sensor surface, as demonstrated in figure 1.3. This way, the target molecules are in close contact with the receptor molecules on the transducer. The often disposable lab-on-a-chip is integrated with readout equipment to enable the measurement of the transducer signals. This results in a fully-automated detection system that, if combined with the right software, reports the result of an assay directly to the operator.

In a medical context, this is often referred to as point-of-care testing as the automated detection system can be brought close to patients in a clinical setting. Additional requirements for such a device are cost, robustness and low-noise performance, also with respect to the optical detection array. In our case, this is realized by eliminating a fragile optical fiber interface of the chip and replacing it by a collimated light beam. The size of the beam enables light coupling to the sensors without strict alignment conditions and also limits the influence of ambient vibrations on the signal quality. This robust coupling scheme significantly reduces the cost of the complete system and also facilitates the operation by medical staff without specific photonics training. However, a drawback of this approach is the introduction of strong interference effects by parasitic light. This significantly compromises the performance of the sensors and therefore we have investigated the implementation of anti-transmission gratings to eliminate the parasitic light paths to the optical sensor array in

chapter 4.

1.4 Photonic ring resonator detection arrays

The transducers of the biosensor platform investigated during this research are photonic microring resonators. Those ring resonators consist of a silicon-on-insulator (SOI) optical waveguide forming a loop on itself. The light confined to the ring waveguide can propagate with very low losses, resulting in high quality factors for the resonator. One or more optical waveguides are evanescently coupled to the microring to couple light to and from the ring. On resonance, the optical power in the microring builds up due to constructive interference while destructive interference causes a sharp decrease in the light intensity in the access waveguide. Because of their small size and sharp filter characteristics, microring resonators are well-known photonic components with many applications in integrated optics [22]. Passive microrings have been investigated for on-chip filters [23], wavelength division multiplexed networks [24, 25] or delay elements in optical buffers [26].

In label-free sensing applications, a microring resonator functionalized with selective receptor molecules directly measures the interaction between an analyte molecule and the probes on the ring. A small fraction of the resonating power is located in exponentially decaying tails of the optical mode that extend into the cladding regions and are very sensitive to changes on the waveguide surface. These evanescent tails immediately feel a change in the refractive index if molecules bind to the ring. This results in a change in the effective index of the waveguide mode and a changing resonance wavelength of the microring, as depicted in figure 1.4. The wavelength shift depends on the concentration of the analyte and its affinity to the receptor molecules. The time evolution of the sensor response provides information about the reaction kinetics.

The shape and quality of a microring resonance are important parameters for all applications of integrated microrings. This is true in particular for biosensing with microring transducers, where the detection limit depends on the quality factor of the resonances [27, 28]. However, resonance splitting as a result of backreflection on waveguide variations severely affects the resonance characteristics. In chapter 5, we investigate the implementation of an integrated interferrometric circuit that gives access to the unsplit normal modes of the resonator to solve this issue.

While the high index contrast of the SOI waveguides makes the microrings sensitive to the effects of backreflection, the index contrast is still a significant advantage for sensing applications. First, the high confinement of the optical mode to the waveguide core results in a very high sensitivity to the molecular interactions in the immediate vicinity of the ring surface. Because the evanescent

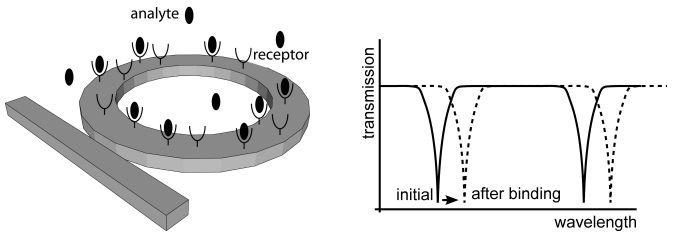

Figure 1.4: Label-free ring resonator sensor with chemically functionalized waveguide surface. The target molecules present in the sample bind to the receptors on the ring and increase the effective index of the optical mode in the ring waveguide. This results in a resonance wavelength shift in the output signal. The resonance shift depends on the affinity between probe and target and the analyte concentration.

field decays rapidly with increasing distance to the sensor, the influence of bulk index changes is low compared to the effect of reactions on the surface. This means the sensor is much less affected by bulk index variations than comparable SPR sensors [29]. The high index contrast also enables the fabrication of very small sensors, with a radius of only 16 μm. These small rings are exceptionally suited for the integration in sensor arrays. Silicon sensor chips with multiplexed detection arrays of up to 128 sensors in parallel are reported in [30–33]. The integration of the sensor arrays with microfluidic channels and a reader instrument to perform biosensing experiments is also demonstrated. This easy integration is another benefit of the SOI platform. Grating couplers that enable easy and efficient coupling of optical signals to the sensors can be lithographically defined in the same processing steps as the microrings [32, 34]. Figure 1.5 shows such a ring resonator microarray. This array is easily scalable to higher degrees of multiplexing. However, for applications with massive degrees of multiplexing like DNA sequencing which requires several thousands of detections in parallel [35], the grating couplers and waveguide routing on the chip start taking up more chip surface than the actual sensors. For such high degrees of parallelization, this approach to connect microring resonators becomes practically impossible and alternative coupling schemes to the sensors are required. Therefore, we investigate the integration of microring sensors with weak gratings that couple light directly out of the ring in chapter 6. Such a grating coupled microring is a first step towards ring sensors without access waveguides, opening the path to unprecedented levels of parallel detection.

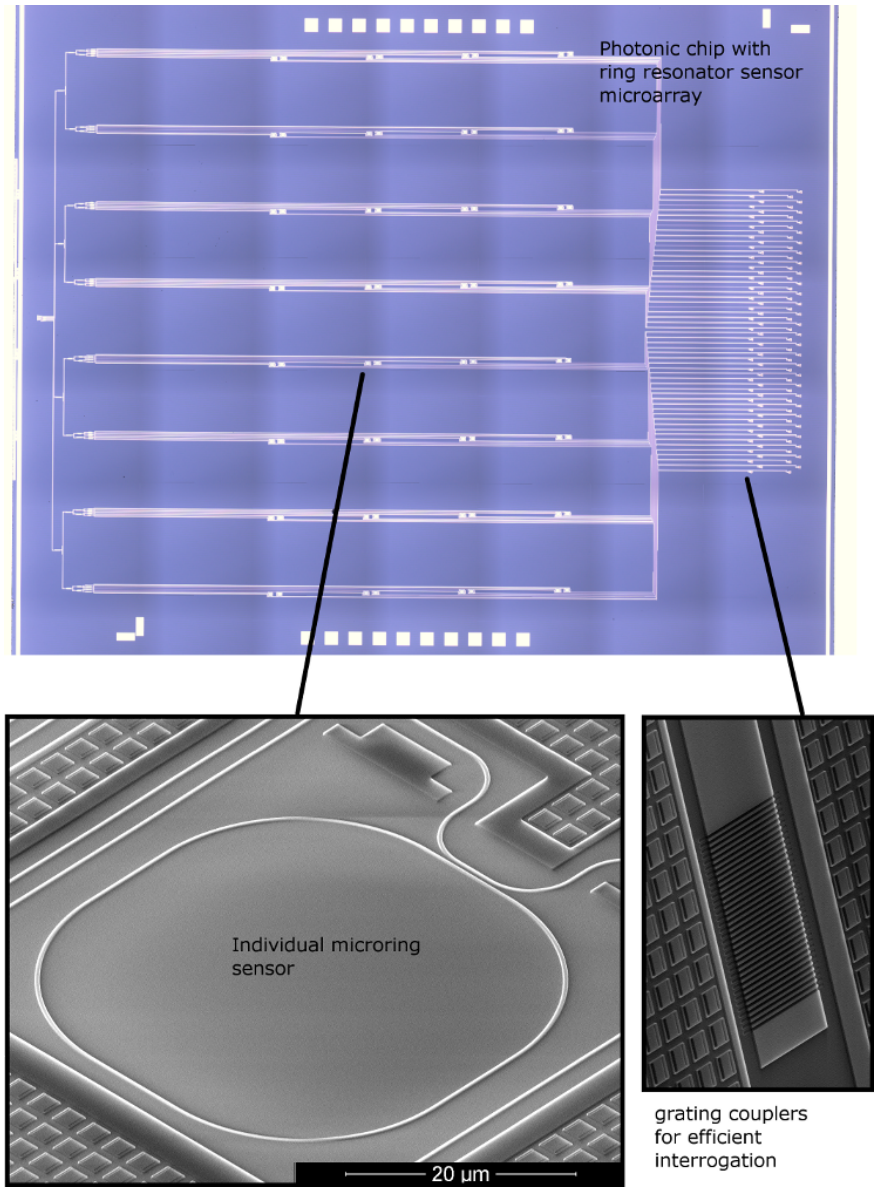

Figure 1.5: Ring resonator sensor microarray for multiplexed detection with 64 parallel sensors. By individually functionalizing the microring sensors, a highly multiplexed assay can be performed on a single silicon chip. On-chip grating couplers allow efficient interrogation of the sensor array by a readout instrument.

1.5 Thesis outline

The goal of this work is to investigate the application of microring resonator biosensor arrays to detect complementary DNA sequences. In this prospect, several improvements to the performance and the applicability of the microrings are made. Part of the work has been focused on issues that are specific for sensing applications, like the surface chemistry or the measurement setup. However photonic solutions that are widely applicable to a variety of integrated applications are also provided. Parasitic interferences also limit the performance of integrated applications such as optical coherence tomography [36] and on-chip laser Doppler vibrometry [37] and a thorough understanding of resonance splitting is of primordial importance when designing microring filters [23, 38]. At the same time, the investigation of alternative array configurations without access waveguides, is a requirement for massive multiplexing applications such as DNA sequencing.

Chapter 2 gives an overview of the characteristics of microring resonators that make them ideal candidates for biosensing. A theoretical description of resonance splitting is provided and the concept of refractive index sensing is described in more detail. This chapter also includes an overview of applications of microring resonator sensors reported in literature.

Chapter 3 describes in depth the application of the microrings in a sensor array for complementary DNA detection. This includes a description of the photonic chip, microfluidic interface and the measurement setup and software. The performance of the measurement setup and the optical sensors is discussed, but also the chemical functionalization of the sensor surface. The different surface modification steps and experimental results for DNA detection are presented. At the moment, complementary DNA concentrations down to 1 nM are measured and an experimental detection limit of 0.2 nM is extrapolated. Also suggestions for future improvements are made.

Chapter 4 demonstrates the application of anti-transmission gratings to eliminate parasitic interferences in the optical signals, while still maintaining the high alignment tolerance required for many applications. Two implementations are discussed, both theoretically and by experimental investigation of practical prototypes. By using a high-contrast grating to block the parasitic light, an efficient suppression up to 20 dB is obtained over a wavelength range of more than 20 nm.

Chapter 5 provides an investigation of microring resonance splitting. An

integrated interferometric circuit is introduced that gives access to the high-quality, unsplit normal modes of the microring resonator. The width of the normal modes is reduced by a factor three compared to that of the split signal. This could be beneficial in reducing the detection limit for sensors that are affected by resonance splitting, but also for other applications that require very narrow resonances.

Finally, chapter 6 demonstrates the combination of microring resonators with weak gratings that enable vertical interrogation of the rings. The quality factors of the vertically diffracting microrings are still sufficiently high to be applicable in sensing applications. This could lead to the elimination of access waveguides, which is a requirement for massive multiplexing applications of ring sensors.

Part of this work is performed in the framework of the FP-7 Rapp-id project, a collaboration between academic and industry partners to develop rapid point-of-care test platforms for infectious diseases.

1.6 Publications

Patent applications

1. S. Werquin and P. Bienstman, *System for coupling radiation into a waveguide*

Publications in international journals

1. S. Werquin, Y. De Koninck, P. Bienstman, *Ring Resonators With Vertically Coupling Grating for Densely Multiplexed Applications,* IEEE Photonics Technology Letters, 27(1):97–100, 2015.
2. S. Werquin, D. Vermeulen, P. Bienstman, *Implementation of Surface Gratings for Reduced Coupling Noise in Silicon-on-Insulator Circuits,* IEEE Photonics Technology Letters, 26(16):1589–1592, 2014.
3. J.W. Hoste, S. Werquin, T. Claes, P. Bienstman, *Conformational analysis of proteins with a dual polarisation silicon microring,* Optics Express, 22(3):2807–2820, 2014.
4. P. Mechet, T. Spuesens, S. Werquin, K. Vandoorne, N. Olivier, J.-M. Fedeli, P. Regreny, D. Van Thourhout, G. Roelkens, and G. Morthier, *All-optical low-power 2R regeneration of 10Gb/s NRZ signals using a III-V on SOI microdisk laser.* IEEE Photonics Journal, 5(6), 2013.
5. E.M.P. Ryckeboer, J. Vierendeels, A. Lee, S. Werquin, P. Bienstman, R. Baets, *Measurement of small molecule diffusion with an optofluidic silicon chip,* Lab on a Chip, 13(22):4392–4399, 2013.
6. S. Werquin, S. Verstuyft, P. Bienstman, *Integrated interferometric approach to solve microring resonance splitting in biosensor applications,* Optics Express, 21(14):16955–16963, 2013.

Publications in international conferences

1. J.W. Hoste, S. Werquin, P. Bienstman, *Employing dual polarisation biosensing to study the conformational behaviour of BSA molecules during the adsorption to a silicon microring,* Europtrode 2014.
2. S. Werquin, D. Vermeulen, A. Goes, A. Van Eeghem, P. Dubruel, P. Bienstman, *Improved performance of highly multiplexed silicion-on-insulator microring sensor chips by surface structure implementation,* Nanoscale Imaging, Sensing, and Actuation for Biomedical Applications XI, 2014.
3. J.W. Hoste, S. Werquin, P. Bienstman, *Dual polarisation biosensing with an SOI microring,* Proceedings of the 18th Annual Symposium of the IEEE Photonics Society Benelux Chapter, 2013.

4. P. Bienstman, S. Werquin, C. Lerma Arce, E. Hallynck, T. Claes, J.W. Hoste, D. Martens, *Silicon nanophotonics on-chip sensing (invited),* Progress In Electromagnetics Research Symposium (PIERS 2013), 2013.
5. S. Werquin, A. Goes, P. Dubruel, P. Bienstman, *Silicon-on-insulator microring resonators for photonic biosensing applications (invited),* International Conference on Transparent Optical Networks-ICTON, 2013.
6. P. Bienstman, S. Werquin, C. Lerma Arce, D. Witters, R. Puers, J. Lammertyn, T. Claes, E. Hallynck, J.W. Hoste, D. Martens, *Nanophotonic biosensors in silicon-on-insulator (invited),* The 17th International Conference on Solid-State Sensors, Actuators and Microsystems (Transducers 2013), 2013.
7. P. Bienstman, S. Werquin, C. Lerma Arce, D. Witters, R. Puers, J. Lammertyn, T. Claes, E. Hallynck, J.W. Hoste, D. Martens, *Ring resonator based SOI biosensors (invited),* 2013 Photonics West Conference, 2013.
8. A. Goes, S. Werquin, E. Vanderleyden, P. Bienstman, P. Dubruel, *Development an evaluation of chemical interfaces for a nanophotonic silicon-on-insulator biosensor platform,* Label-Free Technologies : Adances and Applications, Abstracts, 2012.

Publications in national conferences

1. A. Van Eeghem, S. Werquin, E. Vanderleyden, P. Bienstman, P. Dubruel, *Functionalisation of nanophotonic silicon-on-insulator biosensor chips for real-time DNA detection,* Diatech 2014, 2014.
2. E.M.P. Ryckeboer, A. Lee, S. Werquin, J. Vierendeels, P. Bienstman, R. Baets, *Investigation of glucose diffusion using an optofluidic silicon chips,* Proceedings of the 2012 Annual Symposium of the IEEE Photonics Society Belenux Chapter, 2012.
3. S. Werquin, P. Bienstman, *Interferometric approach to solve microring resonance splitting in biosensor applications,* Proceedings of the 2012 Annual Symposium of the IEEE Photonics Society Benelux, 2012.

References

[1] *Identifying Drug-Resistant Bacterial Infections: Opportunity and Activity in the Diagnostics Arena.* John Wiley & Sons, Inc., 2006.

[2] http://www.ua.ac.be/main.aspx?c=RAPP-ID. 2014.

[3] http://www.mobidiag.com/Products/ProveittradeSepsis/ProveittradeSepsisStripArray/tabid/242/Default.aspx. 2014.

[4] http://molecular.roche.com/assays/Pages/LightCyclerMRSAAdvancedTest.aspx. 2014.

[5] L. M. Sloan, J. R. Uhl, E. A. Vetter, C. D. Schleck, W. S. Harmsen, J. Manahan, R. L. Thompson, J. E. Rosenblatt, and F. R. Cockerill. *Comparison of the Roche LightCycler vanA/vanB detection assay and culture for detection of vancomycin-resistant enterococci from perianal swabs.* J. Clin. Microbiol., 42(6):2636–2643, Jun 2004.

[6] http://www.cepheid.com/us/cepheid-solutions/systems/genexpert-systems/genexpert-i. 2014.

[7] P. Tissari, A. Zumla, E. Tarkka, S. Mero, L. Savolainen, M. Vaara, A. Aittakorpi, S. Laakso, M. Lindfors, H. Piiparinen, M. Mäki, C. Carder, J. Huggett, and V. Gant. *Accurate and rapid identification of bacterial species from positive blood cultures with a DNA-based microarray platform: an observational study.* The Lancet, 375(9710):224–230, 2010.

[8] A. J. Qavi, J. T. Kindt, M. a. Gleeson, and R. C. Bailey. *Anti-DNA:RNA Antibodies and Silicon Photonic Microring Resonators: Increased Sensitivity for Multiplexed microRNA Detection.* Analytical chemistry, 83(15):5949–56, August 2011.

[9] A.-K. Jarvinen, S. Laakso, P. Piiparinen, A. Aittakorpi, M. Lindfors, L. Huopaniemi, H. Piiparinen, and M. Maki. *Rapid identification of bacterial pathogens using a PCR- and microarray-based assay.* BMC Microbiology, 9, Augustus 10 2009.

[10] T. Klamp, M. Camps, B. Nieto, F. Guasch, R. T. Ranasinghe, J. Wiedemann, Z. Petrasek, P. Schwille, D. Klenerman, and M. Sauer. *Highly Rapid Amplification-Free and Quantitative DNA Imaging Assay.* Scientific Reports, 3, May 16 2013.

[11] R. T. Ranasinghe and T. Brown. *Ultrasensitive fluorescence-based methods for nucleic acid detection: towards amplification-free genetic analysis.* Chem. Commun., 47:3717–3735, 2011.

[12] M. Karhanek, J. T. Kemp, N. Pourmand, R. W. Davis, and C. D. Webb. *Single DNA Molecule Detection Using Nanopipettes and Nanoparticles.* Nano Letters, 5(2):403–407, 2005.

[13] Y.-P. Ho, M. C. Kung, S. Yang, and T.-H. Wang. *Multiplexed Hybridization Detection with Multicolor Colocalization of Quantum Dot Nanoprobes.* Nano Letters, 5(9):1693–1697, 2005.

[14] A. J. Qavi, A. L. Washburn, J.-Y. Byeon, and R. C. Bailey. *Label-free technologies for quantitative multiparameter biological analysis.* Analytical and Bioanalytical Chemistry, 394(1):121–135, May 2009.

[15] J. L. Arlett, E. B. Myers, and M. L. Roukes. *Comparative advantages of mechanical biosensors.* Nature Nanotechnology, 6(4):203–215, April 2011.

[16] M. Nirschl, F. Reuter, and J. Vőrős. *Review of Transducer Principles for Label-Free Biomolecular Interaction Analysis.* Biosensors, 1(3):70–92, 2011.

[17] J. Homola. *Surface plasmon resonance sensors for detection of chemical and biological species.* Chemical Reviews, 108(2):462–493, February 2008.

[18] A. J. Tudos and R. B. Schasfoort. *Chapter 1 Introduction to Surface Plasmon Resonance.* In Handbook of Surface Plasmon Resonance, pages 1–14. The Royal Society of Chemistry, 2008.

[19] A. J. Qavi, T. M. Mysz, and R. C. Bailey. *Isothermal Discrimination of Single-Nucleotide Polymorphisms via Real-Time Kinetic Desorption and Label-Free Detection of DNA Using Silicon Photonic Microring Resonator Arrays.* Analytical chemistry, 83(17):6827–33, September 2011.

[20] O. Scheler, J. T. Kindt, A. J. Qavi, L. Kaplinski, B. Glynn, T. Barry, A. Kurg, and R. C. Bailey. *Label-free, multiplexed detection of bacterial tmRNA using silicon photonic microring resonators.* Biosensors and Bioelectronics, 36(1):56 – 61, 2012.

[21] D. Psaltis, S. R. Quake, and C. Yang. *Developing optofluidic technology through the fusion of microfluidics and optics.* Nature, 442(7101):381–386, July 27 2006.

[22] W. Bogaerts, P. D. Heyn, T. V. Vaerenbergh, K. D. Vos, S. Kumar, T. Claes, P. Dumon, P. Bienstman, D. V. Thourhout, and R. Baets. *Silicon Microring Resonators.* Laser & Photonics Reviews, 6(1):47–73, 2011.

[23] P. De Heyn, B. Kuyken, D. Vermeulen, W. Bogaerts, and D. Van Thourhout. *Improved intrinsic Q of Silicon-on-Insulator microring resonators using TM-polarized light.* In Proceedings of the 2010 Annual Symposium of the IEEE Photonics Benelux Chapter, pages 197–200, 2010.

[24] B. Little, J. Foresi, G. Steinmeyer, E. Thoen, S. Chu, H. Haus, E. Ippen, L. Kimerling, and W. Greene. *Ultra-compact Si-SiO2 microring resonator optical channel dropping filters.* IEEE Photonics Technology Letters, 10(4):549–551, April 1998.

[25] P. D. Heyn and J. D. Coster. *Fabrication-tolerant four-channel wavelength-division-multiplexing filter based on collectively tuned Si microrings.* Journal of Lightwave Technology, 31(16):2785–2792, 2013.

[26] F. Xia, L. Sekaric, and Y. Vlasov. *Ultracompact optical buffers on a silicon chip.* Nature Photonics, 1(1):65–71, January 2007.

[27] T. Claes, J. Molera, K. De Vos, E. Schacht, R. Baets, and P. Bienstman. *Label-Free Biosensing With a Slot-Waveguide-Based Ring Resonator in Silicon on Insulator.* IEEE Photonics Journal, 1(3):197–204, September 2009.

[28] J. Hu, X. Sun, A. Agarwal, and L. C. Kimerling. *Design guidelines for optical resonator biochemical sensors.* J. Opt. Soc. Am. B, 26(5):1032–1041, 2009.

[29] M. S. Luchansky, A. L. Washburn, T. a. Martin, M. Iqbal, L. C. Gunn, and R. C. Bailey. *Characterization of the evanescent field profile and bound mass sensitivity of a label-free silicon photonic microring resonator biosensing platform.* Biosensors & bioelectronics, 26(4):1283–1291, July 2010.

[30] M. Iqbal, M. A. Gleeson, B. Spaugh, F. Tybor, W. G. Gunn, M. Hochberg, T. Baehr-Jones, R. C. Bailey, and L. C. Gunn. *Label-Free Biosensor Arrays Based on Silicon Ring Resonators and High-Speed Optical Scanning Instrumentation.* IEEE Journal of Selected Topics in Quantum Electronics, 16(3):654–661, 2010.

[31] S. Janz, D. X. Xu, M. Vachon, N. Sabourin, P. Cheben, H. McIntosh, H. Ding, S. Wang, J. H. Schmid, A. Delage, J. Lapointe, A. Densmore, R. Ma, W. Sinclair, S. M. Logan, R. MacKenzie, Q. Y. Liu, D. Zhang, G. Lopinski, O. Mozenson, M. Gilmour, and H. Tabor. *Photonic wire biosensor microarray chip and instrumentation with application to serotyping of Escherichia coli isolates.* Optics Express, 21(4):4623–4637, February 25 2013.

[32] A. Densmore, D. X. Xu, P. Cheben, M. Vachon, S. Janz, R. Ma, D. Bedard, Y. Li, G. Lopinski, A. Delage, J. H. Schmid, R. Halir, and I. Molina-Fernandez. *Integration of Vertical Grating Couplers and Microfluidic Channels with Silicon Photonic Wire Biosensor Arrays.* In 2010 IEEE Sensors, IEEE Sensors, pages 1550–1553, 2010. 2010 IEEE Sensors Conference, Kona, HI, Nov 01-04, 2010.

[33] A. Densmore, D. Xu, N. A. Sabourin, H. Mcintosh, P. Cheben, J. H. Schmid, R. Ma, M. Vachon, A. Delâge, W. Sinclair, J. Lapointe, Y. Li, G. Lopinski, B. Lamontagne, and S. Janz. *A Fully Integrated Silicon Photonic Wire Sensor Array Chip and Reader Instrument.* Optics Express, pages 350–352, 2011.

[34] G. Roelkens, D. Vermeulen, S. Selvaraja, R. Halir, W. Bogaerts, and D. V. Thourhout. *Grating-Based Optical Fiber Interfaces for Silicon-on-Insulator Photonic Integrated Circuits.* IEEE J. Quantum Electron., 17(3):571–580, 2011.

[35] T. T. Torres, M. Metta, B. Ottenwälder, and C. Schlötterer. *Gene expression profiling by massively parallel sequencing.* Genome research, 18(1):172–7, January 2008.

[36] G. Yurtsever, B. Považay, A. Alex, B. Zabihian, W. Drexler, and R. Baets. *Photonic integrated Mach-Zehnder interferometer with an on-chip reference arm for optical coherence tomography.* Biomedical Optics Express, 5(4):1050, March 2014.

[37] Y. Li, P. Segers, J. Dirckx, and R. Baets. *On-chip laser Doppler vibrometer for arterial pulse wave velocity measurement.* Biomedical optics express, 4(7):1229–35, July 2013.

[38] P. De Heyn, D. Vermeulen, T. Van Vaerenbergh, B. Kuyken, and D. Van Thourhout. *Ultra-high Q and finesse all-pass microring resonators on Silicon-on-Insulator using rib waveguides.* In 16th European Conference on Integrated Optics and technical exhibition, page 195, 2012.

2
Microring Resonators

In this chapter, microring resonators and their characteristics that make them ideal candidates for optical biosensors are discussed. First, the optical waveguide that forms the microring is introduced. In section 2.2, two configurations of microring resonators are discussed. Section 2.3 describes resonance splitting, an important effect in high-quality microring resonators that is often overlooked but can significantly affect their performance. Finally, in section 2.4 the application of microrings as transducers for optical biosensors is discussed.

2.1 Photonic Waveguides

Integrated silicon waveguides are much like the optical fibers used for data transfer, only smaller. An optical waveguide consists of a high refractive index core and a low refractive index cladding. Light is preferentially concentrated in the high index core, with a small fraction of its power extending into the cladding regions. For light with a wavelength of 1550 nm, the silicon-on-insulator (SOI) material system shows an exceptionally high index contrast. The silicon waveguide core has a refractive index of 3.47, while the silica bottom cladding has an index of only 1.44. For most sensing applications, the top cladding will typically consist of aqueous solutions like serum or water-based buffers with refractive indices around 1.31. Light that propagates through an invariant waveguide without changing its transversal shape is called a waveguide

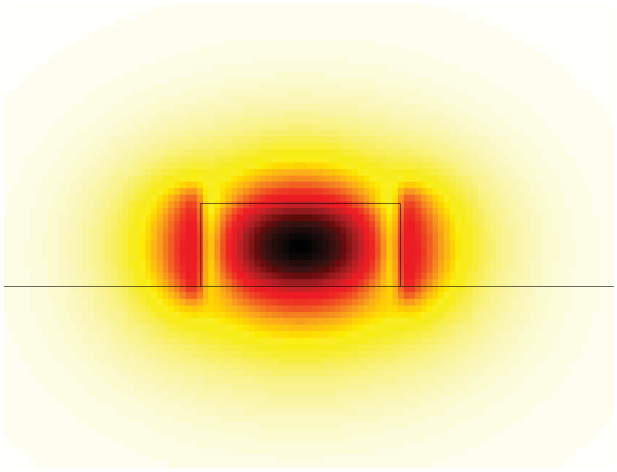

Figure 2.1: Cross section of a silicon on insulator wire waveguide with the intensity distribution of the fundamental quasi-TE mode.

mode. Such a mode is characterized by an invariant transversal intensity profile and an effective index. The effective index of the mode is the ratio between the vacuum speed of light and the phase velocity of the propagating light. It represents how strongly the optical power is confined to the waveguide core. Optical modes with an effective index higher than the largest cladding index are guided modes. Modes with lower index are radiating and the optical power will leak to the cladding regions. Because of the strong confinement in the silicon wires, the waveguide modes are highly dispersive. In practice this means the first order dispersion cannot be neglected and the group index (n_g) of the mode has to be taken into account when considering wavelength changes.

The waveguide dimensions determine which modes can exist. Most waveguides support modes of two independent polarizations, with either the major magnetic (quasi-TM) or electric (quasi-TE) field component along the transverse (horizontal) direction. For most biosensing applications, it is preferable that the waveguides operate in a single-mode regime for each polarization. This single-mode regime is obtained by reducing the waveguide dimensions until all but the fundamental waveguide modes become radiating. The cross section of a silicon wire waveguide measuring 450 nm by 220 nm with the corresponding distribution of the power of the fundamental optical mode is given in figure 2.1. For any waveguide geometry, part of the optical mode power is confined to the silicon waveguide core. The remaining power is located in the cladding regions. For guided modes, the intensity in the cladding region decays exponentially with increasing distance to the core. It is this evanescent tail of the mode

that can sense changes in the waveguide vicinity. The binding of biomolecules to the waveguide will locally change the surrounding refractive index which results in a changing effective index of the optical mode. To inspect the interaction between an optical mode and its environment, waveguides can be used in resonant structures with highly wavelength-dependent behaviour.

2.2 Microring Resonators

The high index contrast of SOI waveguides allows the fabrication of micrometer size bends. The possibility to create very small ring resonators has made them one of the successful components of silicon photonics. Because of their unprecedented small size and wide applicability, silicon microring resonators have been the subject of many scientific publications. In this section, we will discuss the characteristics of microring resonators that make them ideal candidates for biosensing transducers.

A microring resonator consists of a closed circular waveguide. A light wave propagating through a microring waveguide will interfere with itself after one roundtrip. When this interference is constructive, the light will start to resonate in the ring. The resonance condition for constructive interference is satisfied when the phase difference after one roundtrip amounts to an integer multiple of 2π. This means the wavelength of the optical mode has to fit an integer number of times in the roundtrip length of the ring. We can thus express the resonance condition as follows:

$$\lambda_{res} = \frac{n_{eff} L}{m}, m \in \mathbb{N} \tag{2.1}$$

A microring resonator will have an infinite number of resonances, one for every solution of the resonance condition. To address the resonator, connections to access waveguides are needed. Typically, these connections are made by including directional coupler sections. A directional coupler is a region where two waveguides are in close proximity. The evanescent tails of the fields in the waveguide will feel the presence of the other waveguide and coupling between both can occur. The strength of the coupling will depend on the overlap between both waveguide modes and the length of the coupler. Based on the number of access waveguides, we will consider two configurations of microring resonators that can be used for biosensing applications. If only a single access waveguide is present, the resonator is called an all-pass resonator. A microring with two access waveguides is an add-drop or channel-drop resonator. Both configurations are discussed in more detail in the next sections.

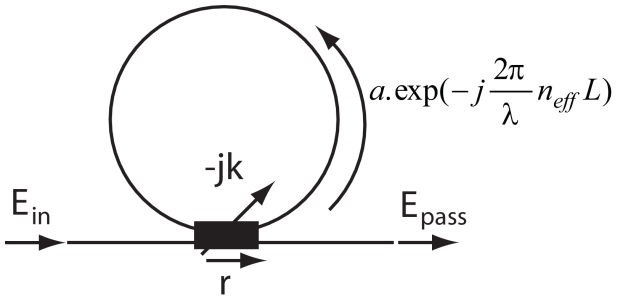

Figure 2.2: Schematic representation of a microring in the all-pass configuration.

2.2.1 All-pass ring resonators

A ring resonator with one access waveguide is in the all-pass configuration. A schematic representation is given in figure 2.2. A fraction k of the input field couples to the ring in the directional coupler. On resonance, the light in the ring interferes constructively and power in the resonator builds up. Light coupling back from the ring to the waveguide will then interfere destructively with the remainder of the input light that is transmitted by the directional coupler. The higher the losses in an undercoupled microring, the lower the transmitted power. Off resonance, the input light does not couple to the ring and the transmitted power is maximal. The power transmission of an all-pass microring is given by equation 2.2:

$$T_{all-pass} = \frac{a^2 - 2ar\cos\phi + r^2}{1 - 2ar\cos\phi + (ar)^2}, \text{ with} \phi = \frac{2\pi}{\lambda} n_{eff} L \tag{2.2}$$

Here a is the roundtrip amplitude reduction due to losses in the ring and r the amplitude self-coupling coefficient of the directional coupler. For a lossless coupler, r is related to the amplitude cross-coupling or coupling loss k as $r = \sqrt{1+k^2}$. The transmission spectrum of an all-pass ring is plotted in figure 2.3.

The spectrum is characterized by the full-width at half maximum (FWHM) of the resonances, the on-off extinction ratio and the free spectral range (FSR) between consecutive resonances. The quality factor, an important characteristic of the resonance, relates to the FWHM as $Q = \frac{\lambda_{res}}{FWHM}$. If the resonator losses and the coupling to the waveguide increase, the resonance broadens.

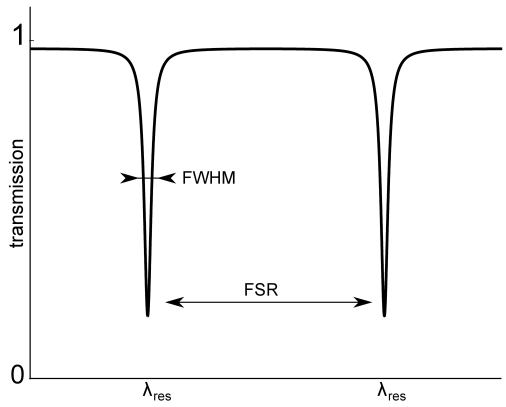

Figure 2.3: Transmission spectrum of a microring in the all-pass configuration.

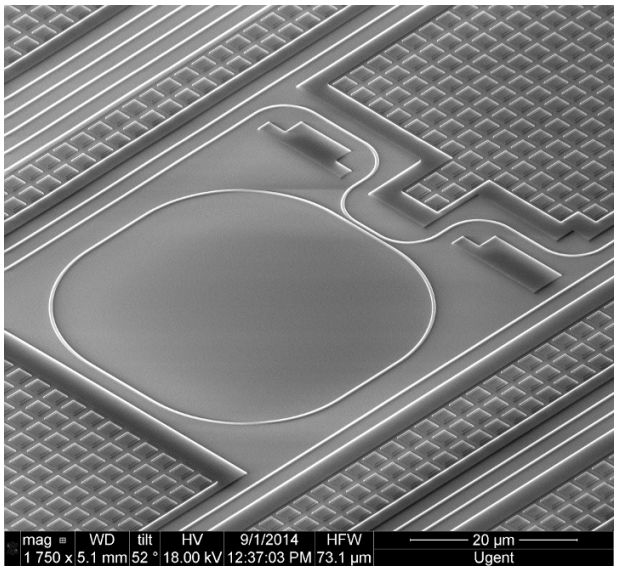

Figure 2.4: SEM image of an all-pass microring.

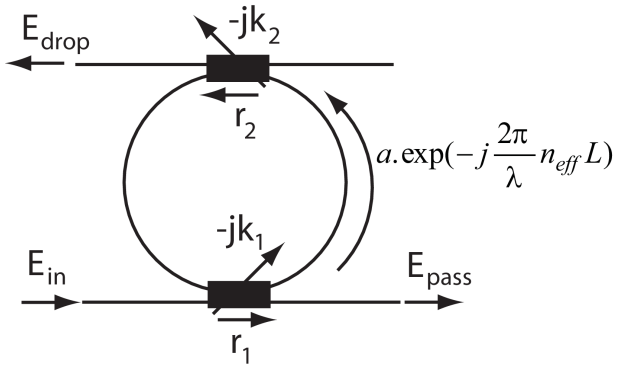

Figure 2.5: Schematic representation of a microring in the add-drop configuration.

The ring is undercoupled if the coupling loss is less then the roundtrip loss ($r > a$). The extinction ratio of the resonances becomes infinite for critical coupling, when the coupling loss balances the roundtrip loss of the ring ($r = a$). If the coupling loss increases further ($r < a$), the ring becomes overcoupled. The resonances broaden and their extinction ratio is reduced. In this research, a critically-coupled all-pass microring like the one depicted in figure 2.4 is used. The microring consists of 450 nm wide and 220 nm high waveguides with 16 μm bends. By including 10 μm straight sections, the FSR of the ring is reduced to 3.6 nm in water. The coupling section has a 250 nm wide gap and is 4 μm long to achieve critcal coupling.

2.2.2 Add-drop ring resonators

An add-drop or channel drop resonator has two access waguides, as shown in figure 2.5. The second waveguide makes it possible to drop or add signals at the resonance wavelength to the signal in the input waveguide. Just like for the all-pass resonator, constructive interference builds up the power in the ring on resonance. Because a second waveguide is coupled to the microring, part of this power couples to this waveguide and light at the resonance wavelength is dropped to the drop port, hence the name. The drop port will show transmission peaks at the resonance wavelengths. The output of the access waveguide, the pass port, features a dip in transmitted power on resonance. Off resonance, the pass transmission is maximum and the drop port is dark. The add-drop resonator is described by two transmission functions, one for the pass port and

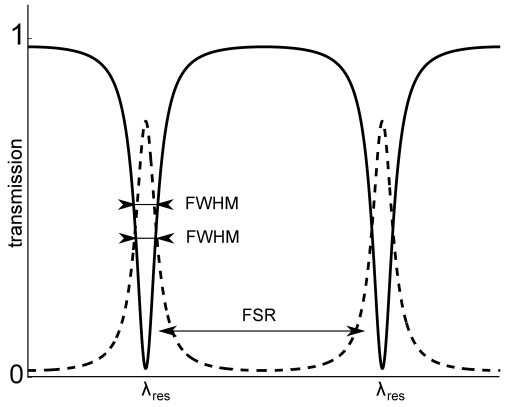

Figure 2.6: Transmission spectrum of a microring in the add-drop configuration.

one for the drop port that are given by equation 2.3:

$$\begin{aligned} T_{pass} &= \frac{a^2 r_2^2 - 2ar_1 r_2 \cos\phi + r_1^2}{1 - 2ar_1 r_2 \cos\phi + (ar_1 r_2)^2} \\ T_{drop} &= \frac{a(1-r_1^2)(1-r_2^2)}{1 - 2ar_1 r_2 \cos\phi + (ar_1 r_2)^2}, \text{ with } \phi = \frac{2\pi}{\lambda} n_{eff} L \end{aligned} \tag{2.3}$$

As an add-drop resonator has two directional coupler sections, two different amplitude self-coupling coefficients feature in the equations. r_1 represents the self-coupling of the input directional coupler and r_2 is the self-coupling coefficient of the directional coupler leading to the drop port. The transmission spectra are plotted in figure 2.6.

When comparing the pass port transmission to that of an all-pass resonator, we see that the second coupler acts as an extra loss mechanism in the microring. The add-drop resonator is critically coupled if $r_1 = ar_2$. Like for an all-pass microring, the pass transmission of the add-drop resonator at critical coupling is zero, but the FWHM of the add-drop ring is larger because of the higher losses induced by the drop waveguide. A SEM image of an add-drop microring used in this research is given in figure 2.7. The microring is close to critically coupled by implementing asymmetrical pass and drop couplers. It has the same design parameters as the all-pass ring we described in 2.2.1, except for the in and output couplers that are 4 μm and 6 μm long, respectively.

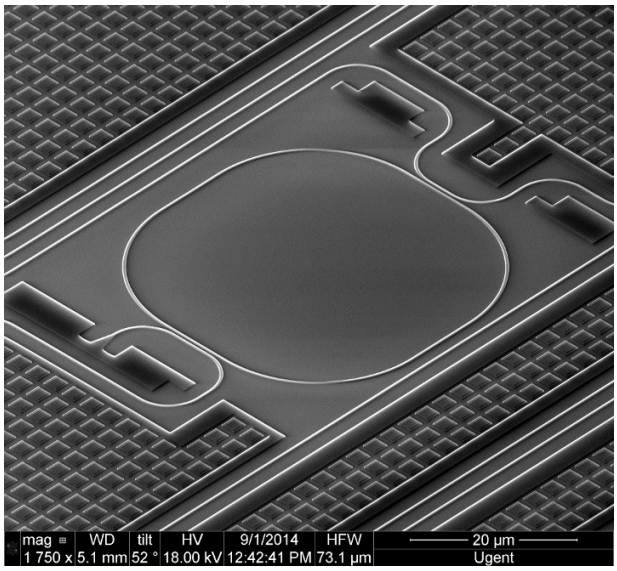

Figure 2.7: SEM image of an add-drop microring.

2.2.3 Lorentzian resonance shape

Ideal microring resonators are described by a Lorentzian resonance shape. This first-order approximation of the transmission is valid around the resonance wavelength and makes the description and fitting of the resonance parameters much simpler compared to the periodic transmission functions 2.2 and 2.3. For the all-pass sensor or the pass port of the add-drop sensor, this Lorentzian function is given by equation 2.4:

$$T_{pass}(\lambda) = \frac{R_{min}\left(\frac{FWHM}{2}\right)^2 + (\lambda_{res} - \lambda)^2}{\left(\frac{FWHM}{2}\right)^2 + (\lambda_{res} - \lambda)^2} \tag{2.4}$$

Here, R_{min} denotes the mininum (on-resonance) transmission. A similar function is obtained for the drop transmission of the add-drop sensor:

$$T_{drop}(\lambda) = \frac{R_{max}\left(\frac{FWHM}{2}\right)^2}{\left(\frac{FWHM}{2}\right)^2 + (\lambda_{res} - \lambda)^2} \tag{2.5}$$

Here, R_{max} denotes the maximum (on-resonance) transmission in the drop waveguide. These Lorentzian approximations are extremely useful because they immediately provide key resonance parameters as the resonance wavelength and the FWHM. The extinction ratio of the resonator can be used to obtain coupling fraction and roundtrip losses as described in [1].

2.3 Resonance splitting in microrings

A perfectly symmetric microring resonator mode in the absence of a bus waveguide is twofold degenerate. Both clockwise (CW) and counterclockwise (CCW) propagation are possible in the microring and the modes are uncoupled. This degeneracy is lifted when the CW mode and CCW mode become coupled, e.g. by surface roughness on the waveguide edges and by the proximity of bus waveguides. These deviations from circular symmetry cause forward propagating light to scatter back into the opposite direction, exciting a CCW mode from a CW mode and vice versa. Standing-wave modes as a symmetric and antisymmetric superposition of the traveling waves can now be considered as the new eigenmodes of the system. They will however no longer be degenerate as a consequence of the symmetry-breaking coupling [2]. If the linewidth of the resonance is small enough to distinguish both modes, the resonance splitting will be visible in the output signal. This occurs for high quality resonances, when the backreflected power becomes comparable to the coupling losses of the resonator. A critical relation between reflected power and microring coupling for ideal resonators is derived in [3]. The reasoning can be extended to lossy resonators. If a microring has intrinsic losses, a certain amount of backreflection will have less severe consequences on the ring performance compared to the situation without losses.

Using the simple coupled harmonic oscillator model described in [2], one can easily derive expressions for modes in the microring, as well as the transmitted and reflected fields of a microring resonator coupled to a waveguide in the all-pass configuration. The coupled mode system is described by equation 2.6:

$$\begin{array}{rcl} \frac{da_{CW}}{dt} & = & i\Delta\omega a_{CW} - \frac{1}{2\tau} a_{CW} + \frac{i}{2\gamma} a_{CCW} + \kappa s \\ \frac{da_{CCW}}{dt} & = & i\Delta\omega a_{CCW} - \frac{1}{2\tau} a_{CCW} + \frac{i}{2\gamma} a_{CW} \end{array} \tag{2.6}$$

Here, a is the amplitude of the CW and CCW modes ($|a|^2$ is the energy stored in the CW and CCW modes, respectively) and s represents the field in the input waveguide ($|s|^2$ is the input power) that couples to the CW mode. The frequency of the lightwave is detuned by $\Delta\omega$ with respect to the resonance frequency of the resonator. τ is the lifetime of photons in the resonator and is determined by the total losses of the coupled microring resonator. The photon lifetime is related to the quality factor (Q) of the microring as $Q = \omega\tau$. The factor κ describes the coupling from the input wave to the resonator mode. By associating a lifetime $\tau_{ext} = 1/\kappa^2$ to the coupling coefficient, intrinsic resonator losses can be distinguished from coupling losses as $1/\tau = 1/\tau_{ext} + 1/\tau_0$. The factor τ_0 is determined by material absorption and scattering losses in the microring waveguide. Losses in the bends and directional coupler also contribute to the intrinsic amplitude decay in the resonator. The coupling between CW and CCW mode is described

by the scattering lifetime γ. As explained in [4], the traditionally-used power coupling coefficient K can be readily translated to the coupling coefficient κ used in this description by expressing the energy decay in a lossless microring:

$$|a(t)|^2 = |a_0|^2 \exp(-t/\tau_{ext}) \tag{2.7}$$

Considering the relation between stored energy and power flow in the ring, the power coupled to the output waveguide is given by:

$$K^2 |A(t)|^2 = K^2 \frac{v_g}{2\pi R} |a(t)|^2 \tag{2.8}$$

In equation 2.8, power coupling coefficient K and the power in the ring $|A(t)|^2$ are introduced. v_g is the group velocity of the waveguide mode and $2\pi R$ the circumference of the ring. Taking the derivative of equation 2.7 and equating this to equation 2.8 results in the relation between the power coupling coefficient K and the coupling coefficient κ used for energy normalized waves:

$$K^2 = \kappa^2 \frac{2\pi R}{v_g} \tag{2.9}$$

Equation 2.9 shows that the proportionality factor between K^2 and κ^2 corresponds to the round-trip time in the microring.

The eigenmodes of the coupled system in equation 2.6 are a symmetric and antisymmetric superposition of the CW and CCW mode. The complex amplitudes of these new eigenmodes are given by:

$$\begin{aligned} a_+ &= \tfrac{1}{\sqrt{2}}(a_{CW} + a_{CCW}) &&= \tfrac{1}{\sqrt{2}} \tfrac{-\kappa s}{i\left(\Delta\omega + \frac{1}{2\gamma}\right) - \frac{1}{2\tau}} \\ a_- &= \tfrac{1}{\sqrt{2}}(a_{CW} - a_{CCW}) &&= \tfrac{1}{\sqrt{2}} \tfrac{-\kappa s}{i\left(\Delta\omega - \frac{1}{2\gamma}\right) - \frac{1}{2\tau}} \end{aligned} \tag{2.10}$$

From equations 2.10, it is clear that the eigenmodes are centered around the new eigenfrequencies $\omega = \omega_0 \pm 1/2\gamma$. They each have a linewidth of $1/\tau$, determined by the losses of the coupled microring. The intensity distribution of the normal modes is given in figure 2.8 and has a Lorentzian shape. The results from equation 2.10 can be used to calculate both the CW and CCW mode given by equation 2.11, as well as the transmitted and reflected fields for the microring coupled to an input waveguide in equation 2.12:

$$\begin{aligned} a_{CW} &= \tfrac{1}{\sqrt{2}}(a_+ + a_-) &&= \tfrac{-\kappa s}{2} \tfrac{2i\Delta\omega - \frac{1}{\tau}}{\left(\frac{1}{2\tau}\right)^2 - \left(\Delta\omega^2 - \frac{1}{2\gamma}\right) - \frac{i\Delta\omega}{\tau}} \\ a_{CCW} &= \tfrac{1}{\sqrt{2}}(a_+ - a_-) &&= \tfrac{\kappa s}{2} \tfrac{\frac{1}{\gamma}}{\left(\frac{1}{2\tau}\right)^2 - \left(\Delta\omega^2 - \frac{1}{2\gamma}\right) - \frac{i\Delta\omega}{\tau}} \end{aligned} \tag{2.11}$$

$$t = s - \kappa a_{CW} \quad \text{and} \quad r = \kappa a_{CCW} \tag{2.12}$$

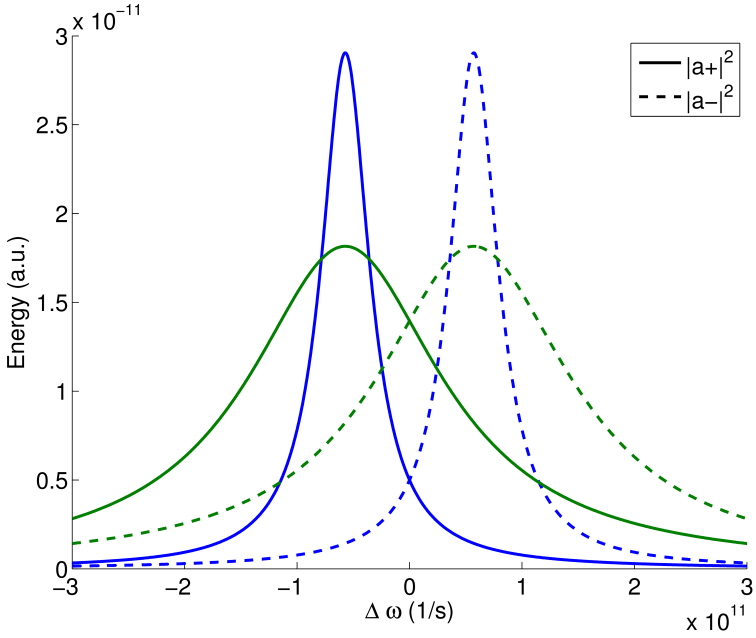

Figure 2.8: The Lorentzian-shaped eigenmodes of the microring for high (green) and low (blue) losses. The high-loss spectra are rescaled for visibility.

A brief inspection of the behaviour of the CW mode (and thus the microring transmission) for different resonator losses and modal coupling values provides more insight in the effect of resonance splitting. Figure 2.9 shows the spectral distribution of the CW mode in the case of high and low resonator losses and for large and small resonance splitting. The intensity for the high loss case has been rescaled for clarity. When the losses are high, small resonance splitting is obscured and the mode profile is approximately Lorentzian, while large splitting results in a flat resonance band. For small losses on the other hand, small splitting already results in a split resonance peak. If the coupling between CW and CCW mode is strong, the resonance splitting can be so severe that it results in two completely separated peaks. Resonance splitting is investigated in more detail in chapter 5. Although resonance splitting has proven an asset in determining the size of individual particles using ultra-high quality resonators [5], it has a detrimental effect on the performance in the simple evanescent field sensing we introduce in the next section.

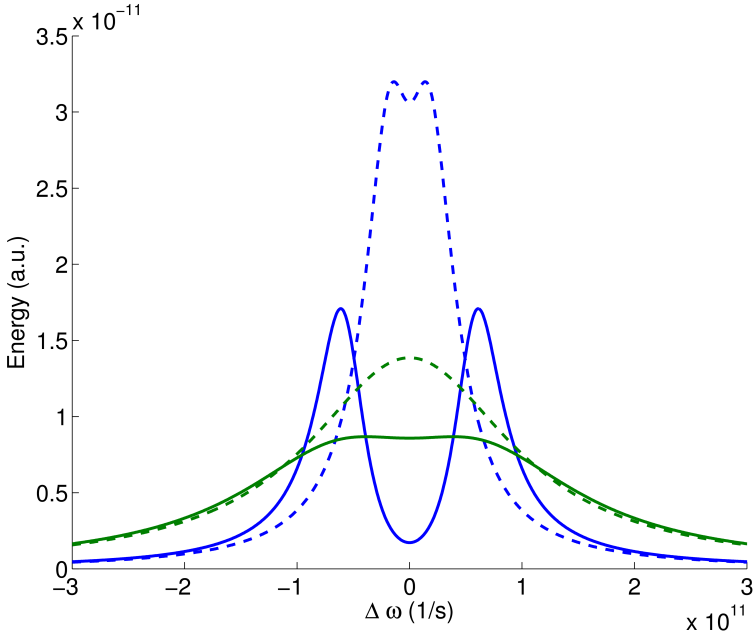

Figure 2.9: The CW mode in the microring for low (blue) and high (green) losses and large (full line) and small (dashed line) splitting. Depending on the relation between losses and mutual coupling, the resonance shape varies significantly. The high-loss spectra are rescaled for visibility.

2.4 Evanescent field sensing with ring resonators

A label-free microring resonator biosensor can directly measure selective affinity interactions between analyte molecules and receptor molecules on the ring waveguide surface. As most biological molecules have a higher refractive index than the surrounding aqueous environment, the binding of such a molecule to the waveguide will locally increase the refractive index. The evanescent tail of the optical field will sense this changing refractive index and it will result in a change in effective index of the waveguide mode. As the ring resonance wavelength is directly proportional to the effective index, this change in effective index in the ring will induce a shift of the resonance wavelength of the microring. For high-index contrast material systems like SOI, the mode is strongly confined to the waveguide core. The high intensity at the waveguide edge explains the high sensitivity to index changes in the immediate vicinity of the chip surface. In [6], it is determined that the 1/e decay length of the optical

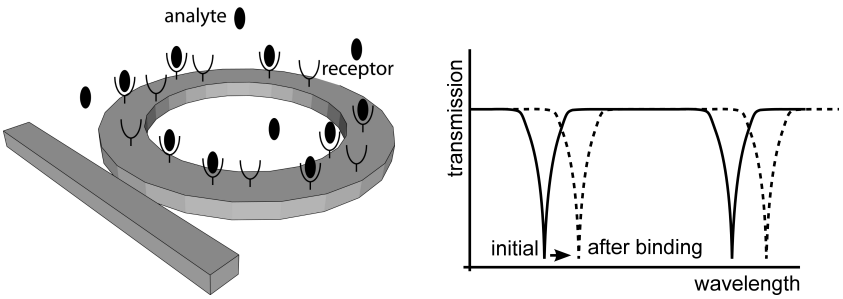

Figure 2.10: Label-free ring resonator sensor with chemically-functionalized waveguide surface. The target molecules present in the sample bind to the receptors on the ring and increase the effective index of the optical mode in the ring waveguide. This results in a resonance wavelength shift in the output signal. The resonance shift depends on the affinity between probe and target and the analyte concentration.

mode for 500 nm wide SOI waveguides in water is only 63 nm. This strong exponential decay of the evanescent field for increasing distance to the waveguide limits the effect of noise inducing index changes in the bulk of the liquid.

The binding of target molecules to an all-pass microring waveguide and resulting wavelength shift are displayed in figure 2.10. Continuous monitoring of the resonance wavelength of a microring resonator leads to the recording of a binding curve like in figure 2.11. This shows the typical timetrace during a biosensing experiment. First, the reference wavelength is established by flowing a buffer solution over the sensors. When switching to the sample solution, the bulk refractive index change causes the sensors to shift abruptly. When the target molecules in the sample solution bind to the ring surface, the effective index of the optical mode in the ring changes and the resonance wavelength of the resonator gradually increases. When the ratio between the bound molecules on the surface and the molecules in solution reaches equilibrium, the sensor signal saturates. The dynamics of this binding curve can provide information about the concentration of the sample, or the affinity between probe and target. A very steep slope in the binding curve indicates a high sample concentration or a strong affinity. The stationary fluidic boundary layer on the surface forms an important limitation of the interaction between the molecules in solution and the chip surface. Only molecules diffusing through this boundary layer can reach the sensor. After switching back to the buffer solution, the bulk refractive index change causes another abrupt wavelength shift in the sensors. When the buffer solution is flowing over the sensor again, some target molecules and non-

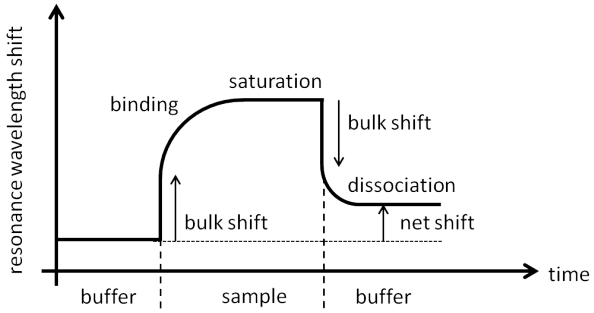

Figure 2.11: Schematic binding curve for a biosensing experiment. The switching between sample fluids induces a bulk index change and causes an abrupt change in resonance wavelength. Binding of the target molecules to the surface increases the resonance wavelength. When switching back to buffer, a net change is recorded after a short dissociation sequence.

specifically adsorbed molecules can dissociate from the sensor surface which causes a further reduction in the sensor signal. The net shift recorded at the end of the experiment is proportional to the amount of molecules bound to the chip surface. Taking into account the first order dispersion in the SOI waveguides, the resonance wavelength shift is readily calculated to be:

$$\Delta\lambda = \frac{\lambda \Delta n_{eff}}{n_g} \tag{2.13}$$

Equation 2.13 also shows that the microring sensor reacts to anything that has an effect on the refractive index of the mode. This makes it a very versatile sensor that can be used not only for biosensing, but also for diverse applications like pressure sensing [7] or temperature sensing [8]. One could also determine the bulk refractive index of a liquid if a known calibration liquid is used. Recently, dual polarization microrings have been used to solve the ambiguity between layer thickness and layer density inherent to single-mode sensors. This provides the ability to detect conformal changes in molecules [9]. On the other hand, when using the rings as a biosensor, all changes in the effective index not due to the target molecule have to be considered as noise in the experiment and increase the detection limit of the microring sensors. The temperature sensitivity of the ring sensors is determined to be about 65 pm/°C [10] and the bulk sensitivity to refractive index unit (RIU) changes is 70 nm/RIU [11]. This implies a very high degree of temperature stability is required for the operation of the sensors. The fluid flow has to be carefully controlled too. Alternatively, reference

sensors can be implemented to eliminate these collective effects from the sensor signal. Another important factor is the surface of the sensors. This has to be chemically functionalized to strongly bind the target molecules while avoiding any non-specific interactions with contaminants in the sample. Careful control over the chemical interface of the chip has led to a wide variety of microring biosensing applications ranging from protein or antibody detection [12–19] to the detection of nucleic acids [20–22] or even entire pathogens like bacteria or virusses [23, 24]. In this work we focus on the detection of complementary DNA sequences, which is discussed in detail in the next chapter.

References

[1] W. R. McKinnon, D. X. Xu, C. Storey, E. Post, A. Densmore, A. Delâge, P. Waldron, J. H. Schmid, and S. Janz. *Extracting coupling and loss coefficients from a ring resonator.* Optics Express, 17(21):18971–82, October 2009.

[2] T. J. Kippenberg, S. M. Spillane, and K. J. Vahala. *Modal coupling in traveling-wave resonators.* Optics Letters, 27(19):1669–71, October 2002.

[3] B. E. Little, J. P. Laine, and S. T. Chu. *Surface-roughness-induced contradirectional coupling in ring and disk resonators.* Optics Letters, 22(1):4–6, January 1997.

[4] B. Little, S. Chu, H. Haus, J. Foresi, and J.-P. Laine. *Microring resonator channel dropping filters.* Journal of Lightwave Technology, 15(6):998–1005, June 1997.

[5] J. Zhu, S. K. Ozdemir, Y.-F. Xiao, L. Li, L. He, D.-R. Chen, and L. Yang. *On-chip single nanoparticle detection and sizing by mode splitting in an ultrahigh-Q microresonator.* Nature Photonics, 4(1):46–49, January 10 2010.

[6] M. S. Luchansky, A. L. Washburn, T. a. Martin, M. Iqbal, L. C. Gunn, and R. C. Bailey. *Characterization of the evanescent field profile and bound mass sensitivity of a label-free silicon photonic microring resonator biosensing platform.* Biosensors & bioelectronics, 26(4):1283–1291, July 2010.

[7] E. Hallynck and P. Bienstman. *Integrated Optical Pressure Sensors in Silicon-on-Insulator.* Photonics Journal, IEEE, 4(2):443–450, April 2012.

[8] H. Xu, M. Hafezi, J. Fan, A. Migdall, G. Strouse, Z. Ahmed, and J. Taylor. *Photonic temperature sensor based on microring resonators.* In CLEO: 2013, page CM4O.1. Optical Society of America, 2013.

[9] J.-W. Hoste, S. Werquin, T. Claes, and P. Bienstman. *Conformational analysis of proteins with a dual polarisation silicon microring.* Optics Express, 22(3):2807–2820, Feb 2014.

[10] T. Claes. *Advanced Silicon Photonic Ring Resonator Label-free Biosensors.* PhD thesis, Ghent University, 2012.

[11] K. D. De Vos, I. Bartolozzi, E. Schacht, P. Bienstman, and R. Baets. *Silicon-on-Insulator microring resonator for sensitive and label-free biosensing.* Optics Express, 15(12):7610–7615, 2007.

[12] D.-X. Xu, M. Vachon, A. Densmore, R. Ma, A. Delâge, S. Janz, J. Lapointe, Y. Li, G. Lopinski, D. Zhang, Q. Y. Liu, P. Cheben, and J. H. Schmid. *Label-free biosensor array based on silicon-on-insulator ring resonators addressed using a WDM approach.* Optics letters, 35(16):2771–3, August 2010.

[13] A. Densmore, D. Xu, N. A. Sabourin, H. Mcintosh, P. Cheben, J. H. Schmid, R. Ma, M. Vachon, A. Delâge, W. Sinclair, J. Lapointe, Y. Li, G. Lopinski, B. Lamontagne, and S. Janz. *A Fully Integrated Silicon Photonic Wire Sensor Array Chip and Reader Instrument.* Optics Express, pages 350–352, 2011.

[14] K. De Vos, J. Girones, T. Claes, Y. De Koninck, S. Popelka, E. Schacht, R. Baets, and P. Bienstman. *Multiplexed Antibody Detection With an Array of Silicon-on-Insulator Microring Resonators.* IEEE Photonics Journal, 1(4):225–235, October 2009.

[15] K. De Vos, J. Girones, S. Popelka, E. Schacht, R. Baets, and P. Bienstman. *SOI optical microring resonator with poly(ethylene glycol) polymer brush for label-free biosensor applications.* Biosensors & Bioelectronics, 24(8):2528–2533, April 15 2009.

[16] M. Iqbal, M. A. Gleeson, B. Spaugh, F. Tybor, W. G. Gunn, M. Hochberg, T. Baehr-Jones, R. C. Bailey, and L. C. Gunn. *Label-Free Biosensor Arrays Based on Silicon Ring Resonators and High-Speed Optical Scanning Instrumentation.* IEEE Journal of Selected Topics in Quantum Electronics, 16(3):654–661, 2010.

[17] A. L. Washburn, L. C. Gunn, and R. C. Bailey. *Label-Free Quantitation of a Cancer Biomarker in Complex Media using Silicon Photonic Microring Resonators.* Analytical Chemistry, 81(22):9499–9506, 2010.

[18] M. S. Luchansky and R. C. Bailey. *Rapid, multiparameter profiling of cellular secretion using silicon photonic microring resonator arrays.* Journal of the American Chemical Society, 133(50):20500–6, December 2011.

[19] M. S. Luchansky, A. L. Washburn, M. S. McClellan, and R. C. Bailey. *Sensitive on-chip detection of a protein biomarker in human serum and plasma over an extended dynamic range using silicon photonic microring resonators and sub-micron beads.* Lab on a chip, 11(12):2042–4, June 2011.

[20] A. J. Qavi and R. C. Bailey. *Multiplexed detection and label-free quantitation of microRNAs using arrays of silicon photonic microring resonators.* Angewandte Chemie (International ed. in English), 49(27):4608–11, June 2010.

[21] A. J. Qavi, J. T. Kindt, M. a. Gleeson, and R. C. Bailey. *Anti-DNA:RNA Antibodies and Silicon Photonic Microring Resonators: Increased Sensitivity for Multiplexed microRNA Detection.* Analytical chemistry, 83(15):5949–56, August 2011.

[22] A. J. Qavi, T. M. Mysz, and R. C. Bailey. *Isothermal Discrimination of Single-Nucleotide Polymorphisms via Real-Time Kinetic Desorption and Label-Free Detection of DNA Using Silicon Photonic Microring Resonator Arrays.* Analytical chemistry, 83(17):6827–33, September 2011.

[23] S. Janz, D. Xu, M. Vachon, N. Sabourin, P. Cheben, H. Mcintosh, H. Ding, S. Wang, J. H. Schmid, A. Delâge, J. Lapointe, A. Densmore, R. Ma, W. Sinclair, S. M. Logan, R. Mackenzie, Q. Y. Liu, D. Zhang, G. Lopinski, O. Mozenson, M. Gilmour, and H. Tabor. *Photonic wire biosensor microarray chip and instrumentation with application to serotyping of Escherichia coli isolates.* Optics Express, 21(4):3243–3245, 2013.

[24] M. S. McClellan, L. L. Domier, and R. C. Bailey. *Label-free virus detection using silicon photonic microring resonators.* Biosensors & bioelectronics, 31(1):388–92, January 2012.

3

DNA detection with microring biosensors

In this chapter, the application of the microring resonators as optical biosensors for complementary deoxyribonucleic acid (DNA) detection is discussed in detail. In a first section, we introduce the measurement setup and address the optical and fluidic components and the software developed to perform the measurements. The second section deals with the optical characteristics of the microring sensors and establishes an optical detection limit by analysing the noise influences during the measurements. The fundamentals of the chemical modification of the chip surface are discussed in the next section and finally some results for the experimental detection of complementary DNA sequences are presented. From these results a calibration curve for DNA detection is obtained and an experimental detection limit is extrapolated. Because of the inherent multidisciplinarity of this topic, the results discussed in this chapter follow from the close collaboration with the Polymer Chemistry and Biomaterials Group (PBM) of Ghent University. The chemical modifications to the chip surface are performed by Arne Goes and Anabelle Van Eeghem. They have also contributed significantly to the biosensing experiments discussed in the final section.

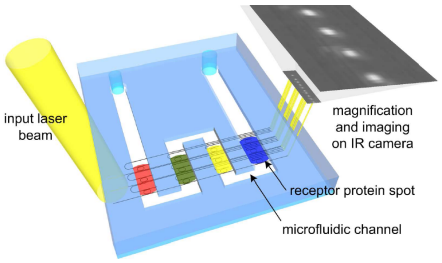

Figure 3.1: Optical sensor chip with functionalized detection array and optical and fluidic interface as proposed by Katrien De Vos [1].

3.1 Measurement setup

The biosensing experiments with the microring resonator sensors are performed on an in-house optical setup in the clean-room in Zwijnaarde. A clean-room is in no way a requirement for the optical sensors, but the availability of all tools required for packaging and preparation of the samples facilitates logistics considerably. This section discusses the optical components of the measurement setup and the microfluidics that play an important role in dispensing the analyte to the sensors. The software that was developed to control and analyze the measurements is also presented. A schematic representation of a sensing chip with optical and fluidic interface is shown in figure 3.1. Descriptions of different measurement systems for similar microring resonator arrays can be found in [2] or [3].

3.1.1 Optics

The complete optical setup is shown in figure 3.2a. On the schematic visualization of figure 3.2b, the different components are indicated. Central is the photonic chip (1) which contains the chemically functionalized microring sensors, in- and output grating couplers and optical waveguides to route the light between the different components. Microfluidic channels (2) are packaged on the chip surface to allow a steady flow of sample fluid over the optical sensors. The fluidics are discussed in more detail in section 3.1.2. Chip and microfluidic channels are mounted on a temperature-stabilized stage with a custom chuck (3). The input laser light is collimated by a collimating lens (4) to achieve a large alignment tolerance and a high robustness again mechanical vibrations. The light coupled out of the chip by the output grating couplers is recorded by a Xenics Xeva-1.7-320 infrared camera mounted on an optical microscope (5). Camera, collimating lens and chuck are mounted on alignment stages to

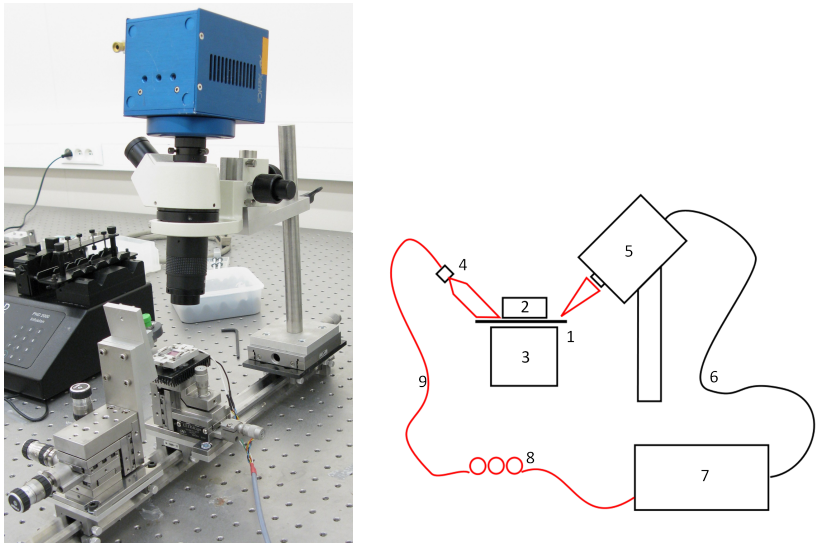

(a) **(b)**

Figure 3.2: (a) Picture of the optical setup showing the microscope-mounted camera and the alignment stages for laser collimator and sample chuck. (b) Schematic representation of the optical setup.

allow easy and accurate alignment of the different optical components. The microscope provides sufficient magnification of the output light combined with straightforward focusing on the camera array. An analog trigger cable (6) connects the camera to a Santec TSL-510 tunable laser source (7). The trigger cable is required to synchronize the camera and the laser during the recording of the wavelength sweeps to obtain the microring spectra. A computer is used to control laser and camera and to process the obtained data. The light emitted by the laser source is passed through polarization wheels (8) to select the TE polarization of the optical mode. This is necessary because the grating couplers on the chip are highly polarization-dependent and are optimized for TE-polarized light. An optical fiber (9) transmits the light from the tunable laser to the collimating lens where it is coupled into the chip.

3.1.2 Fluidics

For the microfluidic interface of the silicon photonic sensor chip, we rely of the process developed by Katrien De Vos which is described in detail in [1]. Microfluidic channels are fabricated in Polydimethylsiloxane (PDMS). The fabrication procedure is straightforward and produces channels for up to 50 chips

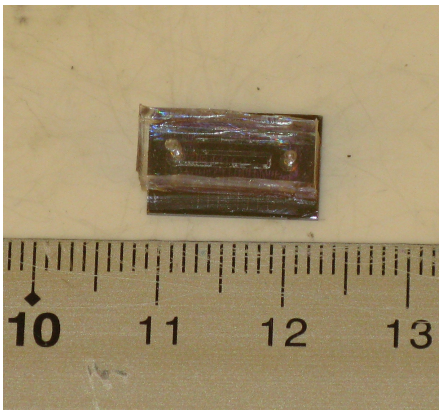

Figure 3.3: Optical chip packaged with PDMS microfluidic channel. The in and outlet of the channel are visible. The optical interfaces of the chip are not covered by PDMS.

at the same time. The channels are cured on an imprint mold for three hours at 80°C to enable maximum polymerization of the silicone. The cured PDMS channels are manually cut from the mold and holes are punctured through from top to bottom to allow integration with standard microfluidic tubing. The mold consists of SU-8 channel patterns on a silicon wafer. It can be reused several times by curing new PDMS after all microfluidic channels are removed. The piece of PDMS containing the microfluidic channels is typically 1 cm thick. Channel dimensions are determined by the SU-8 pattern of the mold. The cross section of the fluidic channel is 50 μm high and 350 μm wide. When designing microfluidic channels for this cast-and-cut procedure, one has to take into account enough margin to avoid errors during the manual cutting of the PDMS from the mold. Careful and skilled hands can typically cut the PDMS with about 1 mm accuracy. To facilitate the connection to the fluidic channels by puncturing the PDMS with a needle, the channels end in 1.5 mm diameter circles.

The silicon chip with the sensor array is then packaged with the PDMS microfluidic channels to obtain a disposable device which combines fluidic channels and optical transducer on a single chip, as shown in figure 3.3. By treatment in an air plasma for 5 minutes, the chip and channel surface are oxidized to improve adhesion between both. Using a flip-chip bonder, chip and channels are aligned with respect to each other and a short heating sequence up to 135°C for about 15 minutes suffices to keep the microfluidic channels in place on the silicon-chip surface. When a bare silicon chip is used, this heating sequence results in strong irreversible Si-O-Si bonds between the channels and

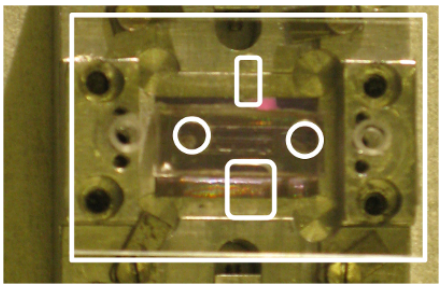

Figure 3.4: The custom chuck with optical chip and clamp to avoid leaking of the microfluidic channels. The openings are emphasized for improved contrast and serve as inlets for the fluidic tubing and to pass optical signals.

the chip. However, when bonding the channels on a nitride covered silicon chip, the bond is not strong enough to avoid leaking channels. Therefore, we have designed a clamp (see figure 3.4) for the chip chuck that exerts an equally distributed pressure on the channels. This keeps channels and chip together and avoids the leaks that were prevalent at the start of this research. The clamp is easily placed on the chuck and by tightening two screws, chip and channel are kept in place.

The microfluidic channels on the chip are connected to standard commercial microfluidic tubing. This tubing is used to dispense the sample fluids to the chip using a syringe mounted on a pump. For efficient switching between liquids, we make use of a 6-port valve with two settings: load and inject. Figure 3.5 schematically representations the valve functionality. In the load position, the inlet of the valve is directly connected to the outlet which sends the fluids to the chip. With this setting, a sample loop can be loaded with sample without affecting the flow of liquid over the chip. It is established that the best way of filling the sample loop is by sucking it full with the required sample by submerging the inlet of the loop in an Eppendorf tube while a negative pressure is applied at the outlet by a syringe. This way, the loop is filled by sucking the sample in and air bubbles can easily be avoided. By switching the valve to the inject position, the sample loop is switched between the in and output of the valve. The valve now guides fluid through the sample loop. The contents of the sample loop are pushed forward and leave the valve through the outlet to the chip. When the volume of the sample loop is dispensed to the chip, the fluid is automatically replaced by the original buffer, without requiring any action of the user. To fill the sample loop again, the valve has to be switched back to the load position.

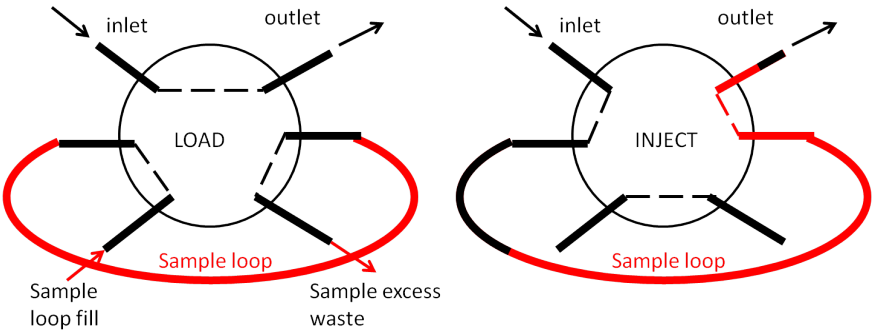

Figure 3.5: Schematic representation of the valve functionality. In the inject position, the sample loop is injected between inlet and outlet and the sample (in red) is pushed to the sensor array.

3.1.3 Measurement software

The measurements are controlled by software developed in-house in collaboration with Michael Vanslembrouck. The software framework controls the infrared camera and tunable laser source to obtain the spectra of the microring resonators. The code is written in the Python programming language [4] to allow adaptations and additions by users with different preferences. The objective of the software is to execute wavelength sweeps with the tunable laser and record the output power of the microrings with the camera to generate the spectra. Lorentzian fits are performed to automatically obtain the resonance wavelengths of the microring spectra and a live binding curve is generated for the user by recoding a time trace. At the start of this PhD, similar software was available but this worked very slowly because of the stepped sweep of the tunable laser. Therefore, we implemented a different protocol, namely the continuous tuning of the laser wavelength while recording camera images at a high framerate. The synchronization between laser and camera is achieved by connecting both devices with a trigger cable. During a sweep of the laser wavelength, the laser sends trigger pulses to the camera at fixed wavelength intervals. When the camera receives a trigger, the current frame is sent to the computer and buffered for processing. To obtain a high wavelength resolution, specific hardware to handle high data rates is required, as a classical USB interface does not have sufficient bandwidth. Therefore, the computer is equipped with a frame-grabber card and a large-bandwidth cable connection to the camera. To record microring spectra with a wavelength resultion of 5 pm at a sweep speed of 2 nm/s, the output grating couplers of the optical chip are imaged at a framerate of 400 Hz. In the output image, each grating coupler is assigned a monitor of 4 by 4 pix-

els and the average pixel value is stored for every wavelength. This averaging has the advantage of limiting noise-inducing intensity oscillations. After each sweep, the data is automatically processed by fitting Lorentzian shapes to the resonance curves to provide the next point of the binding curve to the user. This results in an average time resolution of the binding curve of 7.8 s. This timestep is limited by a slow initialization of the tunable laser, which takes up to 5 seconds between wavelength sweeps. Compared to the time resolution at the start of this project (420 s), this is a tremendous improvement of the measurement rate. It allows the monitoring of reaction dynamics on the sensor surface and previously obscured transient effects are visualized.

3.2 Microchip performance

In this section we describe the photonic chip used for the majority of the DNA detection experiments. Compared to previous chip designs, the number of sensors is increased significantly, the possibility to implement reference sensors is added and the microring resonators have optimized design parameters. Key performance indicators such as optical detection limit are provided and important noise contributions are discussed.

3.2.1 Microchip layout

The chip layout is shown in figure 3.6. The chip consists of three distinct regions. In the input part, light is coupled into the chip using four vertical grating couplers. These grating couplers have an efficiency up to 5 dB and a 1 dB bandwidth of 45 nm as reported in [5]. These input couplers are illuminated by a collimated laser beam to enable robust alignment of the optical setup. Once the light is coupled to the waveguides on the chip surface, several 3 dB splitters distribute it and guide it to the sensor array. The sensor array itself consists of 64 sensors. These are grouped in 32 pairs. The sensors are paired to allow the possibility of combining each sensor with a reference sensor. By implementing reference sensors in an experiment, environmental variations like bulk refractive index changes or temperature changes can be compensated. It suffices to protect the reference sensors from the target molecules to obtain the reference signals. We have experimented with photopatternable Cyclotene [6], a polymer derived from B-staged bis-benzocyclobutene (BCB). Windows over the sensing rings are opened lithograpically while the reference sensors are covered by the polymer. This serves as a very good temperature reference because the thermo-optic coefficient of cyclotene is close to that of water [7]. However, slow diffusion through the polymer layer induces a drift in the reference signals. An additional problem is that these polymer-clad reference sensors are

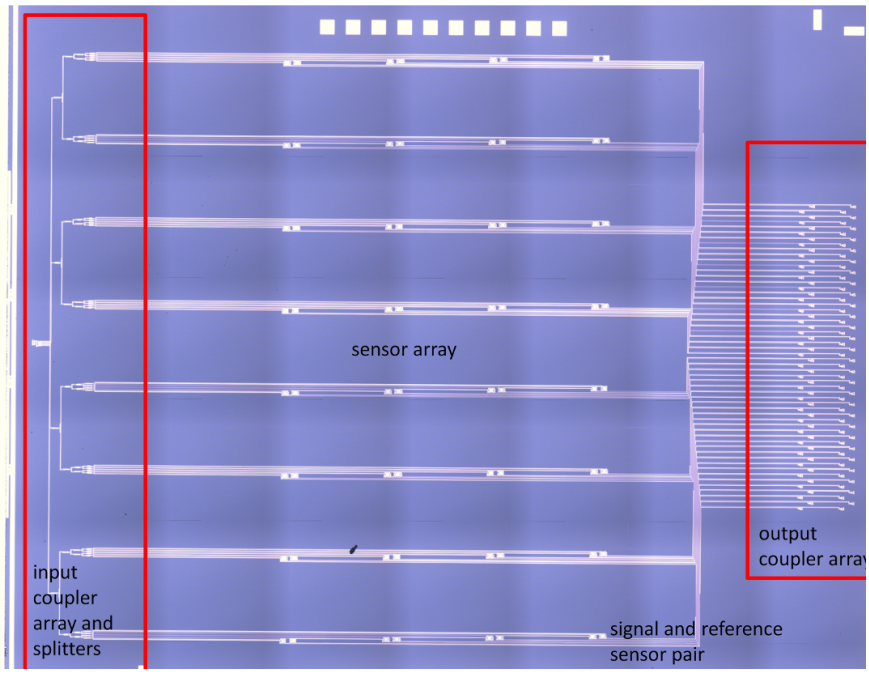

Figure 3.6: Microscope image of the optical sensor chip.

totally isolated from bulk refractive index changes. To allow elimination of bulk changes using reference sensors, it could be better to functionalize them biochemically to avoid non-specific adsorption. Possible coatings that keep the reference sensors exposed to bulk changes while eliminating non-specific binding are polyethylene glycol (PEG) [8] or bovine serum albumin (BSA) [9]. To compare the performance of different sensor implementations, the sensing array combines all-pass and add-drop sensors. The output signals of the microrings are guided to an output coupler array, where grating couplers couple the light out of the chip.

3.2.2 Signal stability and noise contributions

Here we discuss the performance of the microring resonators in the sensing array and several factors that contribute to noise and limit the functionality of the device. An experimental optical detection limit is established. Because the sensing array consist of both all-pass and add-drop sensors, the performance of these two implementations of microring resonator sensors is readily evaluated. Transmission signals of an all-pass and add-drop sensor covered by a phosphate

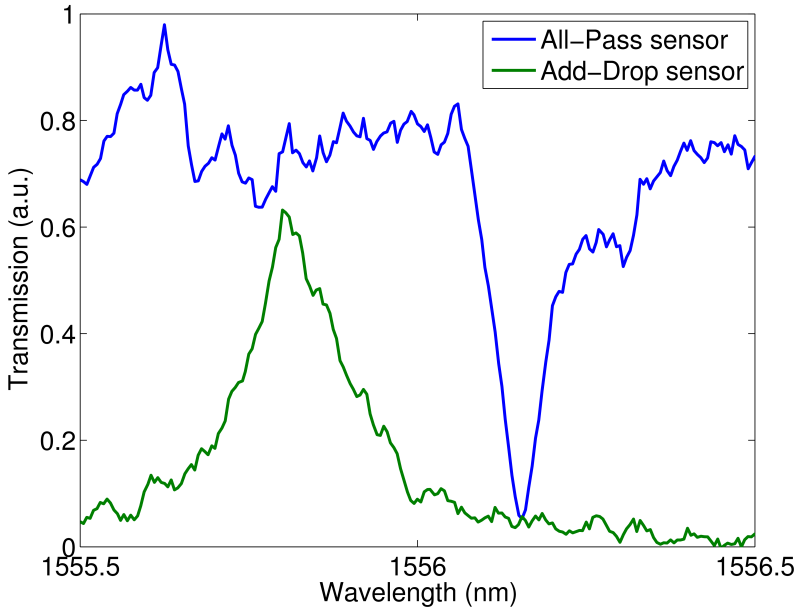

Figure 3.7: Transmission spectrum of microrings in the sensing array. Data is obtained during an experiment in PBS on the optical setup.

buffered saline (PBS) buffer of pH 7.4 recorded on the optical setup are shown in figure 3.7. The resonance shapes are slightly distorted due to various noise contributions, but in the next paragraphs it is demonstrated that these signals are robust enough to result in a highly reliable sensor response.

For the all-pass sensors, the design parameters are obtained from [7]. There it is established that a microring with 16 μm bends and 10 μm straights, a 4 μm long coupling section with a gap of 250 nm results in a close to critically coupled all-pass ring with quality factor of 21000 and a free spectral range (FSR) of 3.6 nm in water. For the add-drop sensors, assymetrical coupling to the microring is necessary to achieve critical coupling. According to Fimmwave [10] simulations, an input coupling section of 4 μm long combined with an output coupling section of 6 μm satisfies the critical coupling condition ($r_1 = r_2 a$, see 2.2.2). This results in an add-drop sensor with a theoretical quality factor of 9000 in water. Notice that a critically-coupled add-drop microring always has a lower quality factor (or wider resonance width) than a comparable all-pass microring because the drop waveguide induces extra losses in the resonator. By reducing the coupling to the waveguides, the resonance width of the add-drop sensor can

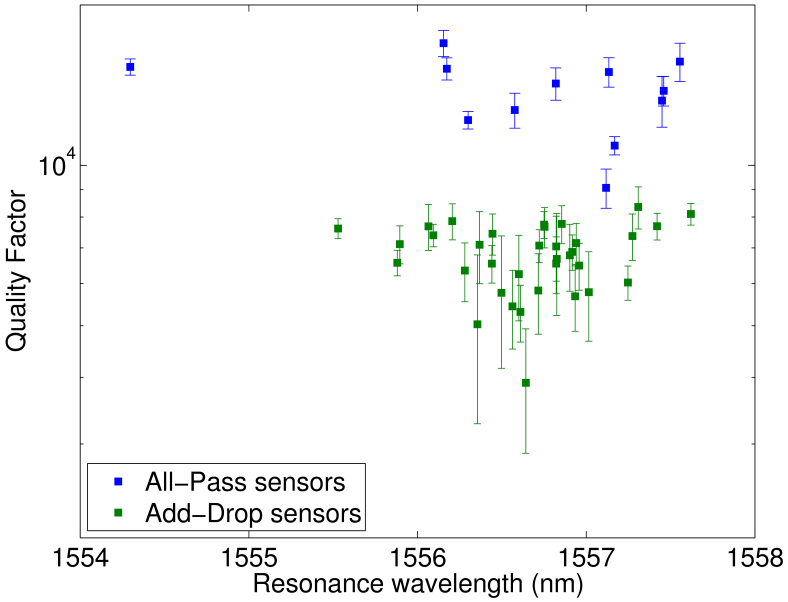

Figure 3.8: Quality factors of microrings in the sensing array during an experiment in PBS on the optical setup. The quality factor of the pass sensors is about twice that of the drop sensors.

be reduced, but this comes at the cost of reduced output power on resonance.

A first metric for the sensor performance we obtain for the microchip array is the resonance width or resonance quality of the sensors. This is an important metric for resonator sensors because the detection limit is directly related to this value [11–13]. Figure 3.8 shows the quality factors of all sensors in the sensing array in a PBS pH 7.4 environment. The quality factors are obtained after fitting a Lorentzian lineshape to the resonances. Error bars show the variation of the calculated Q-factors during 5 minutes of recording and are an indication of the accuracy of the fit. Distortion of the signals due to noise results in variations of the fit parameters. The quality factors for the all-pass sensors range from 9000 to 17000 for nominally identical sensors at different chip positions. This suggests significant processing variations on a chip scale that affect the resonator losses and thus the resonance quality. Another factor that affects the quality of the resonances is resonance splitting. This is apparent for the widest resonances that show significant broadening of the linewidth and even clearly split resonances like in figure 3.9. For such split resonances, a Lorentzian is a poor

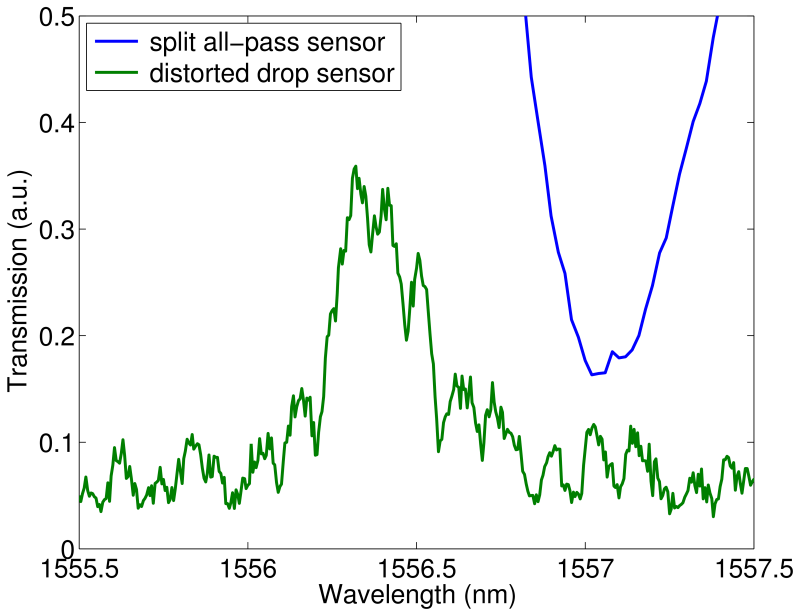

Figure 3.9: Distorted optical signals in the sensing array in PBS. Because of the large difference in resonance width of both signals, the wavelength scale of the pass signal is magnified by four to visualize the resonance splitting.

approximation of the resonance shape. This explains why the lowest Q-factors also show the largest variation in fit parameters. Resonance splitting of microrings is investigated in detail in chapter 5. It is also important to mention that the obtained Q-values are significantly lower that the value of 21000 reported by Tom Claes in [7]. Even though the design parameters of the microrings are identical. This could be caused by a change in the chip processing which results in slight changes to the design parameters. The directional coupler section in particular would have to be reoptimized.

The calculated quality factors of the drop signals vary between 4000 and 9000. Compared to previous generation drop sensors, this is an improvement of the resonance quality by a factor 2, mainly caused by reduced bend losses and optimized coupler sections. Here it are again the lowest Q-factors that show the strongest variations. Indeed, these wide resonances are significantly distorted and a Lorentzian is a poor estimation of their shape. Because of the lower quality factors of add-drop resonators compared to all-pass rings, it is unlikely

these signals are much affected by resonance splitting. The distorted drop signal from figure 3.9 shows that a periodic perturbation of the transmission forms an important contribution to the noise on the signal. This can be attributed to interference between light coupling directly into the waveguide and light reflecting from the substrate before coupling into the waveguide. This effect is investigated in detail in chapter 4. Other contributions to the noise are intensity oscillations due to mechanical vibrations. At the input side, this effect is significantly reduced by coupling light into the chip using a broad collimated light beam rather than fragile optical fibers. At the output side on the other hand, the camera mounted on the microscope still picks up ambient vibrations. By integrating the output intensity over the pixels of the grating monitor, this effect is suppressed but not eliminated. Because of their wider resonance shape, the drop signals are more prone to distortions due to the interferences or vibrations.

Although this analysis of resonance quality provides interesting insights in the sensor performance, the most important metric of the microring biosensor is still the stability of the resonance wavelength. Using a combination of theory and simulations, the noise on the resonance wavelength after fitting was previously established to be about 0.4 pm [8] for our optical setup. However, a more rigorous approach is to take an actually recorded binding curve and extract the variations on those resonance wavelengths.

Obviously, the stability of the binding curve is strongly dependent on the applied fitting algorithm and the type of sensor. We have evaluated several approaches, all based on a Lorentzian fit of the resonance shape. For an all-pass sensor, a Lorentzian fit with a width of 100 pm around the resonance wavelength provides the best result. The width is determined to include sufficient data points for a robust fit while keeping the fitting window narrow enough to ensure an accurate description of the resonance shape, since the Lorentzian description is only accurate close to the resonance wavelength. A fitting window of 100 pm has approximately the width at half maximum of the pass signals and yields the most stable results. For the wide signals in the add-drop filters, a fitting window of 200 pm has to be used. Additional information is available from the sensing array for the drop signals. Indeed, the pass ports corresponding to the drop ports can also be used, since every add-drop sensor also has a pass waveguide that is routed to the output array. By including the information of the pass signals to normalize the drop signals, the influence of distortions such as the interferences can be suppressed as these are equally strongly present in the pass ports. A comparison of the different sensor signals and the corresponding fit results is presented in figure 3.10.

The variation of the resonance wavelength for the optical sensors in a PBS pH 7.4 environment is evaluated using the optimized fitting algorithms. To evaluate the standard deviation of the sensors, the signals are corrected for a linear

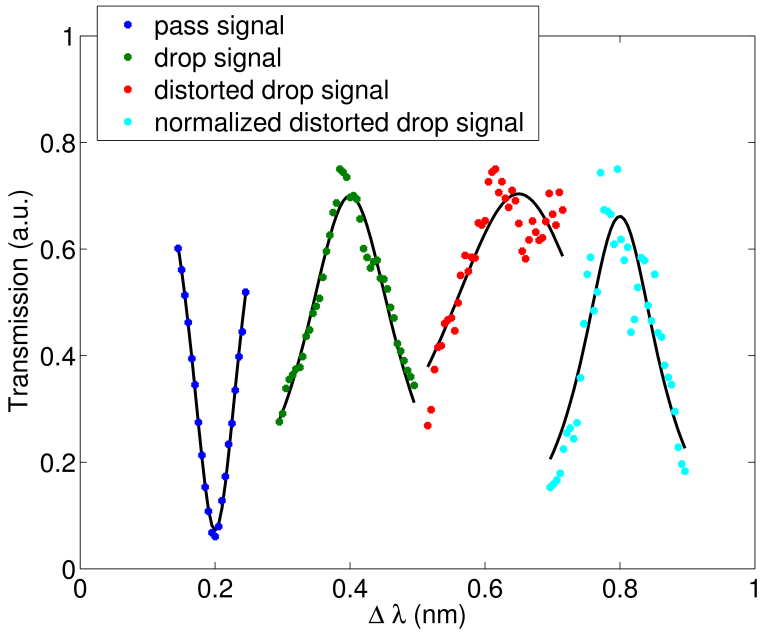

Figure 3.10: Resonance signals and corresponding fit results for all-pass sensor and add-drop sensors.

all-pass sensor	add-drop sensor	normalized add-drop sensor
1.5 pm	2 pm	0.9 pm

Table 3.1: Standard deviation on resonance wavelength.

drift present in al sensors. This results in the values listed in table 3.1. The add-drop sensors show the strongest variation of the resonance wavelength because of their lower quality factors. However, by implementing the normalization by the corresponding pass signals, the signal is stabilized and the variations are reduced to a level below that of the all-pass sensors.

A time evolution representing the subsequent optimizations to the measurement setup and the fitting algorithm is shown in figure 3.11. In this graph, the record stability of the microring sensors is obtained by coupling light into the chip using an optical fiber and after correction of the signals using the reference sensors. Because of the fast readout of the optical setup, a time averaging can be applied to the reference sensors which results in an additional improvement of the stability. The coupling scheme using an optical fiber eliminates

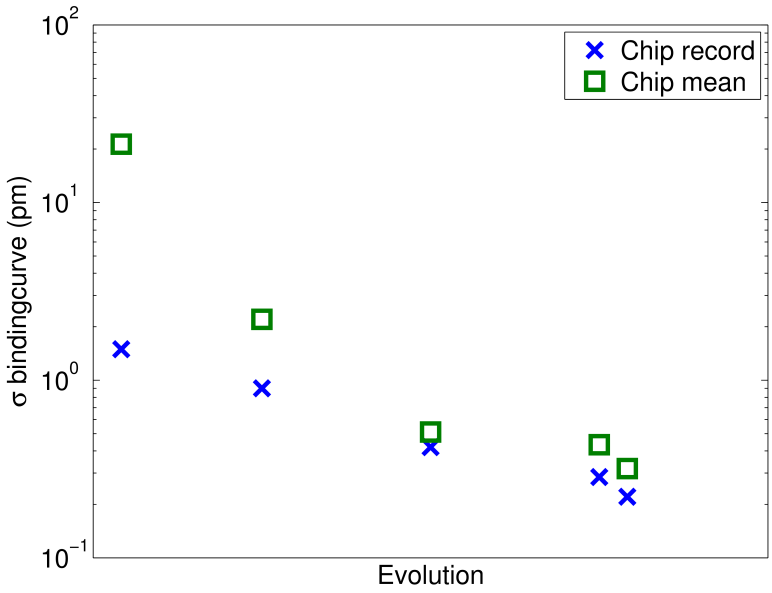

Figure 3.11: Evolution of the standard deviation on a binding curve recorded on the optical setup during consecutive improvements to the measurement method. The reported noise levels correspond to, from left to right: (1) the original noise level (2) the normalization of the drop signals (3) a new sensor array (4) the implementation of reference sensors and (5) the time averaged reference sensors. (3), (4) and (5) are obtained after elimination of parasitic interferences by coupling light to the chip using an optical fiber.

most parasitic interferences, but it has to be noted that it is very susceptible to ambient vibrations. The noise reported in figure 3.11 is a record value and requires a very stable environment, which is often not the case. Under general operating conditions, coupling using a collimated laser beam provides better results, despite the interferences. Because the methods discussed in chapter 4 are expected to improve the performance of the collimated laser beam by eliminating the parasitic interferences, the record optical fiber result is included in the time evolution to establish the optical detection limit of the system. The trend shows a clear decrease in optical noise following consecutive developments, both for the best sensor in the array and for the mean response over the sensor array. The average noise performance of the entire array also comes closer the value for the best sensor, indicating a general stability improvement. The

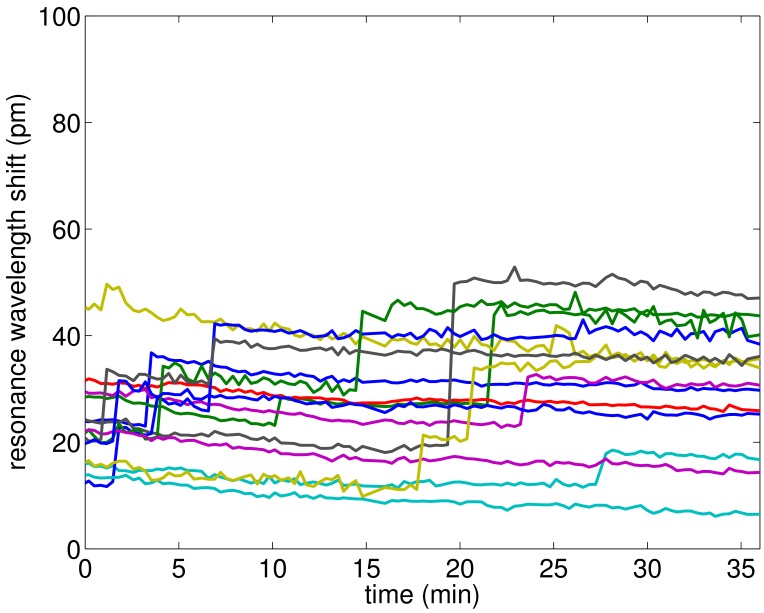

Figure 3.12: Experimental binding curve showing the binding of individual beads to the sensor surface.

lowest recorded variations on the binding curve have a standard deviation of $\sigma = 0.2\,\text{pm}$. Using these results, the optical detection limit of the system can be determined by the 3σ value of the resonance wavelength variations, or 0.6 pm. Notice that this value is an order of magnitude lower than the wavelength step in the recorded spectra, which shows the added value of our optical setup and the fitting algorithms in the stabilization of the signals. This optical detection limit is close to the noise level reported for the commercial system from Genalyte [2] ($\sigma = 0.1\,\text{pm}$), showing that only marginal improvements can be made to the stability of the complete optical system. Keeping in mind the very high sensitivity of the sensors to bulk refractive index changes (70nm/RIU) and temperature changes (60pm/°C), this corresponds to an impressive system stability of the order of 10^{-6} RIU and 10^{-3} °C, partly because these collective effects are compensated by the reference sensors.

3.2.3 Single-bead detection

Using streptavidin-coated beads and biotinilated microring sensors, the response of the optical sensors to beads is evaluated. This experiment is per-

formed to investigate the possibility of amplification of the binding signal for DNA hybridization. The superparamagnetic beads are obtained from Ademtech and can bind a very high amount of biotin up to 800 pmoles/mg [14]. The bead diameter is 500 nm on average. The recorded binding curve during the exposure of the sensors to the bead solution of 7 nM is shown in figure 3.12. This clearly shows discrete binding events indicating single bead sensitivity of the microring sensors. The strong response of the sensors is explained by the very large index contrast between the surrounding PBS buffer and the magnetic particles. The strong difference in wavelength shift between binding events relates to the overlap of the optical mode with the bead. The position of the bead with respect to the optical waveguide has an important effect on the wavelength shift. A second experiment conducted without biotin on the chip surface unfortunately yields the same results. The beads sink to the bottom of the microfluidic channel and stick non-specifically to the sensor surface. This shows that under current operating conditions, this is not a feasible way to amplify the signal of the sensors. Reduced non-specific interaction with the sensors by implementation of a PEG or BSA functionalization could avoid the non-specific bead signal. However, it is unsure if the flow in the microfluidic channel is strong enough to completely prevent the sinking of the heavy beads.

3.3 Chemical modifications

In this section we discuss the chemical modification steps required to enable DNA detection with a silicon nanophotonic chip. In order to selectively bind the target DNA sequence, a complementary probe has to be present on the surface. To covalently bind the organic DNA probe to the anorganic silicon surface, a silanization of the silicon is required. During the experiments, we notice the best reproducibility of the results if the chemical modification steps are performed online on the optical setup. Offline functionalization in the chemistry labs requires several steps where the chips have to be transported during which it is difficult to maintain a clean chip surface. Also the deposition of biochemical layers on the entire chip surface offline, as opposed to only on the transducers inline covers optical components like grating couplers and splitters. This negatively affects the optical transmission of the chip. A final advantage of the online functionalization lies in the fact that the steps are monitored live on the optical setup and resonance wavelength shifts are recorded during the entire functionalization process, which enables quality control. For these reasons, most of the chemical modifications discussed in this section take place in the microfluidic channels on the photonic chip. While online functionalization offers several benefits during the development stage of the biosensing platform, an offline scheme has to be used for the final application, mainly because of the

additional multiplexing flexibility.

3.3.1 Silanization

The first step in the modification of the silicon surface is the silanization. In this step, organic linkers - silanes - react with the silicon surface to covalently bind functional groups to the silicon. These functional groups are used in the following steps to bind the target-specific probes to the biosensor surface. In this work, we have investigated two silanization approaches to detect complementary DNA. The first one binds 3-aminopropyltriethoxysilane (APTES) to the silicon surface before modifying the silane with a hydrazine linker (Hynic) [15], as described in [16]. However, this two-step approach is very time-consuming considering the long reaction time between APTES and the hydrazine (3 hours). In the second approach, commercially modified Hynic silanes [17] are immediately deposited on the silicon surface. This reduces the durating of the experiments considerably and we will focus our attention in this section on the one-step approach.

Just like APTES, the Hynic silane contains a triethoxysilane group. The modification of the silicon surface can thus be performed using the same steps as for an APTES silanization. The silicon chip is treated by a reactive-ion etching (RIE) plasma containing both nitrogen and oxide ions for 0.4 minutes. This plasma activation is performed in a Pico Diener Electronic. The treatment results in an oxidized and activated surface which contains highly reactive $Si(-O)_2$ groups [18]. This plasma activation serves a double purpose because it also enhances the binding of the PDMS microfluidic channels. The Hynic silane on the surface ends by a protecting group, but is activated in water to form a free hydrazine. This deprotection happens automatically after switching to a PBS buffer in the next functionalization step with the formation of aceton. The reaction of Hynic silane on the silicon chip surface is depicted in figure 3.13.

The efficiency of the reaction of the triethoxysilane to a silicon surface is evaluated using fluorescence microscopy. Detailed fluorescence analysis by Stephania Dante indicates that the silanization is most efficient on the parts of the surface that are not optical waveguides, because the fluorescent signal from these areas is much stronger. This is supported by [19], where it is established that fluor residue from etching steps can reduce the efficiency of silane coupling to the silicon waveguides. To neutralize the influence different etchants can have on the sensor performance, it was decided to coat the silicon surface with a thin silicon nitride layer. Fluorescence quenching on the silicon waveguides provides an alternative explanation for the low signal from these waveguides, from this point of view the nitride layer would not be responsible for the observed improved performance. In an Advanced Vacuum Vision 310

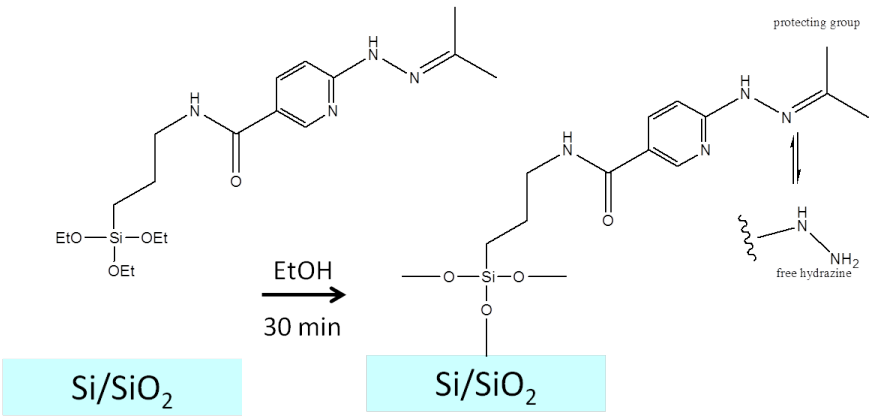

Figure 3.13: Silanization of the silicon surface and deprotection of the Hynic silane.

plasma-enhanced chemical vapour deposition (PECVD) tool, a SiNx layer of 9 nm is deposited on the silicon chip surface. This has only a limited effect on the optical characteristics of the microring sensors because of the very small thickness of the layer. The nitride buffer layer does however eliminate any effect of processing steps on the chemical modification steps of the surface and guarantees an identical chip surface for all functionalization steps. The silanization of the nitride layer does not require any other major changes to the processing, as a plasma oxidation in the RIE is sufficient to activate the surface. In [20] an oxidation time of 30 minutes is suggested, but we find experimentally that 5 minutes suffice for efficient silanization.

A solution of 2% (v/v) Hynic silane in ethanol (EtOH) and 5% dimethylformamide (DMF) is used to deliver the silane to the sensor surface. First a wavelength reference is established by rinsing the sensors with EtOH. By switching the fluidic valve, a sample loop containing the Hynic silane solution is flown over the surface. After a 30 minute reaction time, the chip surface is rinsed by EtOH again. The experimentally-recorded binding curve for the online functionalization with Hynic silane is given in figure 3.14. Different colors correspond to the response of individual sensors. The initial strong increase in the signal is attributed to a bulk index shift caused by the 2% silane solution. After the sample loop, the chip surface is rinsed by EtOH and the bulk refractive index shifts back to the initial value. The residual wavelength shift indicates the amount of Hynic silane that is deposited on the sensor surface. The average shift over all active sensors is 165 pm. Changes in the binding curve are not abrupt because the EtOH in the fluidic channels surrounds the sample loop. While

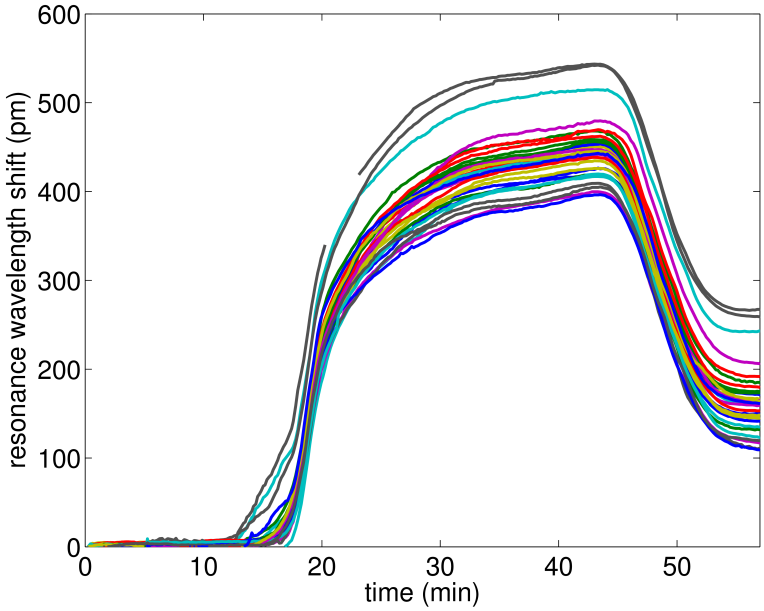

Figure 3.14: Binding curve for the functionalization of the sensors with Hynic silane.

the fluid is pumped over the chip, there is some mixing between the leading and trailing end of the sample loop and the EtOH. This causes a more gradual change in the bulk refractive index step between both liquids. After successful silanization of the microrings, we can proceed with the immobilization of the specific DNA probes on the surface.

3.3.2 Immobilization of DNA probe

Prior to coupling the target specific DNA probes to the chip, they have to be chemically modified with a reactive group to bind with the Hynic silane. This step is performed offline in the chemistry laboratory. The chemical reaction corresponding to this modification is given in figure 3.15.

The DNA probes with the right sequence and a primary amine functional group are purchased from Eurogentech. The sequence of the surface DNA tag is:

$$5' - \text{CTCTCTCTCTCTCTCTCTCTCATGAGTCGTGAGTACGCTT} - 3'$$

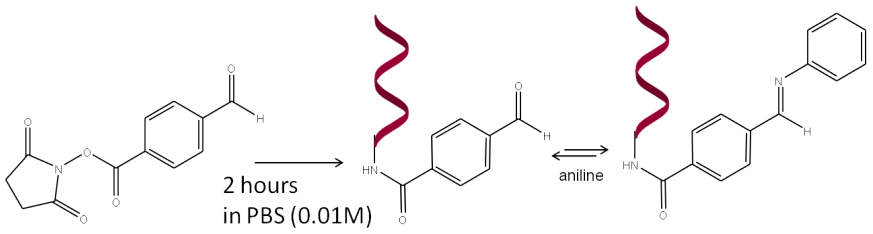

Figure 3.15: Functionalization of the DNA probe with S-4FB.

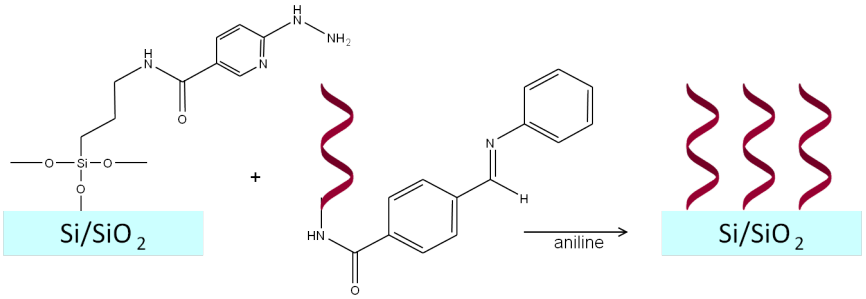

Figure 3.16: Coupling of the DNA probe to the Hynic silane on the chip surface.

This is modified with an amine at the 5' end. The recognition sequence is:

$$5' - \text{CATGAGTCGTGAGTACGCTT} - 3'$$

This is preceded by a CT-spacer sequence to make sure the recognition tag is easily accessible for the complementary target. The DNA strands are dissolved in a solution of succinimidyl-4-formylbenzamide (S-4FB) in PBS (0.01 M) of pH 7.4 to react for two hours. This reaction results in a bond between the primary amine of the DNA sequence and the S-4FB functional group. When the DNA functionalized with S-4FB is brought in a solution containing aniline, the aniline forms a Schiff base which can react efficiently with the Hynic silane on the surface [21]. Therefore, the functionalized DNA probe is dissolved in a PBS buffer (pH 6) with 100 μM aniline for reaction with the chip surface. The probe concentration in this buffer is 1 μM. Because the microfluidic channels contain water at this time, the protected hydrazine is deprotected according to the reaction of figure 3.13. On the surface of the chip, the Schiff base on the functionalized probe reacts with the free hydrazine of the Hynic silane to form a stable hydrazone bond. This reaction is given in figure 3.16.

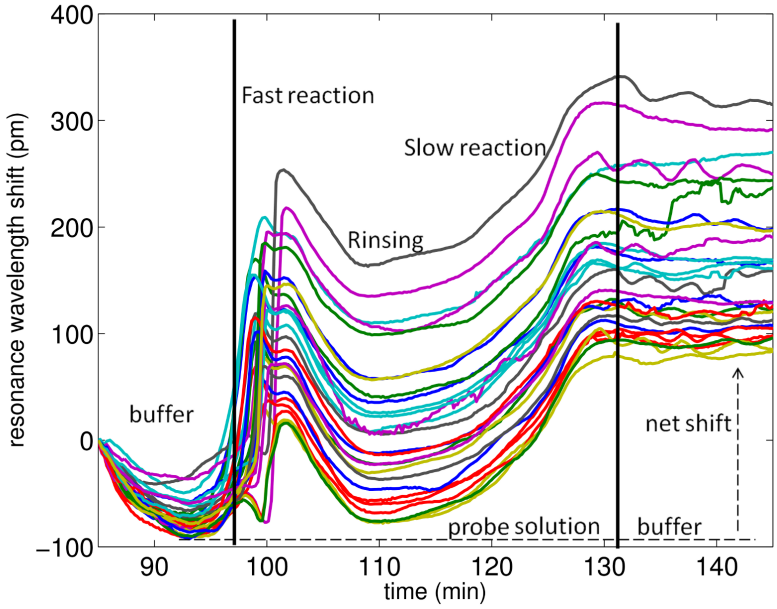

Figure 3.17: Binding curve for the functionalization of the sensors with the target specific DNA probe.

A binding curve representing the binding of the DNA probes to the chip surface is given in figure 3.17. This binding curve is harder to interpret than the straightforward coupling we observed during the silanization. A first thing to notice is the strong variation between individual sensors responses. This can indicate the functionalization of the surface is not homogeneous and some sensors record more binding than others. The response also shows an initial drop in the signal, which is explained by the slow rinsing of the ethanol that remains in the channels after the silanization step. The reaction on the surface starts with a fast association of probes on the surface, corresponding to the abrupt initial shift. While the reaction takes place, deposition of material on the surface is followed by a rinsing stage (the resonance wavelength drops again) to finally stabilize for a net addition of molecules to the surface. The average shift over the active sensors amounts to 160 pm. Over various experiments, the specific shape of the binding curve for probe coupling to the surface can vary significantly, but in general the net shift of the resonance wavelength after the reaction is positive.

3.4 DNA measurements

Once the chip surface is functionalized with the target specific DNA probes, the sensors are equipped to detect the complementary DNA strands. The complementary DNA we detect is representative for Pseudomonas aeruginosa (PA), a bacterium commonly responsible for ventilator-associated pneumonia (VAP) in intensive care units of hospitals. The 84-base sequence is the result of rolling cycle amplification (RCA) [22] of the pathogen DNA and reads:

$$5'- \quad \text{CTCCTCAGTAATAGTGTCTTAC}\textit{AAGCGTACTCACGACTCATG}$$
$$\text{AAATCGCCGGACTGCCGGTGGTCGACAGGTCGGTGTATGCAG} \quad -3'$$

The complement of the surface probe sequence is marked in italic. Strong hydrogen bonds between the complementary sequences of target and probe ensure hybridization of the target strand to the sensor surface. The hybridization happens preferably at 35°C. To improve the efficiency of complementary hybridization, the hybridization buffer consists of 50% formamide in PBS (0.01 M) with pH 7.4. The function of formamide is to favor complementary hybridization over the formation of non-complementary duplexes by destabilizing the double-stranded DNA [23, 24]. To detect the complementary DNA strand, a wavelength reference level is established by flowing hybridization buffer over the sensors. Because of the high refractive index difference between hybridization buffer with formamide and a pH 7.4 PBS buffer, it is very difficult to have buffers without bulk index changes when switching to the sample loop with the target DNA. To create the DNA solution of the required concentration, dilutions are prepared which means the final buffer is never 100% hybridization buffer. Even after several buffer exchange sequences, a bulk index shift upon switching to the diluted DNA solution remains visible. However, by correcting for an identical bulk shift before and after the DNA sample loop, a hybridization profile can be recorded as shown in figure 3.18.

5 minutes after the start of the experiment, the sample loop containing a 10 nM DNA solution reaches the sensor surface and hybridization between the target DNA and the surface probe starts to form double stranded-DNA (ds-DNA). Because many hybridization sites are available, the initial signal ramps up quickly. When the available sites become sparse, the hybridization slows down to eventually reach a steady state when the equilibrium between the target strands in solution and on the surface is reached. After 30 minutes, the pure hybridization buffer replaces the DNA solution again and the signal remains constant. This indicates the hybridization on the surface is permanent and no DNA is rinsed off. The average net shift is 74 pm. It has to be mentioned that this binding curve of figure 3.18 is recorded at room temperature and without nitride layer on the chip surface and was only observed once. A more typical binding curve, which shows a bulk shift during the sample loop but no clear

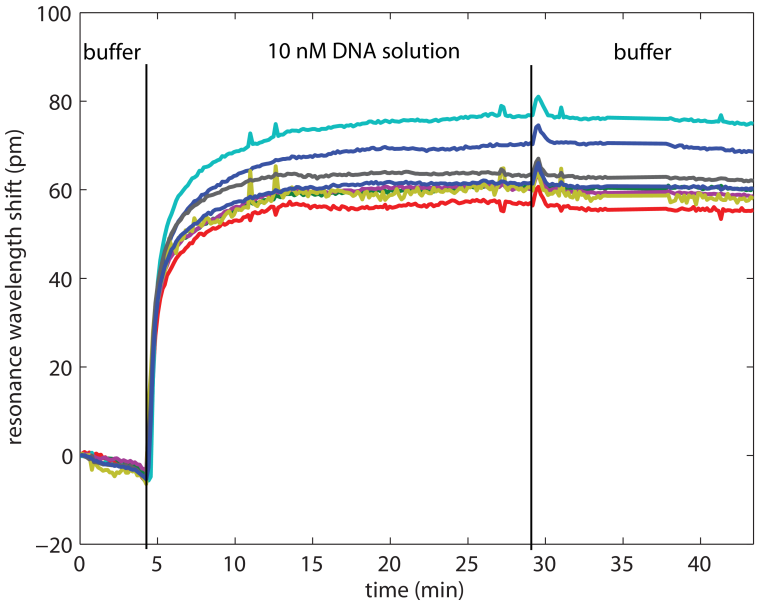

Figure 3.18: Binding curve for the hybridization of the complementary DNA strands on the sensors. Only the net shift is visible as the signal has been corrected for the bulk refractive index shift.

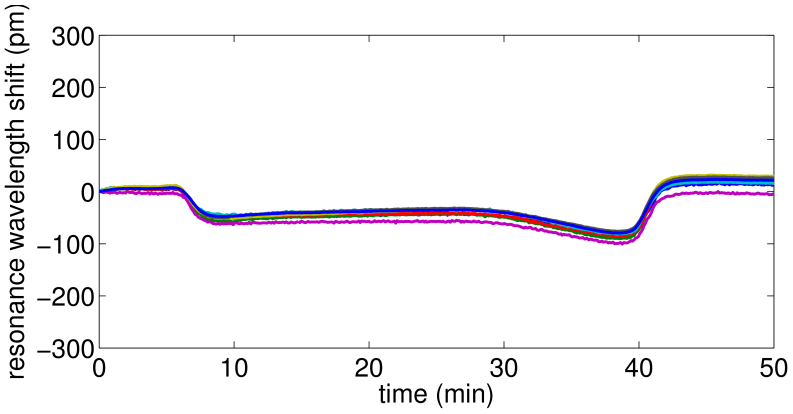

Figure 3.19: The net shift on a typical complementary DNA binding curve for a chip without nitride layer can barely be determined.

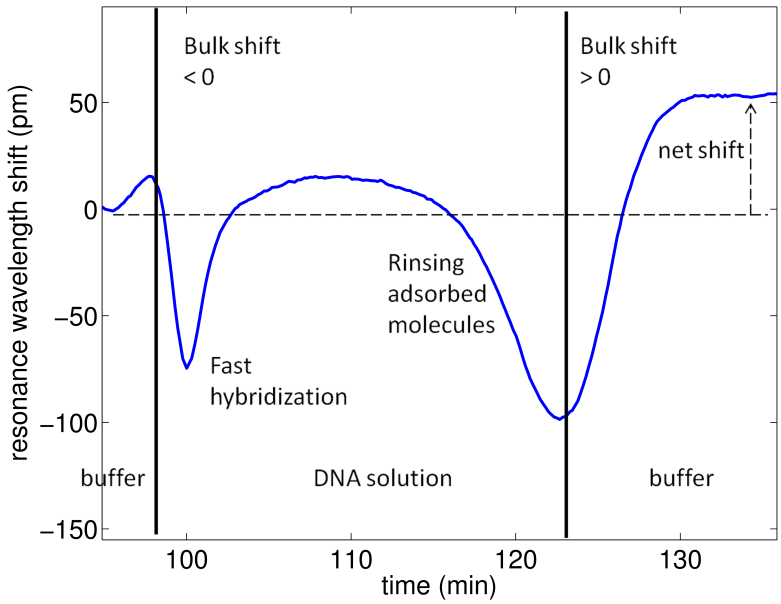

Figure 3.20: A generic binding curve of DNA hybridization with complex transient behaviour.

complementary DNA binding, is shown in figure 3.19. It is precisely for this reason the process has evolved with the implementation of the nitride layer and hybridization at elevated temperature in order to improve reproducability. Under these new conditions described in the previous paragraphs, several successful hybridization experiments are performed. However, these experiments do not lead to a clearly-recorded binding curve, but a net shift can be identified by comparing the resonance wavelength shift before and after the sample loop. A representation of this more complex binding curve for the hybridization of a 10 nM complementary DNA solution is given in figure 3.20. This is the average shift of the active sensors on a single chip. It shows a complex transient behaviour: a combination of fluidic mixing, bulk refractive index changes, hybridization on the sensor surface and rinsing of non-specifically adsorbed molecules.

The sample loop arrives around 98 minutes into the experiment. The initial positive wavelength shift has to be attributed to an effect associated to the boundary between the hybridization buffer and the solution in the sample loop. The strong drop in signal that follows can be explained by the bulk index differ-

ence between the dilution in the sample loop and the pure hybridization buffer. While the sample loop flows over the sensors, hybridization on the chip surface takes place. Towards the end of the sample loop a rinsing of non-specifically adsorbed molecules explains the recorded negative wavelength shift. By comparing the slopes at 99 and 125 minutes into the experiment, we observe that the bulk index change or corresponding positive shift after the sample loop is less abrupt than the initial downshift. This is explained because the trailing end of the sample loop is pushed forward by pure hybridization buffer during the experiment and the boundary between both fluids is mixing through diffusion during the entire detection time. The leading edge of the sample loop reaches the sensors shortly after it comes in contact with the pure buffer and undergoes less mixing. The initial drop in signal is less deep than the final upshift because the fast hybridization at the start of the sample loop partly obscures the negative bulk shift. A net shift of 55 pm is recorded. This complex binding profile during the detection of complementary DNA shows the variety of reactions going on on the surface. It is a combination of bulk refractive index change, continuous hybridization and dissociation of sequences on the surface, while non-specific adsorption on the surface takes place or poorly bound molecules dissolve in solution again. At the same time the DNA strands in solution continuously interact with partially complementary sequence on other strands or form complex secondary structures by interaction with themselves. It is also unknown whether the large DNA strands on the surface form a dense blob or rather extend into the surrounding medium. We have to consider the possibility that the configuration of the bound molecules is not constant during the experiment. Especially after switching back to a standard PBS buffer, significant reorganizations on the surface can be expected. Another important limitation of reactions on the chip surface is the stationary fluidic boundary layer which forms a diffusion barrier with the fast moving liquid in the center of the channel.

Even though the precise dynamics of the measurement are not completely understood, a net shift corresponding to a certain concentration of DNA in the sample can be established by comparing the resonance wavelength of the sensors before and after the hybridization experiment. The net shifts recorded for three different concentrations down to 1 nM are depicted with a linear trend line in figure 3.21. This graph can serve as a calibration curve for the detection of the specific DNA sequence using the microring resonator sensors. The vertical line represents the 3σ noise level on the sensor wavelength as determined in section 3.2. Based on this calibration curve, the projected detection limit of the microring sensors would be about 200 pM. Further optimizations to improve this limit of detection are discussed in the next section. Unfortunately, the technique of recording net shifts significantly limits the possibility to detect very low concentrations because we are unable to perform the slope fitting

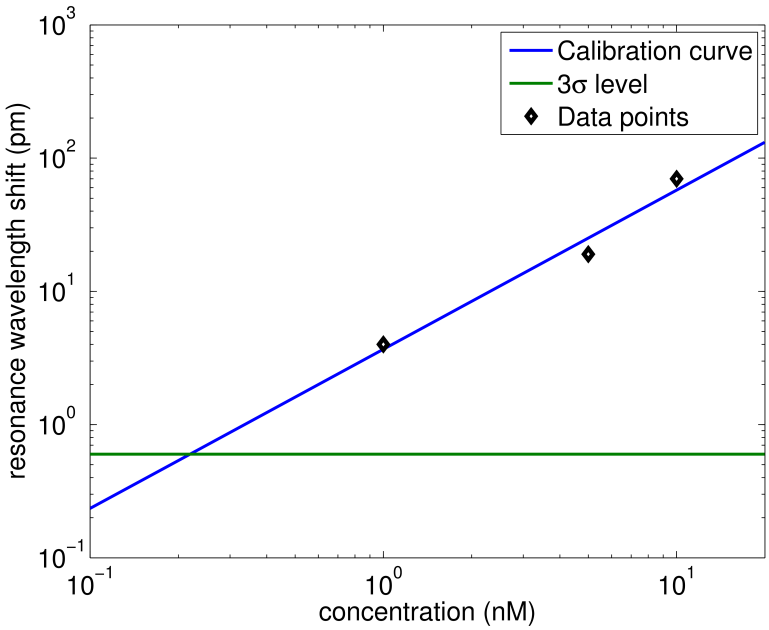

Figure 3.21: A calibration curve for the detection of complementary DNA using the microring resonator. The projected detection limit is 200 pM.

reported in [2]. Advanced applications like the detection of single-nucleotide polymorphism also rely on consistent and real-time monitoring of the transient behaviour [25]. Complex reaction dynamics prevent the extraction of the slope from the binding curve and improved fluidic systems and a better understanding of the chemical reactions on the surface are required to push the detection limit for complementary DNA of our system to lower values. Our experimental detection limit is close to the lowest concentration of 0.5 nM reported in literature for unamplified nucleic acid detection with microring resonators [26] and the theoretically extrapolated value is even lower. Continued improvements to the chemical surface modification and the measurement setup could further reduce the detection limit of our sensor platform, but order of magnitude improvements should not be expected for unamplified DNA detection. In the next section, additional optimizations that could push the detection limit to even lower values are discussed.

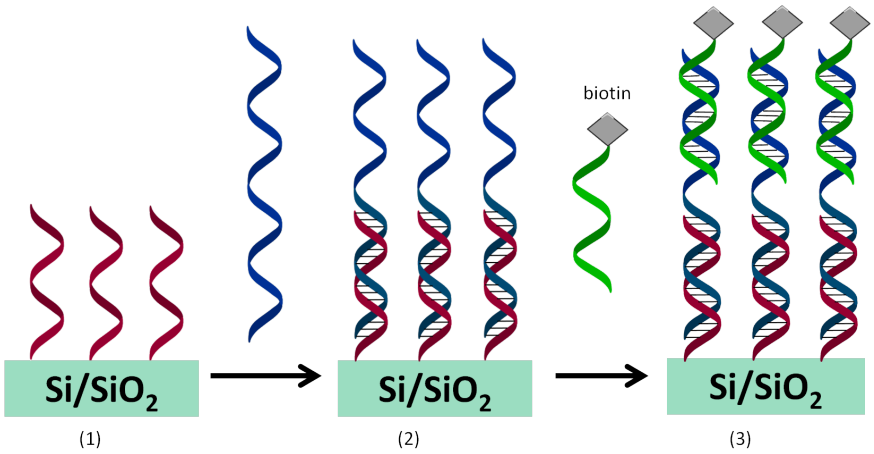

Figure 3.22: Schematic representation of the sandwich assay to introduce biotin to the sensor surface for increased avidin affinity.

3.4.1 Additional optimizations

In an attempt to amplify the signal after detection of the complementary strand, a sandwich assay can be performed. By introducing a second shorter DNA strand modified with a biotin tag, a specific affinity to streptavidin can be introduced to the sensor surface. This short biotinilated strand has a sequence complementary to the tail of the target DNA that extends into the solution, away from the surface. The procedure for biotinilation of the sensor surface using an aditional DNA strand is depicted in figure 3.22. In step (1), the surface is modified with the DNA capture probes. In step (2) the target DNA sequence hybridizes with the probes on the surface. During step (3) a short biotinilated DNA sequence hybridizes with the free end of the target strand and the affinity for streptavidin is introduced, but only when the target DNA is detected on the surface.

Preliminary experiments show little to no signal for the hybridization of the third DNA strand, which indicates a low efficiency for this step. It is likely that the hybridization is limited due to orientational problems with the strands in the vicinity of the chip surface. Experiments with streptavidin show a positive shift even when no biotin is present on the sensors. This indicates an important contribution of non-specific interactions on the sensor surface. This non-specific adsorption on the surface can also be recognized by the apparent rins-

ing in the recorded binding curve of figure 3.20. To eliminate this non-specific interaction, the incorporation of PEG spacers has proven successful in different applications [27] and this is currently under investigation.

The molecular weight of streptavidin is about 60 kDa [28], much higher than the average nucleotide weight of single stranded DNA (303.7 Da) [29]. By introducing large streptavidin molecules, the signal due to the target DNA strand could be amplified. However, because of the very long length of the target strand (84 bases), a signal amplification by only a factor 2 can be obtained assuming 100% efficiency for the hybridization of the biotinilated strand and the biotin-avidin interaction. Such a high effiency is very unlikely and the amplification factor is low. A better approach would be to introduce streptavidin-coated beads to exploit the single-bead detection demonstrated in section 3.2. This does however also require reduced non-specific interactions and possibly an improvement of the microfluidic system to avoid the sinking of the heavy beads to the bottom of the channel. Signal amplification using DNA:RNA duplex antibodies has been reported to improve the limit for detection of complementary oligonucleotides down to 10 pM [30].

3.5 Conclusions

To summarize, we have developed measurement software and implemented improvements to the optical setup and the sensor chip that result in an optical detection limit of 0.6 pm, determined by the noise of the optical system. Using streptavidin-coated magnetic beads, single-bead sensitivity of the optical sensor is established. In collaboration with the Polymer Chemistry and Biomaterials Group, the chemical functionalization of the chip surface to detect complementary DNA sequences is developed. Measurements on the optical setup using the DNA detection array have resulted in the detection of different concentrations of target DNA sequences down to 1 nM and an experimental detection limit of 200 pM is projected. To improve the performance of the microring DNA sensors, we propose the development of an amplification scheme using biotinilated DNA sequences and streptavidin-coated beads. Improved microfluidic systems can be an important step towards simplified reaction dynamics, which could further reduce the detection limit by enabling slope detection techniques. Finally, the elimination of the non-specific signal of the sensors by blocking the surface with PEG or BSA is a key requirement for the continued development of the microring sensors.

References

[1] K. D. Vos. *Label-Free Silicon Photonics Biosensor Platform with Microring Resonators*. PhD thesis, Ghent University, 2010.

[2] M. Iqbal, M. A. Gleeson, B. Spaugh, F. Tybor, W. G. Gunn, M. Hochberg, T. Baehr-Jones, R. C. Bailey, and L. C. Gunn. *Label-Free Biosensor Arrays Based on Silicon Ring Resonators and High-Speed Optical Scanning Instrumentation*. IEEE Journal of Selected Topics in Quantum Electronics, 16(3):654–661, 2010.

[3] A. Densmore, D. Xu, N. A. Sabourin, H. Mcintosh, P. Cheben, J. H. Schmid, R. Ma, M. Vachon, A. Delâge, W. Sinclair, J. Lapointe, Y. Li, G. Lopinski, B. Lamontagne, and S. Janz. *A Fully Integrated Silicon Photonic Wire Sensor Array Chip and Reader Instrument*. Optics Express, pages 350–352, 2011.

[4] https://www.python.org/. 2014.

[5] G. Roelkens, D. Taillaert, F. Van Laere, D. Vermeulen, J. Schrauwen, S. Scheerlinck, T. Claes, W. Bogaerts, P. Dumon, S. Selvaraja, D. Van Thourhout, and R. Baets. *Interfacing optical fibers and high refractive index contrast waveguide circuits using diffractive grating couplers*. In Broquin, JE and Greiner, CM, editor, Integrated Optics: Devices, Materials, and Technologies XIII, volume 7218 of *Proceedings of SPIE-The International Society for Optical Engineering*. SPIE, 2009. Conference on Integrated Optics - Devices, Materials, and Technologies XIII, San Jose, CA, Jan 26-28, 2009.

[6] T. D. C. Company, *http://www.dow.com/cyclotene/prod/402235.htm*. May 2013.

[7] T. Claes. *Advanced Silicon Photonic Ring Resonator Label-free Biosensors*. PhD thesis, Ghent University, 2012.

[8] K. De Vos, J. Girones, T. Claes, Y. De Koninck, S. Popelka, E. Schacht, R. Baets, and P. Bienstman. *Multiplexed Antibody Detection With an Array of Silicon-on-Insulator Microring Resonators*. IEEE Photonics Journal, 1(4):225–235, October 2009.

[9] A. E. Cetin, A. F. Coskun, B. C. Galarreta, M. Huang, D. Herman, A. Ozcan, and H. Altug. *Handheld high-throughput plasmonic biosensor using computational on-chip imaging*. Light: Science & Applications, 3, January 2014.

[10] http://www.photond.com/files/brochures/fimmwave_brochure.pdf. 2014.

[11] T. Claes, J. Molera, K. De Vos, E. Schacht, R. Baets, and P. Bienstman. *Label-Free Biosensing With a Slot-Waveguide-Based Ring Resonator in Silicon on Insulator*. IEEE Photonics Journal, 1(3):197–204, September 2009.

[12] T. Yoshie, L. Tang, and S.-Y. Su. *Optical Microcavity: Sensing down to Single Molecules and Atoms.* Sensors, 11(2):1972–1991, 2011.

[13] J. Hu, X. Sun, A. Agarwal, and L. C. Kimerling. *Design guidelines for optical resonator biochemical sensors.* J. Opt. Soc. Am. B, 26(5):1032–1041, 2009.

[14] http://www.ademtech.com/images/masterbeads%20streptavidin%200315%20v1.3.pdf. 2014.

[15] http://www.solulink.com/products/ptm/S-1002-SHyNic.pdf. 2014.

[16] A. J. Qavi and R. C. Bailey. *Multiplexed detection and label-free quantitation of microRNAs using arrays of silicon photonic microring resonators.* Angewandte Chemie (International ed. in English), 49(27):4608–11, June 2010.

[17] http://www.solulink.com/products/ptm/HL-1002-HyNicSilane.pdf. 2014.

[18] A. U. Alam, M. M. R. Howlader, and M. J. Deen. *Oxygen Plasma and Humidity Dependent Surface Analysis of Silicon, Silicon Dioxide and Glass for Direct Wafer Bonding.* ECS Journal of Solid State Science and Technology, 2(12):P515–P523, 2013.

[19] B. W. Biggs, H. K. Hunt, and A. M. Armani. *Selective patterning of Si-based biosensor surfaces using isotropic silicon etchants.* Journal of Colloid and Interface Science, 369(1):477 – 481, 2012.

[20] J. Diao, D. Ren, J. R. Engstrom, and K. H. Lee. *A surface modification strategy on silicon nitride for developing biosensors.* Analytical Biochemistry, 343(2):322 – 328, 2005.

[21] J.-Y. Byeon, F. T. Limpoco, and R. C. Bailey. *Efficient Bioconjugation of Protein Capture Agents to Biosensor Surfaces Using Aniline-Catalyzed Hydrazone Ligation.* Langmuir, 26(19):15430–15435, 2010.

[22] I. Barisic, S. Schoenthaler, R. Ke, M. Nilsson, C. Noehammer, and H. Wiesinger-Mayr. *Multiplex detection of antibiotic resistance genes using padlock probes.* Diagnostic Microbiology and Infectious Disease, 77(2):118–125, October 2013.

[23] R. D. Blake and S. G. Delcourt. *Thermodynamic Effects of Formamide on DNA Stability.* Nucleic Acids Research, 24(11):2095–2103, 1996.

[24] http://www.mcb.uct.ac.za/Manual/hybridn.htm. 1998.

[25] A. J. Qavi, T. M. Mysz, and R. C. Bailey. *Isothermal Discrimination of Single-Nucleotide Polymorphisms via Real-Time Kinetic Desorption and Label-Free Detection of DNA Using Silicon Photonic Microring Resonator Arrays.* Analytical chemistry, 83(17):6827–33, September 2011.

[26] O. Scheler, J. T. Kindt, A. J. Qavi, L. Kaplinski, B. Glynn, T. Barry, A. Kurg, and R. C. Bailey. *Label-free, multiplexed detection of bacterial tmRNA using silicon photonic microring resonators.* Biosensors and Bioelectronics, 36(1):56 – 61, 2012.

[27] K. De Vos, J. Girones, S. Popelka, E. Schacht, R. Baets, and P. Bienstman. *SOI optical microring resonator with poly(ethylene glycol) polymer brush for label-free biosensor applications.* Biosensors & Bioelectronics, 24(8):2528–2533, April 15 2009.

[28] http://www.piercenet.com/method/avidin-biotin-interaction. 2014.

[29] http://www.lifetechnologies.com/be/en/home/references/ambion-tech-support/rna-tools-and-calculators/dna-and-rna-molecular-weights-and-conversions.html. 2014.

[30] A. J. Qavi, J. T. Kindt, M. a. Gleeson, and R. C. Bailey. *Anti-DNA:RNA Antibodies and Silicon Photonic Microring Resonators: Increased Sensitivity for Multiplexed microRNA Detection.* Analytical chemistry, 83(15):5949–56, August 2011.

4

Anti-transmission gratings

4.1 Introduction

Low-noise performance combined with ease of use and robustness against external disturbances is a mandatory requirement for many integrated applications. This is especially true for devices that are extremely sensitive to interference noise caused by parasitic paths. While this thesis focuses on applications for Silicon-on-insulator (SOI) photonic biosensors, the results discussed in this chapter are applicable to a variety of integrated applications, including optical coherence tomography [1] and on-chip laser Doppler vibrometry [2]. Rather than coupling light into the microchip waveguides using traditional fiber coupling relying on vertically coupling gratings [3] which require delicate alignment fibers and micrometer accuracy, one can make use of a free-space setup with a broad, collimated laser beam to illuminate the chip surface. This improves robustness against vibrations and enables simultaneous excitation of a compact grating coupler array for better multiplexing possibilities [4]. However, various parasitic reflections from the SOI degrade the performance of the device. Improved grating couplers for photonic applications [5, 6] and reflectionless multimode interferometers [7] have been suggested, but parasitic transmission paths through the chip substrate still form an important limitation of the device performance by inducing interferences in the coupled light. Here, we develop an integrated anti-transmission grating to alleviate this issue. Section 4.2 discusses

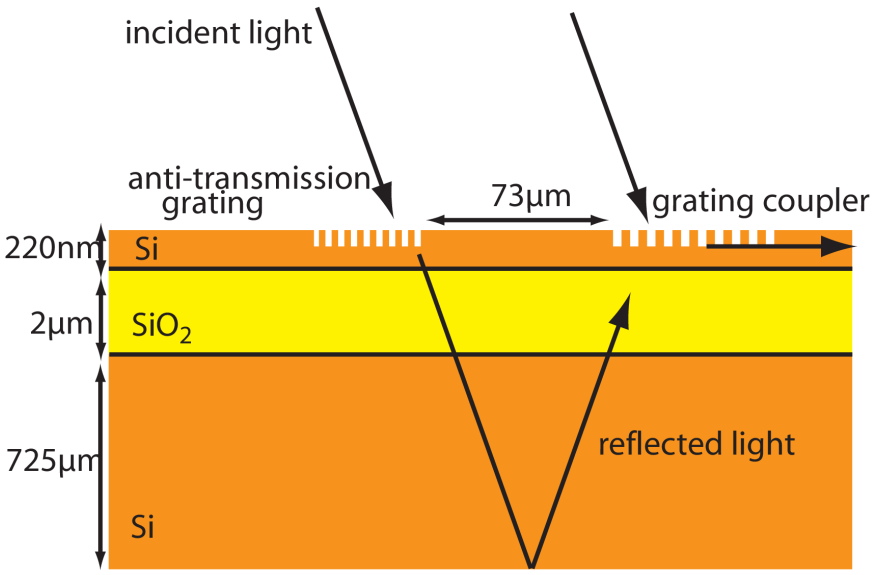

Figure 4.1: Schematic representation of light incident on chip surface. Light coupling to the waveguide through the grating coupler after reflection on the substrate induces an interference pattern. An anti-transmission grating can be implemented to block this parasitic light path.

the origin of the coupling issues. In section 4.3, the theoretical and simulated performance of the suggested anti-transmission gratings is analyzed. Finally, in section 4.4 the experimental reduction of the interference pattern is demonstrated.

4.2 Surface Grating Structures

Figure 4.1 shows a schematic representation of the incident light and the layered microchip surface. The chip is processed from a Smart-Cut SOI wafer [8] and consists of a thick silicon substrate, a 2 μm thick oxide buffer layer and a 220 nm silicon top layer. It is in this top silicon layer that integrated photonic structures such as microring sensors are patterned. The chip surface is illuminated by a collimated light beam with an incidence angle of 10°. Several waveguides can be excited simultaneously by a single input beam. The fraction of the light incident on a grating coupler [9] in a waveguide couples directly into

the photonic wire waveguide with an efficiency up to 30% and an angle tolerance below 1 dB per 2°. However, light incident on the chip surface in the area in front of this grating will be transmitted through the silicon-air interface. This beam propagates through the chip substrate and reflects at the back surface. As the longitudinal component of the wavevector is conserved upon refraction, the Bragg condition of equation 4.1 for the grating coupler is also met by the reflected light beam:

$$\beta = k_{in}\sin(\theta) + K \tag{4.1}$$

In (4.1), $\beta = \frac{2\pi}{\lambda} n_{eff}$ is the propagation constant of the guided mode with effective index n_{eff} and $K = \frac{2\pi}{\Lambda}$, with Λ the period of the grating. $k_{in} = \frac{2\pi}{\lambda}$ is the wavevector and θ is the angle between the incoming light and the surface normal, $\theta = 10°$ in this case. The reflected light will then couple efficiently through the buried oxide layer to the waveguide. The round trip through the chip substrate introduces a significant path length difference and affects the phase of the reflected light. The phase difference between the directly coupled and the reflected light generates a strong interference pattern in the input light. The effect on the transmitted power in the microchip for the application of microring resonator sensors is demonstrated in figure 4.2, where it can be seen that the interference completely destroys the resonance line shape. The microring resonator used in this experiment consists of a 450 nm by 220 nm silicon wire waveguide. With a total round-trip length of 140 μm and directional coupler spacing of 250 nm, this results in a resonance linewidth of 200 pm and a free spectral range of 3.6 nm in water.

The interference pattern has a period of 450 pm and modulates the microring drop signals to an extent that the peak intensity is greatly suppressed and the sensor signal is effectively destroyed. Experimental characterization of the chip thickness confirms that reflections of the back surface generate an interference pattern with the observed period. Even in the case that the microring signal is not completely destroyed, the interference pattern can still severely degrade sensing operation. During the detection of a biomolecule, the change in refractive index at the surface of the biosensor induces a shift in wavelength visible in the sensor signal. However, the strong modulation signal does not shift. This gives rise to highly undesirable features in an experimentally recorded binding curve and could lead to false detection events. Therefore, we suggest an integrated solution that can be implemented with the same lithographic procedure used for the definition of the transducer and thus does not require any additional processing steps. We implement anti-transmission grating structures at the chip-air interface in the position that leads to the parasitic light path, as shown in figure 4.1. This limits the transmission efficiency and reduces the intensity of the reflected light. Other techniques, like local metal deposition to absorb the parasitic light or surface roughening yield similar results, but this

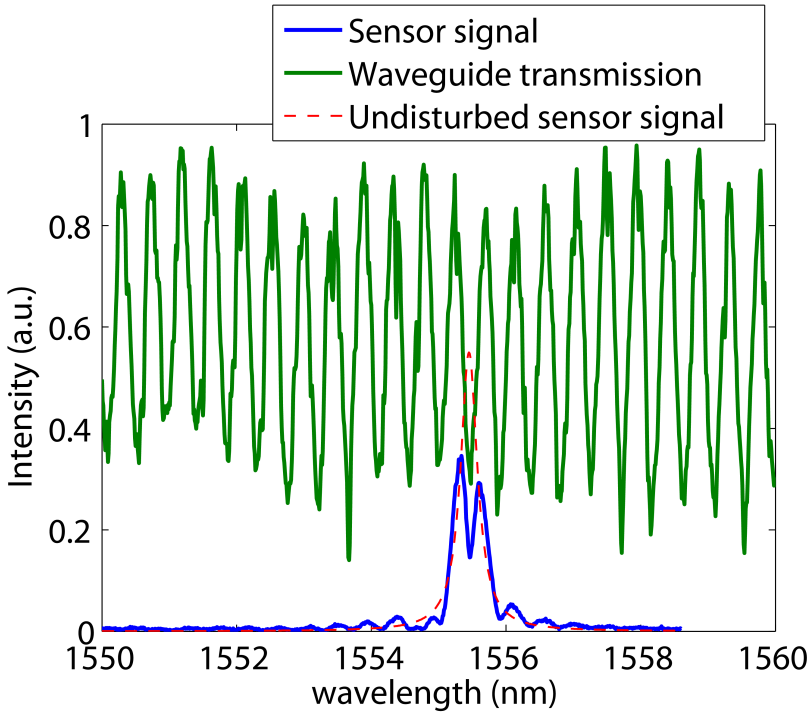

Figure 4.2: Measured transmission signals disturbed by interference due to parasitic reflections. The dashed line shows the calculated undisturbed sensor signal.

requires additional costly and time-consuming processing steps. We will show that our approach efficiently reduces the parasitic reflected signals and their corresponding interference pattern, without introducing additional processing steps.

4.3 Theory and simulations

In this section, we will examine the characteristics of the grating structures that are implemented as anti-transmission gratings. Both backward-coupling gratings (BCG) and high-contrast gratings (HCG) are investigated for this purpose. First, a theoretical description of the gratings is given. Simulations for these two different implementations of the anti-transmission grating of figure 4.1 are performed using two-dimensional finite-difference time-domain (2D-FDTD) methods and Rigorous Coupled Wave Analysis (RCWA). For backward-coupling gratings, a theoretical efficiency is obtained by discussing experimen-

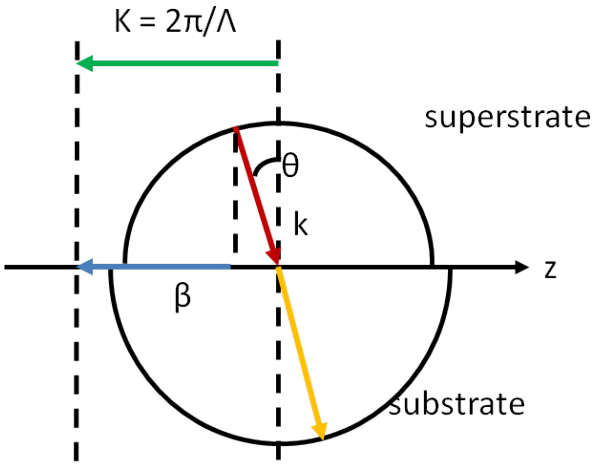

Figure 4.3: Schematic representation of the Bragg condition for a grating coupling backward to the waveguide mode.

tally recorded transmission characteristics of the individual gratings.

4.3.1 Backward-coupling grating

A first approach uses a backward-coupling grating to diffract light to the waveguide in the opposite direction. This light will then propagate away from the grating coupler rather than refracting to the substrate region. Using a taper structure, the backward propagating light is dissipated in the silicon slab region that covers the chip surface. The grating is realized by etching 70 nm deep lines in the 220 nm thick waveguide layer, with a duty cycle of 50%.

The Bragg condition of equation 4.2 is schematically represented in figure 4.3. It is used to derive a grating period of 540 nm for a BCG for light with a wavelength of 1550 nm and an incidence angle of 10°.

$$-\beta = k_{in}\sin(\theta) - K \tag{4.2}$$

In equation 4.2, $\beta = \frac{2\pi}{\lambda} n_{eff}$ is the propagation constant of the guided mode with effective index n_{eff} and $K = \frac{2\pi}{\Lambda}$, with Λ the period of the grating. $k_{in} = \frac{2\pi}{\lambda}$ is the wavevector and θ is the angle between the incoming light and the surface normal, $\theta = 10°$ in this case.

We can estimate the theoretical performance of the BCG as anti-transmission grating by investigating the coupling efficiency of an individual BCG. Figure 4.4 shows the recorded transmission to a single-mode optical waveguide of the

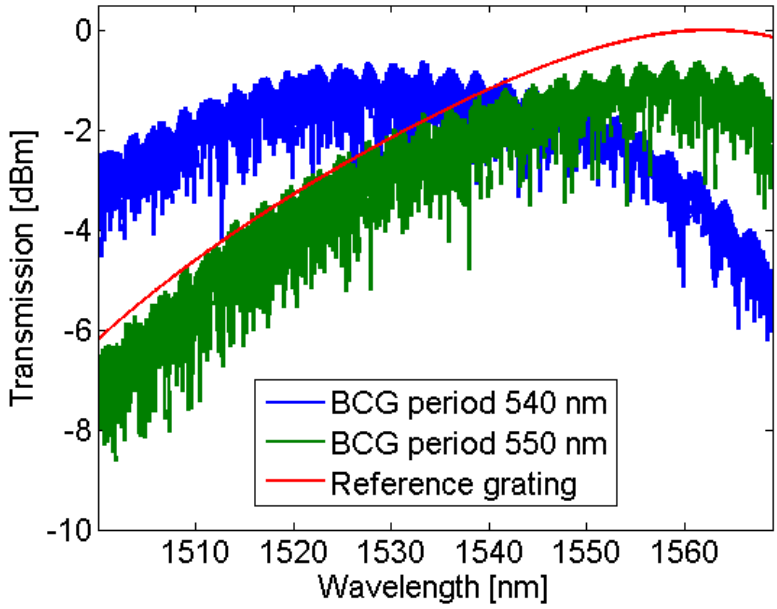

Figure 4.4: Experimentally recorded transmission spectra for backward-coupling gratings.

backward-coupling grating compared to the transmission spectrum of the standard forward-coupling tapered grating coupler from [10]. The spectra are recorded from the same optical chip by an Agilent 81980A tunable laser and an Agilent 81635A optical powermeter. For the reference spectrum, a 4th-order polynomial is fit to the transmission to eliminate noise fluctuations. In theory, a second-order polynomial adequately describes the grating transmission. However in practice, small alignment differences in the in- and output optical fiber result in a slightly different response for the in-and output grating couplers. This makes a 4th-order polynomial better suited to describe the transmission from a waveguide with two grating couplers. By dividing the response by two, we obtain the average response of the two grating couplers, which we use as a reference. The zero of the transmission scale is set to the maximum of the reference spectrum. Both backward-coupling gratings introduce an extra loss of only 0.6 dB with transmission maxima at 1533 nm and 1559 nm for a period of 540 nm and 550 nm, respectively. Even though these results are obtained for fiber-to-grating coupling, they hold approximately for a plane wave incident on the surface, since only -1 dB can be attributed to mode mismatch losses [11].

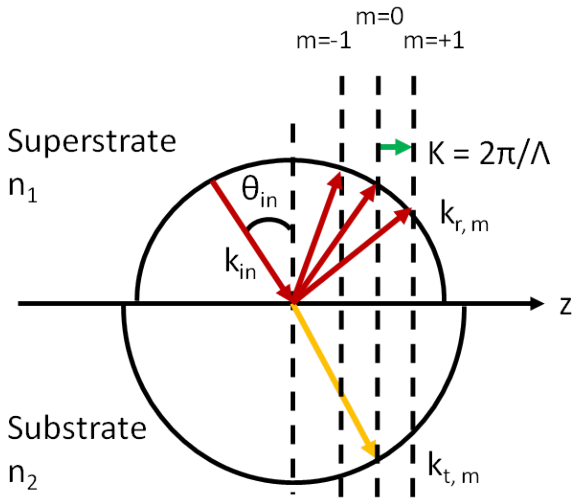

Figure 4.5: Schematic representation of the Bragg condition for diffraction by a grating on an interface between two media.

From [10], we know that the experimental efficiency of the reference grating is about −5 dB. Compared to the situation without any anti-transmission structure, this coupling efficiency indicates an additional fraction of about 30% of the input power is unavailable for transmission to the substrate because it is coupled to the waveguide by the backward-coupling grating.

4.3.2 High-contrast grating

Alternatively, we have also investigated the implementation of a high-contrast grating. Instead of guiding the light to the slab region, the HCG prevents light from reaching the grating coupler by maximizing the zero-order reflection. This type of grating has been primarily investigated for the applications in vertical-cavity surface-emitting lasers (VCSELs) because of its high reflection over wide wavelength bands and therefore relatively large fabrication tolerances for lasing devices [12, 13]. The high contrast is obtained by etching 220 nm deep lines through the full height of the waveguide layer. Theoretically, maximum zero-order reflection can be obtained by creating a grating without higher order diffraction. This can be understood from figure 4.5. An incident wave with wavevector k_{in} and angle θ_{in} is diffracted by a grating on an interface between two media with refractive indices n_1 and n_2 to several diffraction orders $k_{r,m}$ and $k_{t,m}$ for reflection and transmission, respectively. These wavevectors propagate with an angle $\theta_{r,m}$ and $\theta_{t,m}$, respectively. The m-

th order diffraction is determined by the Bragg condition of equation 4.3, which expresses conservation of the longitudinal component of the wavevector.

$$k_m \sin(\theta_m) = k_{in} \sin(\theta_{in}) + mK \tag{4.3}$$

In equation 4.3, $K = \frac{2\pi}{\Lambda}$ is the reciprocal grating vector and m an integer indicating the diffraction order. For a diffracted beam in reflection:

$$k_m \sin(\theta_m) = n_1 \frac{2\pi}{\lambda} \sin(\theta_{r,m}) + mK \tag{4.4}$$

while for the transmitted diffraction orders:

$$k_m \sin(\theta_m) = n_2 \frac{2\pi}{\lambda} \sin(\theta_{t,m}) + mK \tag{4.5}$$

In this case, $n_1 = 1$ for air and $n_2 = 1.45$ for the buried oxide layer of the silicon chip. For an angle of incidence $\theta_{in} = 10°$, any real solutions in transmission for $|m| > 0$ can be eliminated by reducing the grating period Λ. Because $\left|\sin(\theta_{t,m})\right| > 1$ as soon as

$$\left|\sin(\theta_{in}) \pm \frac{\lambda}{\Lambda}\right| > n_2 \tag{4.6}$$

all higher order transmitted light becomes evanescent. Then:

$$\Lambda < \frac{\lambda}{\sin(\theta_{in}) + n_2} \tag{4.7}$$

or:

$$\Lambda < 957\,\text{nm} \tag{4.8}$$

The condition to eliminate higher-order diffraction for the reflected light as well is then automatically observed, because it is less stringent than for the transmitted light. This value of Λ will serve as a reference value for the simulations to study the behaviour of the high-contrast grating.

4.3.3 Simulation results

First, 2D-FDTD is used to simulate the transmission to the substrate. The backward-coupling grating in the simulation consists of 70 nm deep lines etched in the 220 nm thick waveguide layer, with a duty cycle of 50% and a period of 540 nm. The high-contrast grating with 220 nm deep lines has a fill factor of 50% and a period of 950 nm, which corresponds to the condition for zero-order diffraction established before. For the reference simulation, we consider the 220 nm thick silicon waveguide layer that covers the buried oxide layer on the chip. Scanning Electron Microscope (SEM) pictures of the cross section of both gratings with schematic indication of the desired light propagation are shown in figure 4.6a.

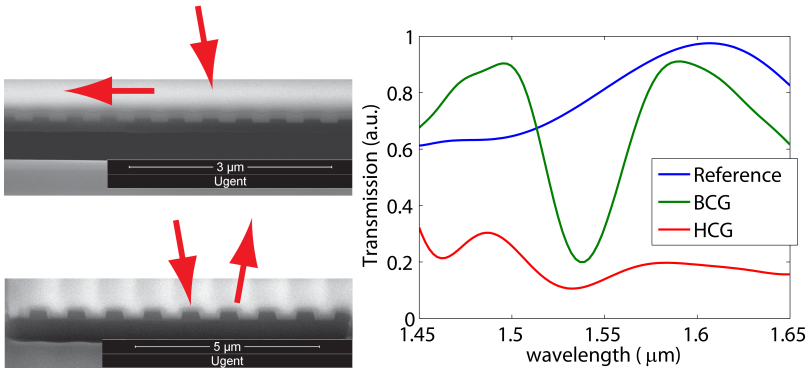

(a) **(b)**

Figure 4.6: (a) SEM pictures of the cross section of backward (top) and high-contrast grating (bottom) with schematic representation of light propagation. (b) Simulated transmission to the substrate for different grating implementations. Introduction of the surface gratings significantly reduces the transmitted power.

Figure 4.6b shows the simulated transmission to the substrate. These simulations clearly show a significant reduction of the transmitted power after implementing the gratings on the chip surface. A fundamental difference between both approaches also becomes apparent. The BCG is only efficient in a narrow band around the design wavelength of 1550 nm, whereas the HCG can introduce high reflection over a relatively wide wavelength band. For the BCG design we can benefit from previous work that has been done in optimizing the classical grating couplers [11, 14, 15]. For the HCG on the other hand, we can rely on more appropriate simulation methods to investigate the influence of various parameters on the grating efficiency.

As described in [16], other simulation methods than FDTD are better suited to simulate grating design. In this work, we will use the technique of RCWA. We make use of the publicly available RCWA tool RicWaA [17], which is based on the methods described in [18–20]. In this paragraph, we investigate the influence of design parameters like operating wavelength, grating period, grating thickness and fill factor on the efficiency of the HCG as an anti-transmission grating. These parameters are indicated on the grating schematic of figure 4.7. As the grating thickness is determined by the silicon waveguide layer, it cannot be influenced at the design stage. It is however, subject to variations occurring during fabrication. That is why this parameter is included in this analysis. For the theoretical grating thickness of 220 nm the lowest transmission at an operating wavelength of 1550 nm is obtained for a grating period of 950 nm and a

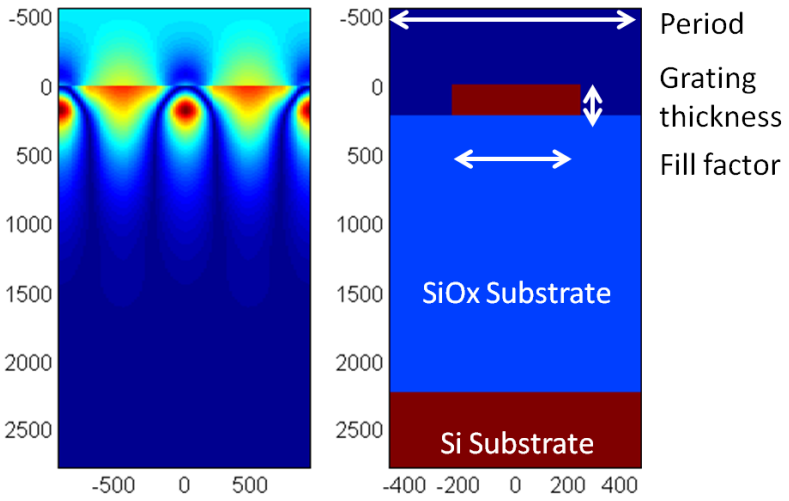

Figure 4.7: The simulated field distribution in a period of the high-contrast grating (right) and a schematic representation of the same region with simulation parameters (left).

duty cycle or fill factor of 50% and amounts to 7%. For the HCG with these parameters, the resulting field distribution in one period of the grating is given in figure 4.7.

In general, when considering normally-incident light compared to an incidence angle of 10°, the effect of changing the parameters is more pronounced in the latter. We can also identify some trends. Within the region of interest, changing the operating wavelength and the grating thickness has relatively little effect on the transmission to the substrate. Transmission remains low (< 0.1) over the majority of the parameter space. The wavelength dependency of the grating becomes significant only for a grating thickness larger than 230 nm, but transmission still remains below 35%. This is depicted in figure 4.8.

On the other hand, parameters that have a very strong effect on the grating efficiency are the grating period and the fill factor or duty cycle (unetched fraction) of the grating. This is demonstrated in figure 4.9, where the area of low transmission (< 0.1) is very small compared to the parameter space. But what is even worse, by changing the period, the grating moves from a low transmission regime to a high transmission regime $> 90\%$, which is contrary to what we want to achieve. A change in duty cycle can also result in a high-contrast grating operating in a high transmission regime, especially for duty cycles larger than 50%.

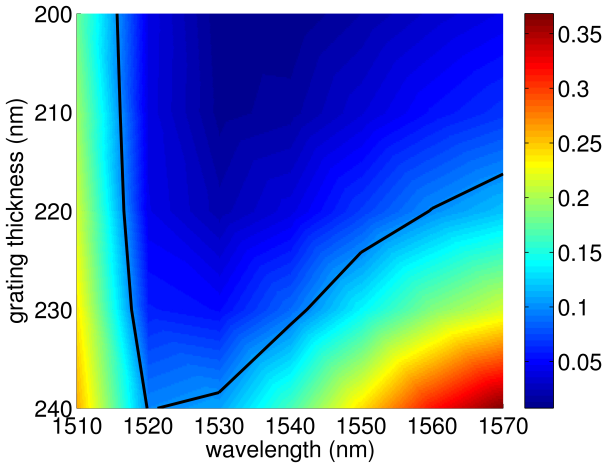

Figure 4.8: Simulated transmission to substrate for varying operating wavelength and grating thickness for a HCG with 950 nm period and a duty cycle of 50%. The 0.1 contour is also given. The incident light has an angle of 10°.

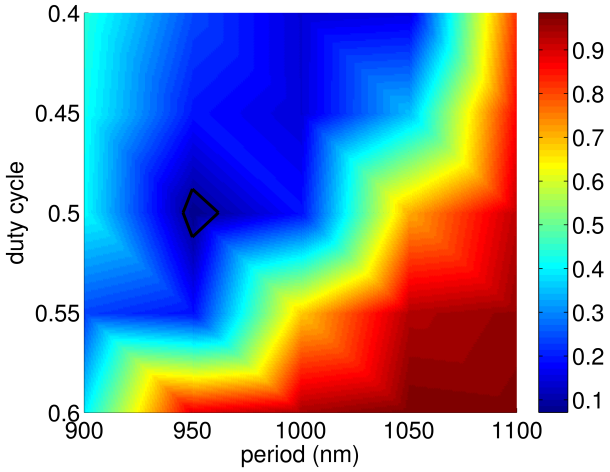

Figure 4.9: Simulated transmission to substrate for varying grating period and duty cycle for a HCG with 220 nm thickness at a wavelength of 1550 nm. The 0.1 contour is also given. The incident light has an angle of 10°.

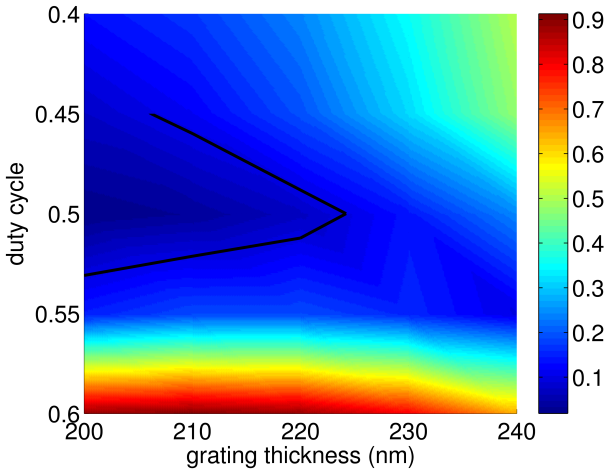

Figure 4.10: Simulated transmission to substrate for varying grating thickness and duty cycle for a HCG with 950 nm period at a wavelength of 1550 nm. The 0.1 contour is also given. The incident light has an angle of 10°.

This last effect is especially important when considering fabricated devices, as over- or underetching of the grating will immediately affect the duty cycle. Large deviations from the design period are not expected during fabrication, but another parameter that suffers significantly from fabrication variations is the thickness of the silicon waveguide layer, which determines the grating thickness. To visualize the effect of the parameters that are expected to suffer most from fabrication deviations, we have included the influence of duty cycle and grating thickness in figure 4.10. This figure again confirmes that a change in duty cycle results in the most adverse effects. However, for small duty cycles, a change in grating thickness can also cause a significant change in transmission from 0.1 to 0.5.

4.4 Experimental Results

Based on the simulation results, a design combining the grating couplers and the anti-transmission gratings has been fabricated in a complementary metal-oxide-semiconductor (CMOS) pilot line at imec. Scanning Electron Micrographs (SEM) of the fabricated gratings are shown in figure 4.11.

For a chip thickness of 725 μm, the location of the gratings on the surface is calculated to be 73 μm in front of the grating coupler, as depicted in figure 4.1. In

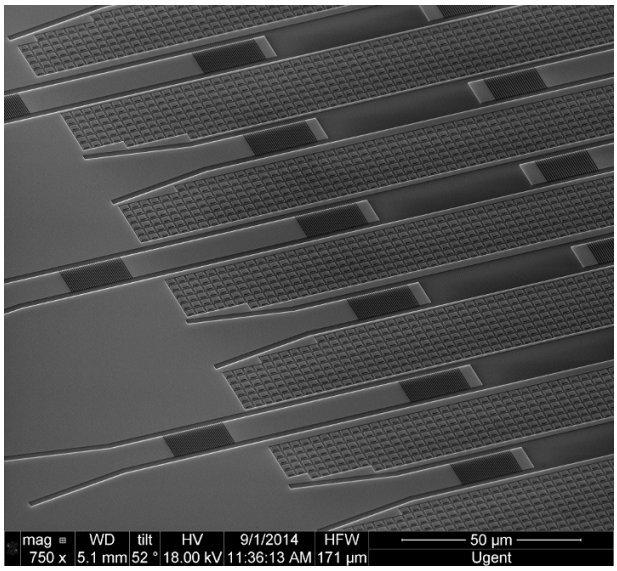

(a)

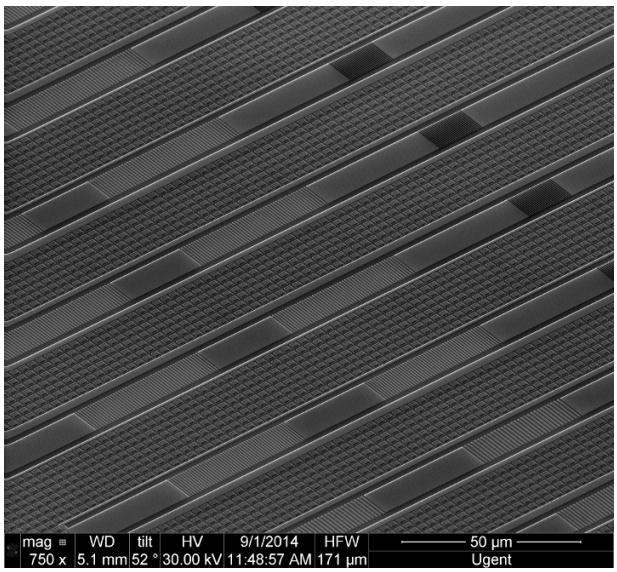

(b)

Figure 4.11: SEM pictures showing the combination of input coupling gratings with anti-transmission gratings for (a) BCG and (b) HCG implementations.

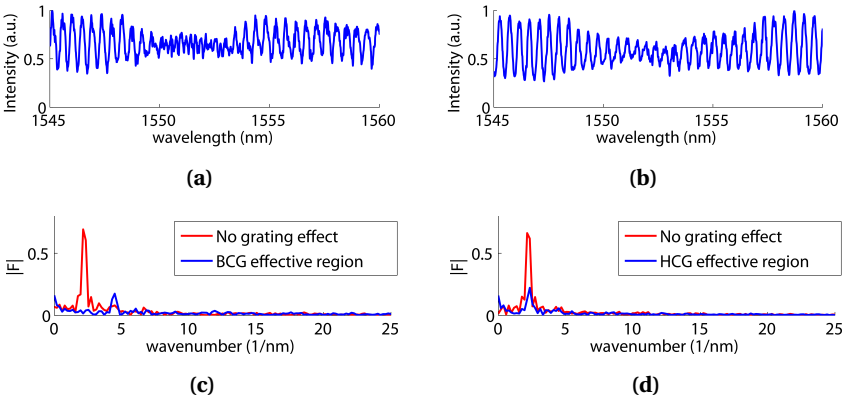

Figure 4.12: Transmission spectra of grating coupler combined with BCG (a) and HCG (b). The grating effective region is clearly visible in both cases. (c) and (d) show the comparison of the Fourier spectra in and outside the grating region of effect for BCG and HCG, respectively. The dominant Fourier components are significantly reduced in both cases.

this position, the anti-transmission gratings will prevent the incident light from being transmitted to the back of the substrate and reflected up to the grating coupler. This eliminates the parasitic interferences. The chip is mounted on a measurement chuck for characterization. A collimated laser beam illuminates the input grating couplers and the surrounding chip surface. The light incident on the surface of the chip can be approximated by a plane wave because the spot size of the laser beam is much larger than the region of interest surrounding the gratings. A Santec TSL-510C tunable laser is swept at 5 nm/s over a 20 nm range with a wavelength resolution of 10 pm. A Xenics Xeva-1.7-320 infrared camera is used to record the output spectra with a frame rate of 500 Hz. This is the same measurement setup we use for the bio-experiments described in chapter 3. In this section, we will discuss the results obtained for the implementation of a BCG and a HCG as anti-transmission gratings.

4.4.1 First generation

In a first generation of the design, the anti-transmission gratings are placed in the position that leads to the parasitic pathway through the substrate, 73 μm in front of the waveguide grating coupler. The transmission spectra recorded on the optical setup are shown in figure 4.12. Figure 4.12a shows the recorded spectrum for a grating coupler combined with a 35-period BCG with a grating period of 530 nm. Around 1551.5 nm, a region with reduced interference effects

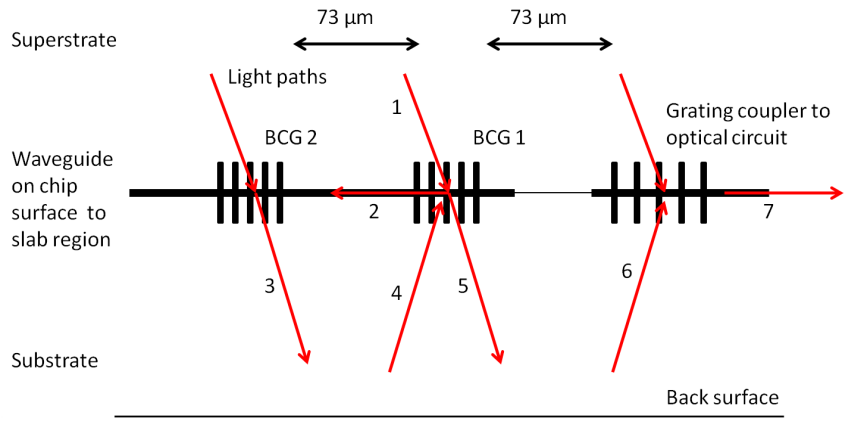

Figure 4.13: Implementation of a second BCG leads to a deterioration of the signals because diffracted light circulates between both gratings.

is clearly visible. This suppression region corresponds reasonably well to the grating wavelength targeted during design. It should be noted this sample is processed in a different process run than the sample which contained the BCGs discussed in section 4.3.1. This can explain why the BCG appears to operate at a different wavelength. The data are analyzed by Fourier transforming the spectrum. This provides more insight into the origin of the oscillations. Figure 4.12c compares the Fourier spectrum of a 3 nm region around 1551.5 nm to that of a 3 nm region with maximum interference strength. This shows the dominant component corresponding to oscillations with a 450 pm period is successfully suppressed in the 1551.5 nm region. The suppression region shows the occurrence of another Fourier component corresponding to 220 pm period oscillations, but with significantly lower intensity. This feature is also present in the maximum interference region, but it is slightly obscured due to the noisy nature of the signals. The second component can be attributed to second-order reflections of the chip substrate. Indeed, light incident on the chip surface 146 μm in front of the grating coupler will make two round trips through the substrate, reflecting twice off the bottom surface and thus arriving at the grating coupler with lower intensity and giving rise to less pronounced interference effects. Figures 4.12b and 4.12d show the results for a 30-period HCG implemented 73 μm in front of the grating coupler. The period of the HCG is 1050 nm. Here, the 450 pm period remains the dominant oscillation, while its strength is significantly reduced. A small component at 220 pm can barely be discerned from noise.

4.4.2 Second generation

In view of the second-order reflections that still give rise to degradation of the signals in the suppression region of the first grating, we have designed a second-generation optical chip. In this design, the anti-transmission gratings are repeated in the location that leads to the second-order transmission path, 146 μm in front of the waveguide grating coupler. Unfortunately, for the BCG, this approach does not result in a significant improvement of the transmission spectra compared to the first generation. This can be attributed to the effect of the combination of two backward-coupling gratings on the same waveguide, explained in figure 4.13. When the light coupled by the first BCG travels backward through the waveguide, it encounters the second BCG on its way to the slab region. On this second grating, the light diffracts rather than continuing on to the slab region. Because the grating period matches the Bragg condition, the diffraction angle equals the angle of the refracted light in the substrate. This means the light from the second BCG will be sent back to the first BCG, because the second grating is placed exactly in the position that constitutes the parasitic light path. This leads to the complex interference pattern that is visible in figure 4.14a, with two equally strong oscillating contributions in the Fourier spectrum 4.14c. This spectrum corresponds to the transmission of a grating coupler combined with two 35-period BCGs with a grating period of 550 nm. Because the second-generation BCG does not provide the required performance, it is not discussed in the following paragraphs.

For the second-generation high-contrast grating on the other hand, repeating the HCG in the location that leads to the second-order parasitic path leads to a significant improvement of the signal. The difference here is that the HCG maximizes the zero-order reflection, and the light that is not transmitted is lost in free space. For the combination of a grating coupler with two 50-period HCGs with a grating period of 1050 nm, the transmission spectrum is shown in figure 4.14b. A wide region of reduced oscillations can be seen in the spectrum. The Fourier spectrum for the grating effective region is obtained by transforming a 4 nm wide window around the maximum efficiency wavelength of 1565 nm and is given in figure 4.14d. When comparing this Fourier spectrum to that outside the grating effective region, it is clear that both Fourier components are almost entirely suppressed.

4.4.3 Analysis of experimental results

For a detailed analysis of the results, we have to introduce a model that describes the interference pattern. The intensity pattern in the signal waveguide can be modeled as a simple two-beam interference signal given by equation 4.9:

$$I = I_1 + I_2 + 2\sqrt{I_1 I_2}\cos(\Delta\phi) \tag{4.9}$$

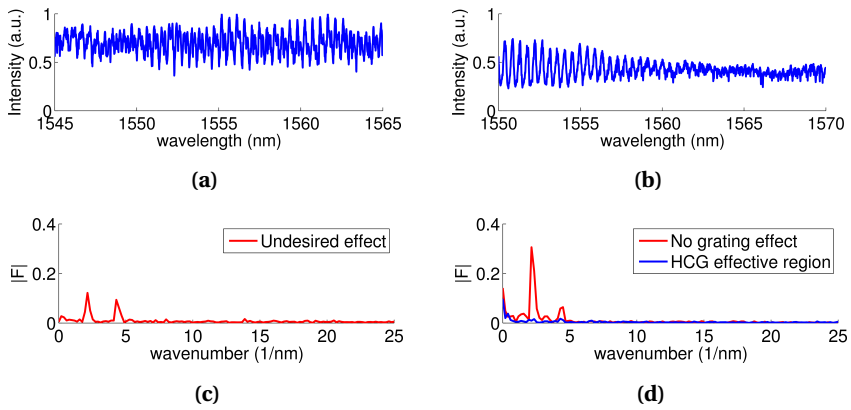

Figure 4.14: Transmission spectra of grating coupler combined with BCG (a) and HCG (b) in two locations. The BCG shows an unanticipated degradation of the signal. The grating effective region is clearly visible for the HCG. (c) and (d) show the Fourier spectra for BCG and HCG, respectively. In (d), the Fourier components are significantly reduced when comparing the spectrum outside the grating region of effect to the one inside the effective region.

where I_1 is the intensity of the light coupling directly into the waveguide through the grating coupler, I_2 is the intensity of the light coupling in the waveguide via reflections on the backside and $\Delta\phi$ accounts for the wavelength dependent path length difference between both interfering waves. In the case of a single dominant Fourier component, like in figures 4.12c, 4.12d and 4.14d the Fourier component represents the oscillating term of equation 4.9. It is thus proportional to the amplitude of the cosine term, or $2\sqrt{I_1 I_2}$. Comparing two Fourier spectra provides us then with a means to determine the reduction in intensity of the parasitic beam I_2 as a consequence of the implementation of the surface grating structures, assuming I_1 is unaffected by the anti-transmission gratings. The intensity reduction or grating suppression efficiency is given by:

$$\eta_{supp} = 10\log_{10}\left(\frac{I_{2,ref}}{I_{2,eff}}\right) = 10\log_{10}\left[\left(\frac{X_{ref}}{X_{eff}}\right)^2\right] \tag{4.10}$$

Here, X_{ref} and X_{eff} are the amplitudes of the dominant Fourier components outside and inside the grating's spectral region of effect, respectively. I_2 denotes the intensity in the corresponding spectral regions.

For the first-generation BCG in figure 4.12c, the signal originating from second-order reflections becomes dominant in the suppressed region where the 450 pm component is completely suppressed. Therefore, the strength of the Fourier component corresponding to 220 pm period oscillations should be

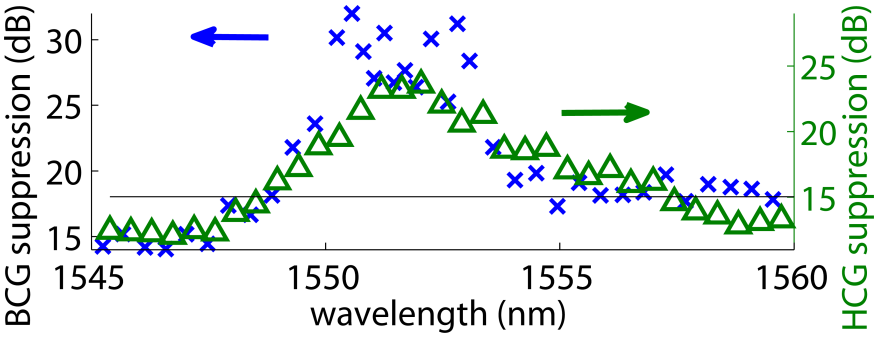

Figure 4.15: Wavelength dependency of the ratio I_1/I_2 for the first-generation high-contrast and backward-coupling gratings. The suppression threshold is indicated by a line. A higher maximum suppression is obtained for the BCG, but the HCG is effective over a wider wavelength range.

used for X_{eff} in equation 4.10. For the first-generation HCG in figure 4.12d, the 450 pm component remains dominant, so X_{eff} corresponds to the Fourier component of this period. This results in an efficiency of 12 dB for the BCG and an efficiency of only 10 dB for the HCG.

The second-generation HCG however, outperforms both implementations by an order of magnitude. In figure 4.14d, the Fourier components are almost completely suppressed in the effective region, which results in an efficiency of 25.5 dB. The obtained efficiencies are only representative for the grating effect around the central grating wavelength. To obtain a spectral representation of the grating efficiency, a more extensive analysis can be applied. The strength of the interference pattern is also apparent in the extinction ratio of consecutive fringes. From equation 4.9, the dependence of the ratio I_1/I_2 on the extinction ratio is analytically calculated to be:

$$\sqrt{I_1/I_2} = \frac{(1-x)}{-(1+x)+\sqrt{4x}} \tag{4.11}$$

with x the intensity ratio between consecutive maxima and minima of the spectrum. The + sign in the equation is determined by the assumption that I_2 has to be smaller than I_1. The result for the first-generation implementations is plotted in figure 4.15, for both the BCG and the HCG. To obtain this graph, a smoothing filter to suppress high frequency oscillations is applied to facilitate identification of local extrema.

Outside the grating effective region, we can determine a baseline level. Without grating effect, I_2 is found to be 12 to 15 dB weaker than the intensity of light coupling directly into the waveguide. We experimentally find an extinction

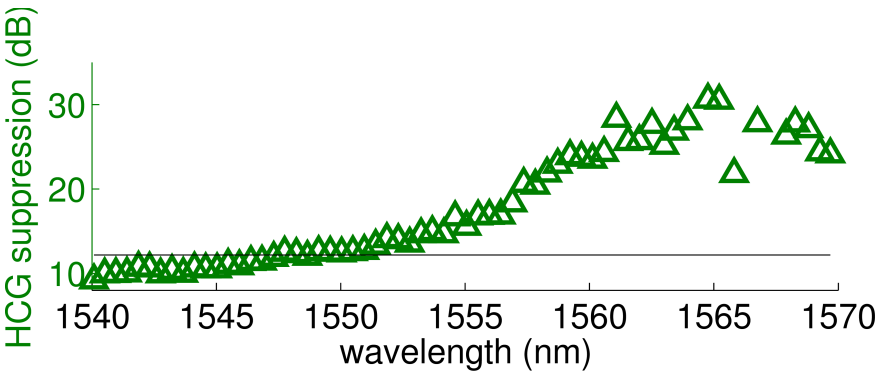

Figure 4.16: Wavelength dependency of the ratio I_1/I_2 for the second-generation high-contrast grating. The suppression threshold is indicated by a line. An additional suppression up to 20 dB is obtained over a wide wavelength range.

due to the BCG up to 27 dB, or 12 dB higher than the baseline. Here, we have to keep in mind that this number is limited by second-order reflections of the chip substrate. The direct transmission through the grating is practically completely eliminated, as suggested by the Fourier spectrum. If we set an arbitrary suppression threshold to an additional extinction of 3 dB, the bandwidth of the suppressed region is 6 nm, with a 4 nm region that exceeds 10 dB suppression. For the HCG, we calculate a reduction of the intensity I_2 up to 24 dB, or a suppression of 11 dB. The maximum suppression is reduced compared to that of the BCG, but the suppression threshold is exceeded over a wider range, i.e. 8 nm.

Figure 4.16 shows the wavelength dependent suppression ratio for the second-generation HCG. In this experiment, I_2 is found to be 10 dB smaller than I_1 outside the grating effective region. The maximum extinction of I_2 exceeds 30 dB, or an additional extinction in the HCG effective region up to 20 dB. This is slightly lower than the value obtained from the Fourier spectrum because noisy oscillations are an important contribution to the spectrum, so the two-beam Fourier approach overestimates the suppression. The bandwidth of the suppression region far exceeds 20 nm, with at least a 10 nm region exceeding 10 dB suppression (limited by the measurement range). In view of applications in biosensing with microring resonators, this behaviour fulfills the requirements. As the free spectral range of the microring sensors is 4 nm, we can always find a microring resonance inside the suppression regions. We notice the suppression efficiencies obtained from the spectral representation correspond very well to values calculated from the Fourier components.

Based on our measurement results, we have to make some additional re-

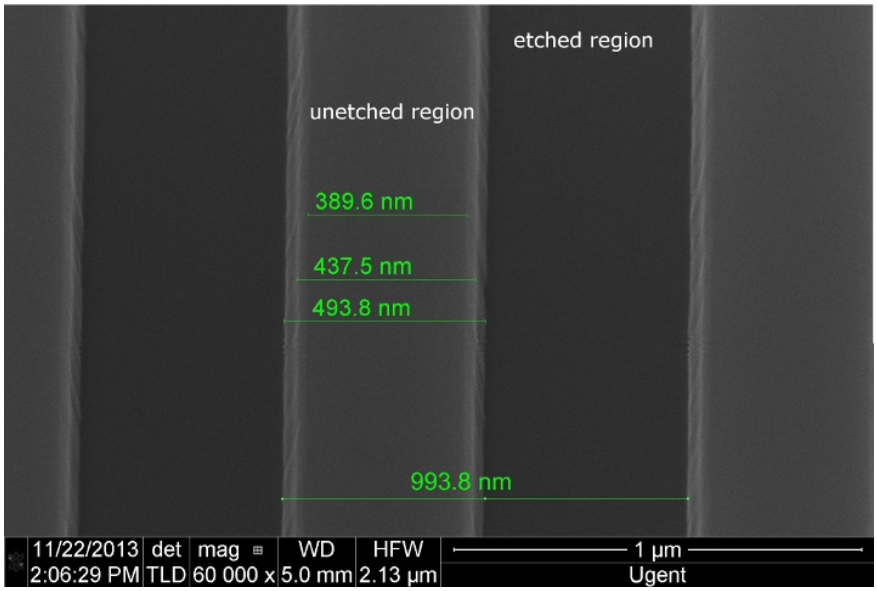

Figure 4.17: SEM top view showing deviations from the 1050 nm period with 50% fill factor in a fabricated high-contrast grating. Grating period and grating tooth width at different heights are indicated.

marks concerning the implementation of the anti-transmission gratings. The second-generation BCG does not perform as expected, because the waveguide to the slab region connects both gratings. A suggestion to solve this issue could be to taper the backward coupled light from the first BCG to the slab region before it reaches the second BCG. The 73 μm that separate both gratings are a sufficiently long distance to do this. The first implementations of a BCG with the appropriate operating wavelength show consistently efficient suppression of the parasitic light path. For the HCG on the other hand, the first-generation performance is significantly improved by adding a second grating to block second-order reflections. A drawback however is that we experimentally note a strong variation in the efficiency between different devices, with the 1050 nm period device performing considerably better than other implementations. Because the fabrication process can have a strong influence on the duty cycle and the side wall slope of the fabricated gratings, we can attribute many variations to fabrication issues. Indeed, in section 4.3.3 we have shown the strong dependence of the HCG transmission on the duty cycle. Sloped sidewalls can be expected to cause similar effects. Figure 4.17 shows a high-contrast grating with a theoretical period of 1050 nm and duty cycle of 50%. The dimensions of the fabricated device differ considerably from the design parameters. Especially the

slope of the sidewall of the grating tooth is important. The results discussed in this section suggest the implementation of two high-contrast anti-transmission gratings as the best approach to limit parasitic interferences in optical circuits, provided the fabrication process is stable or variations can be anticipated at the design stage.

4.5 Conclusion

For ease of use, the delicate fiber-chip interface should be avoided in complex integrated devices for a variety of applications. Instead, a collimated laser beam can be used for a robust coupling method with high alignment tolerance. In this chapter, we suggested a straightforward technique to reduce parasitic substrate reflections inherent to this approach. We demonstrated that implementing anti-transmission gratings to block parasitic light paths efficiently reduces coupling-induced interferences, without the need for additional processing steps. In particular, a high-contrast reflection grating and a grating that diffracts incoming light in the backward propagation direction of the waveguide were investigated. In a second generation, the second-order reflections were also suppressed by implementing two identical high-contrast gratings in the correct locations on the surface. A suppression efficiency of the coupling noise up to 20 dB was obtained for the high-contrast grating in a wavelength band exceeding 20 nm.

References

[1] G. Yurtsever, B. Považay, A. Alex, B. Zabihian, W. Drexler, and R. Baets. *Photonic integrated Mach-Zehnder interferometer with an on-chip reference arm for optical coherence tomography.* Biomedical Optics Express, 5(4):1050, March 2014.

[2] Y. Li, P. Segers, J. Dirckx, and R. Baets. *On-chip laser Doppler vibrometer for arterial pulse wave velocity measurement.* Biomedical optics express, 4(7):1229–35, July 2013.

[3] F. Van Laere, T. Claes, J. Schrauwen, S. Scheerlinck, W. Bogaerts, and D. Taillaert. *Compact Focusing Grating Couplers for Silicon-on-Insulator Integrated Circuits.* Optics Express, 19(23):1919–1921, 2007.

[4] K. De Vos, J. Girones, T. Claes, Y. De Koninck, S. Popelka, E. Schacht, R. Baets, and P. Bienstman. *Multiplexed Antibody Detection With an Array of Silicon-on-Insulator Microring Resonators.* IEEE Photonics Journal, 1(4):225–235, October 2009.

[5] Y. Li, D. Vermeulen, Y. De Koninck, G. Yurtsever, G. Roelkens, and R. Baets. *Compact grating couplers on silicon-on-insulator with reduced backreflection.* Optics letters, 37(21):4356–8, November 2012.

[6] D. Vermeulen, Y. D. Koninck, Y. Li, E. Lambert, W. Bogaerts, R. Baets, and G. Roelkens. *Reflectionless grating couplers for Silicon-on-Insulator photonic integrated circuits.* Optics Express, 20(20):1919–1921, 2012.

[7] Y. Li and R. Baets. *Improved multi-mode interferometers (MMIs) on silicon-on-insulator with the optimized return loss and isolation.* 2(Ldv):2–5.

[8] B. Aspar, M. Bruel, H. Moriceau, C. Maleville, T. Poumeyrol, A. Papon, A. Claverie, G. Benassayag, A. Auberton-Herve, and T. Barge. *Basic mechanisms involved in the Smart-Cut(R) process.* Microelectronic Engineering, 36(1):233–240, 1997.

[9] F. Van Laere, G. Roelkens, M. Ayre, J. Schrauwen, D. Taillaert, D. Van Thourhout, T. F. Krauss, and R. Baets. *Compact and Highly Efficient Grating Couplers Between Optical Fiber and Nanophotonic Waveguides.* Journal of Lightwave Technology, 25(1):151–156, 2007.

[10] D. Taillaert, F. V. Laere, M. Ayre, W. Bogaerts, D. V. Thourhout, P. Bienstman, and R. Baets. *Grating Couplers for Coupling between Optical Fibers and Nanophotonic Waveguides.* Japanese Journal of Applied Physics, 45(8R):6071, 2006.

[11] G. Roelkens, D. Vermeulen, S. Selvaraja, R. Halir, W. Bogaerts, and D. V. Thourhout. *Grating-Based Optical Fiber Interfaces for Silicon-on-Insulator Photonic Integrated Circuits.* IEEE J. Quantum Electron., 17(3):571–580, 2011.

[12] M. C. Huang, Y. Zhou, and C. J. Chang-Hasnain. *A surface-emitting laser incorporating a high-index-contrast subwavelength grating.* Nature Photonics, 1(2):119–122, February 2007.

[13] Y. Zhou, M. C. Y. Huang, and C. J. Chang-Hasnain. *Large Fabrication Tolerance for VCSELs Using High-Contrast Grating.* IEEE Photonics Technology Letters, 20(6):434–436, March 2008.

[14] D. Taillaert, W. Bogaerts, P. Bienstman, T. Krauss, P. van Daele, I. Moerman, S. Verstuyft, K. De Mesel, and R. Baets. *An out-of-plane grating coupler for efficient butt-coupling between compact planar waveguides and single-mode fibers.* Quantum Electronics, IEEE Journal of, 38(7):949–955, Jul 2002.

[15] D. Taillaert, P. Bienstman, and R. Baets. *Compact efficient broadband grating coupler for silicon-on-insulator waveguides.* Opt. Lett., 29(23):2749–2751, Dec 2004.

[16] V. Karagodsky, F. G. Sedgwick, and C. J. Chang-Hasnain. *Theoretical analysis of subwavelength high contrast grating reflectors.* Optics Express, 18(16):16973–88, August 2010.

[17] http://www-personal.umich.edu/~zlei/index.html. 2012.

[18] M. G. Moharam, T. K. Gaylord, E. B. Grann, and D. A. Pommet. *Formulation for stable and efficient implementation of the rigorous coupled-wave analysis of binary gratings.* J. Opt. Soc. Am. A, 12(5):1068–1076, May 1995.

[19] M. G. Moharam, T. K. Gaylord, D. A. Pommet, and E. B. Grann. *Stable implementation of the rigorous coupled-wave analysis for surface-relief gratings: enhanced transmittance matrix approach.* J. Opt. Soc. Am. A, 12(5):1077–1086, May 1995.

[20] P. Lalanne and G. M. Morris. *Highly improved convergence of the coupled-wave method for TM polarization.* J. Opt. Soc. Am. A, 13(4):779–784, Apr 1996.

5 Resonance splitting

In this chapter, we present an integrated interferometric approach to resolve the resonance splitting of a microring resonantor on a single chip. In section 5.2, the origin of resonance splitting is discussed. Different contributions that lead to splitting are considered and some implications on the microring operation are analyzed. The integrated interferometric circuit that gives access to the unsplit normal modes of the microring is introduced in section 5.3. The fabrication of the optical chip and practical calibration steps that are necessary to obtain the experimental results are discussed in section 5.4. Finally, in 5.5 the developed theoretical model is confirmed by experimental results and an improvement of the resonance quality by a factor of 3 is obtained.

5.1 Introduction

The high index contrast of the silicon-on-insulator platform (SOI) has an important role in the successful application of integrated microring biosensors. It leads to a high confinement of the optical fields in the waveguide, which enables small bend radii and very small sensor sizes. The high optical intensity in the ring makes it very sensitive to changes on its waveguide surface. This explains the very high sensitivity to refractive index changes when biomaterials bind to the ring. However, this high contrast also makes the optical mode very sensitive to some undesired effects, like scattering of the guided light on

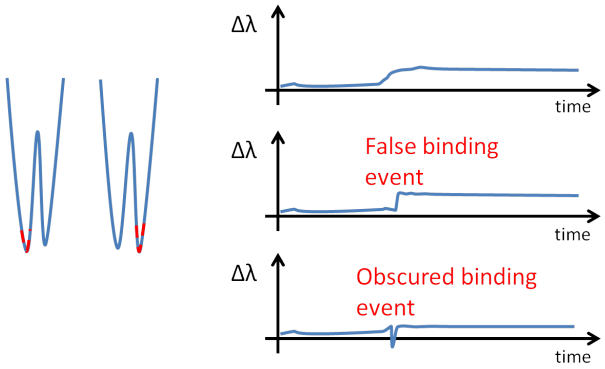

Figure 5.1: Unpredictable resonance splitting can introduce errors in a binding curve. Fitting errors can result in false positive or even false negative results.

roughness of the waveguide edges. This causes optical losses in the waveguide that degrade the quality factor of the resonances. When the scattering leads to reflections to the opposite propagation direction in the waveguide, this can ultimately result in splitting of the microring resonance [1]. Because the detection limit of a microring biosensor is directly related to the quality of the ring resonance, a high Q-factor is of primordial importance in sensing applications [2]. Moreover, the consequences of resonance splitting can become even worse. In a biosensor device, the resonance wavelength will be tracked automatically by a fitting algorithm. This works fine for unsplit resonances, but unpredictable resonance splitting can introduce errors in the recorded binding curve signal, as explained by figure 5.1. Since the resonance splitting in a microring sensor can easily amount to a measurable erroneous shift, unexpected resonance splitting can result in fitting errors and severely compromise a recorded binding curve.

5.2 Origin of resonance splitting

As discussed in chapter 2.3, if backreflection of optical power enables coupling between the clockwise (CW) and counterclockwise (CCW) mode of a microring resonator, the degeneracy of the resonance is lifted and the spectrum can feature resonance splitting. Whether the splitting is visible in the output spectrum depends on the losses in the microring. In [3], it is determined that the resonator response becomes severely degraded if the backreflected power exceeds the coupling losses for an ideal resonator. Because high-quality microrings for sensing applications require low coupling factors, minor reflection

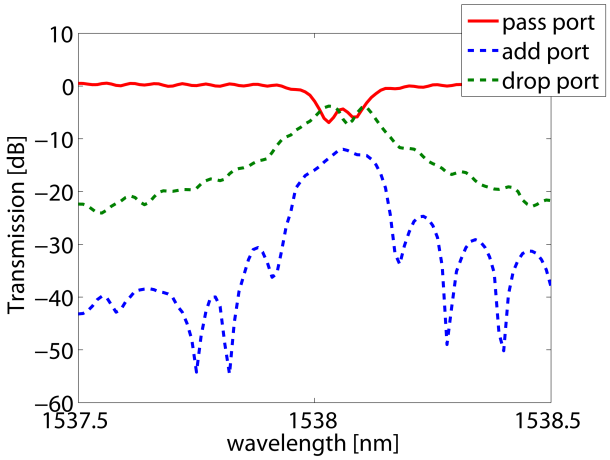

Figure 5.2: Measured spectra for add-drop microring resonator showing resonance splitting and backscattered power.

levels can already lead to significant splitting in the output spectrum

Evidence of the importance of backreflected power is provided in figure 5.2, which shows both the pass-port and add-port spectrum of a microring in add-drop configuration. The microring is designed to have a roundtrip length of 36 μm and a power coupling ratio of 6 percent. Since only the input port is excited, no power should be present in the CCW mode and the add port should remain dark. The measurement shows that backscattering in the microring waveguide cannot be neglected, resulting in significant power in the add port and resonance splitting in the pass-signal amounting up to 50 pm.

When backreflection is present in a microring resonator, superpositions of the CW and CCW mode become the eigenmodes of the system. In 2.3, it is derived that the standing modes a_+ and a_-, given by equation 5.1 are these new eigenmodes:

$$\begin{aligned} a_+ &= \frac{1}{\sqrt{2}}(a_{CW} + a_{CCW}) = \frac{1}{\sqrt{2}} \frac{-\kappa s}{i\left(\Delta\omega + \frac{1}{2\gamma}\right) - \frac{1}{2\tau}} \\ a_- &= \frac{1}{\sqrt{2}}(a_{CW} - a_{CCW}) = \frac{1}{\sqrt{2}} \frac{-\kappa s}{i\left(\Delta\omega - \frac{1}{2\gamma}\right) - \frac{1}{2\tau}} \end{aligned} \tag{5.1}$$

Here, the scattering lifetime γ represents the coupling between the travelling modes. The factor κ is the coupling between the bus waveguide and the microring. s is the amplitude of the input field in the bus waveguide. From equation 5.1, it is clear that the eigenmodes are centered around the new eigenfrequencies $\omega = \omega_0 \pm 1/2\gamma$. They each have a linewidth of $1/\tau$, determined by the losses of the coupled microring. The results from equation 5.1 can be used to

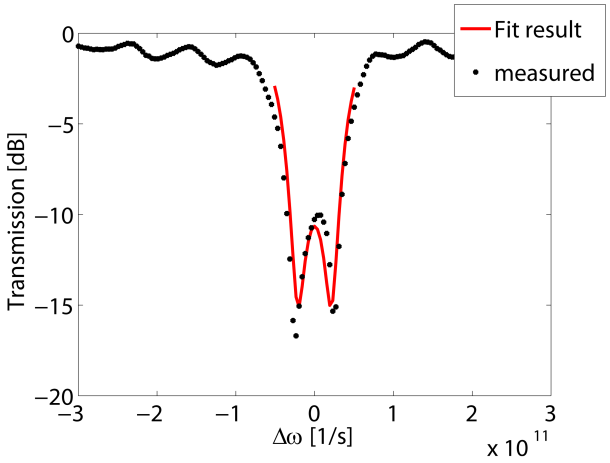

Figure 5.3: Measured spectrum of all-pass microring with resonance splitting. The full line gives the theoretical transmission after fitting the model parameters.

parameter		chacteristic	
κ	$2.1 \times 10^5 s^{-1/2}$	K^2	0.033
γ	$1.6 \times 10^{-11} s$	$\Delta\lambda$	79 pm
τ	$1.7 \times 10^{-11} s$	Q	20850

Table 5.1: Model parameter values for the split resonance.

calculate both the CW and CCW mode as well as the transmitted and reflected fields for the microring coupled to an input waveguide by using the relations from equation 5.2:

$$t = s + \kappa a_{CW} \quad \text{and} \quad r = \kappa a_{CCW} \tag{5.2}$$

When comparing the theoretical transmission to the recorded transmission spectrum of an all-pass microring resonator, we obtain the results from figure 5.3. The resulting fitted parameter values indicate a quality factor of $Q = 20850$ for the eigenmodes a_+ and a_-. The mode splitting amounts to $\Delta\lambda = 79\,\text{pm}$ and the power coupling ratio of the directional coupler is $K^2 = 0.0332$, which corresponds well to the projected design value for critical coupling. K can be related to κ by expressing the coupled energy per round trip, $K^2 = \kappa^2 \frac{2\pi R}{v_g}$. These parameters are summarized in table 5.1.

For these experimentally determined parameters, we can investigate the

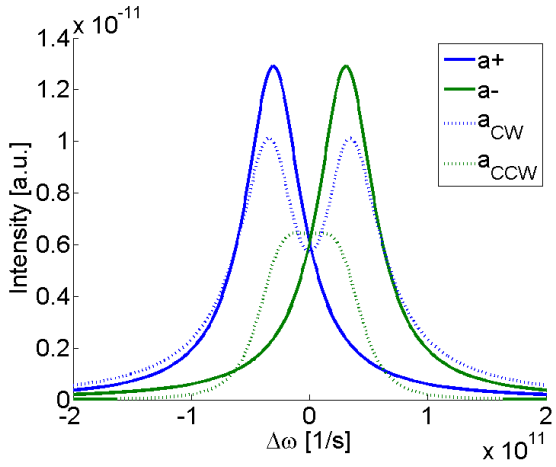

Figure 5.4: Normal modes and travelling modes in a microring resonator with resonance splitting. The microring parameters are given by table 5.1.

characteristics of the microring modes. Their spectral intensity distribution is given in figure 5.4. This shows the normal modes with a Lorentzian distribution, centered around their corresponding resonance frequencies $\omega_0 \pm 1/2\gamma$. It is interesting to note that the peaks appearing in the a_{CW} spectrum do not correspond exactly to the resonances of the normal modes. The a_{CCW} on the other hand shows hardly any visible resonance splitting. The peaks in the spectrum are obscured and the splitting results in a broadening and flattening of the reflection band of the resonator. The spectral shapes of the traveling wave modes depend on the relation between the mode splitting $1/\gamma$ and the losses $1/\tau$. When the splitting is high compared to the losses, both a_{CW} and a_{CCW} will show a clearly split spectrum. When the splitting is much lower than the losses, the splitting in the spectrum is obscured by the broad resonance linewidth. In that case, the backreflection only results in an additional broadening of the resonance. Even though the resonator is symmetric for the CW and CCW mode, both modes show a very different spectrum. This is because the excitation in the bus waveguide is not symmetric, an effect explained in detail in [4]. A detailed analysis of resonance splitting due to mutual coupling is provided in [5].

It is important to mention that different resonance orders show different splitting in experiments, i.e. the amount of resonance splitting in a resonator mode is strongly dependent on the wavelength. This is because the roughness of the waveguide edges is an important contribution to the backreflection, and the exact phase relation between different reflecting contributions determines

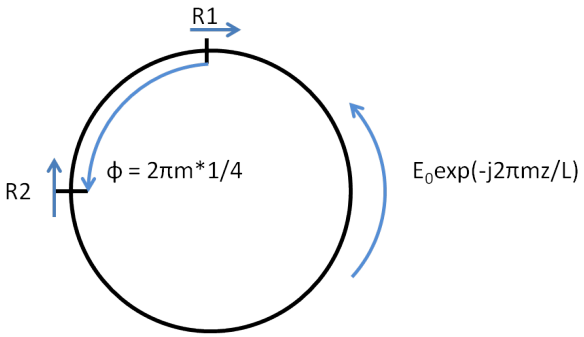

Figure 5.5: Schematic representation of a microring with distributed reflection sites. The resulting resonance splitting is strongly dependent on the resonator mode.

the total reflection. Another possible contribution to the reflected power comes from the proximity of the bus waveguide, which also causes reflections. It is difficult to distinguish both contributions and estimate which one is more important. However, because the reflections of the coupler section interfere constructively for every resonator mode while the strength of the distributed reflections on the waveguide roughness differs for different resonator modes, the observed behaviour of mode-dependent resonant splitting suggests a regime where the waveguide roughness is the dominant contribution.

The importance of the phase relation between different contributions of distributed reflections can easily be understood by considering a theoretical resonator. This is explained in figure 5.5. Assume the resonator has two equally strong reflection sites R_1 and R_2, separated by a quarter round trip. For the first order resonance ($m = 1$), the light reflected from R_2 will arrive at R_1 and cancel the light reflected there because of destructive interference. The phase difference between both contributions is indeed π. For the same resonator, but considering the second order resonance ($m = 2$), both reflected contributions will be exactly in phase and interfere constructively, leading to a strong coupling between both counterpropagating modes and a split resonance. This reasoning can be extended to proof a perfectly homogeneously distributed reflection does not cause resonance splitting. This can also be understood theoretically, because such a reflection does not break the symmetry of the microring (making abstraction of the coupling section), so the degeneracy is preserved. It has to be stressed that a random distribution of reflection sites differs fundamentally from homogeneous reflection [6]. To correctly describe resonance splitting due to waveguide roughness variations, a statistical description of the reflection has

to be applied, as described in [3].

The intensity distribution of the standing wave normal modes leads to a another physical explanation for the observed resonance splitting. This is easiest to understand for a single reflecting particle on the ring. When a particle binds to the ring, the normal modes are redistributed. Because the presence of the particle redefines the symmetry of the microring, the modes are redistributed such that the reflecting particle coincides with an antinode for the symmetric supermode, while it is located in a node for the antisymmetric supermode. Because the antisymmetric mode does not feel the presence of the particle - the light intensity in the node is zero - it does not experience a wavelength shift. The symmetric mode on the other hand, has maximum overlap with the higher index particle. This results in a increase in refractive index for this mode and a resonance wavelength shift. This technique has been used for single particle detection in ultra-high Q resonators [7]. In practice, this means the intensity distribution of the standing waves for split resonator modes results in a different average refractive index for both normal modes.

5.3 Integrated interferometric circuit

As demonstrated in [8], in the context of a fiber-based system, an interferometric approach can be used to retrieve the unsplit modes of the microring resonator in an output signal. However, such a fiber-based setup is difficult to stabilize and to integrate. Therefore, we have implemented this in an integrated circuit on a single SOI-chip. A layout of the circuit is provided in figure 5.6. Vertical grating couplers are used to couple light from a tunable laser lightsource into the circuit and collect the power at the output. The input light excites the CW mode in the microring resonator, which in turn excites the CCW mode as a consequence of mode coupling. The normal modes of the microring resonator are the symmetric and antisymmetric superposition of the CW and CCW mode, given by equation 5.1. If the coupling per unit time between the bus waveguide and the microring is represented by κ, the fields transmitted and reflected by the resonator are again given by equation 5.2. Here, $s = a_{in}/\sqrt{2}$ and $|a_{in}|^2$ is the total input power.

The input light first passes through a 3dB combiner before coupling to the microring. The CW propagating light will couple back to the waveguide to constitute the transmitted field. The CCW propagating light will form the reflected field when coupling back to the waveguide. The input combiner acts as a splitter for the reflected light which is guided through a feedback arm towards a 2x2 multi mode interference (MMI) coupler. The transmitted light is passed to a 3dB MMI-splitter. It is split equally between output 1 and the 2x2 MMI coupler, where it is recombined with the reflected light. The signals from the 2x2 cou-

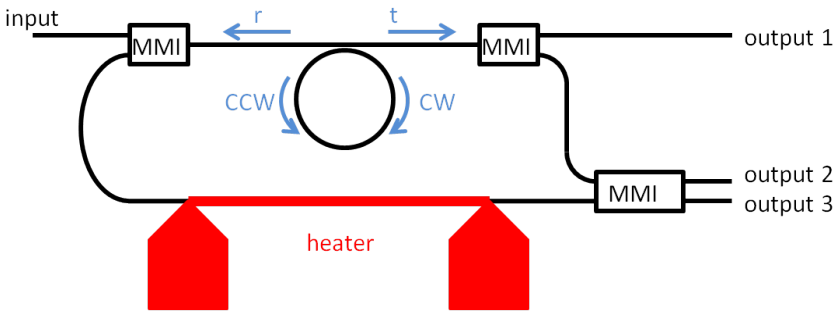

Figure 5.6: Schematic representation of the integrated interferometric circuit.

pler are the result of interference between the transmitted and reflected fields and are collected in output 2 and 3. For the case of a perfect 2x2 MMI coupler, the fields at the output ports for given input fields E_1 and E_2 are $1/\sqrt{2}\,(E_1 \pm iE_2)$. There is a quadrature phase relationship between both output signals. We can summarize the output fields of the interferometric circuit in equation 5.3:

$$\begin{aligned} out_1 &= \tfrac{1}{\sqrt{2}}\,t \\ out_2 &= \tfrac{1}{2}(\tfrac{1}{\sqrt{2}}\,a_{in} + \kappa a_{CW} + e^{i\phi}\kappa a_{CCW}) \\ out_3 &= \tfrac{1}{2}(\tfrac{1}{\sqrt{2}}\,a_{in} + \kappa a_{CW} - e^{i\phi}\kappa a_{CCW}) \end{aligned} \tag{5.3}$$

Here, ϕ is the phase difference between the interfering transmitted and reflected fields. We find that output 1 is always proportional to the pass-signal of the microring resonator in the all-pass configuration. To obtain the required output signals (a_+ and a_-) in output 2 and 3, the phase difference ϕ between the transmitted and reflected wave has to be controlled carefully. In this case, this is done by processing a titanium-gold heater on the feedback waveguide. By setting the current through the heater, we can tune the phase difference to the required value. If it is a multiple of π, we see from equation 5.3 that the signals in output 2 and 3 are given by the sum of a constant and a signal proportional to the complex amplitudes of the normal modes a_+ and a_- of the resonator, given by equation 5.1. In other words, the spectral shape of the signals in output 2 and 3 will be identical to this of the complex amplitudes of the eigenmodes. This means we will have access to the unsplit, high-Q normal modes of the cavity. Since the detection limit of a biosensor is limited by the quality factor of the resonance [9] - higher Q-factors give rise to lower detection limits - this provides a tool to improve the detection limit significantly.

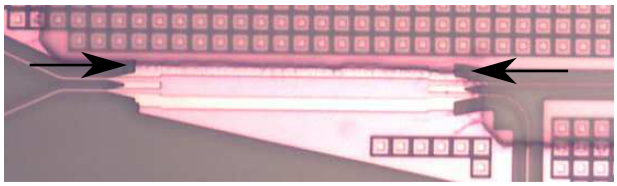

Figure 5.7: Microscope image of lithographically opened BCB layer. The arrows indicate the edge of the 2x2 MMI that is covered by BCB residue.

5.4 Fabrication and calibration

The circuit from figure 5.6 is designed and processed in a CMOS pilot line at imec. Using the vertical in- and output couplers on the waveguides [10], the chip can easily be characterized in a fiber-to-fiber configuration. The process of depositing tuning heaters on the feedback waveguide is straightforward and does not require any high-accuracy alignment steps. To limit optical losses induced by the heater metal, a polymer layer of approximately 1 μm is deposited on the chip surface prior to heater definition. For this layer, the photopatternable resin Cyclotene 4022-25 [11] is used to allow the definition of windows over critical device structures. The polymer is derived from B-staged bisbenzocyclobutene (BCB) and is widely used for various post-processing steps on SOI-chips for near-infrared applications [12]. After developement, we remove the photo-BCB covering the microring, grating couplers and 2x2 MMI.

Figure 5.7 shows the 2x2 MMI and the edge of the BCB layer. The tuning heater is then processed on the chip with locally opened BCB cover. For that purpose, a lithographic lift-off procedure is used [13]. The heater measures 450 by 2.5 μm with large contact pads for easy probing. For characterization of the tuning heater, a Mach-Zehnder-Interferometer (MZI) is used.

Because of the large thermo-optic effect in silicon [14], the refractive index changes with temperature. The refractive index change is proportional to the temperature and thus to the dissipated power in the heater. This leads to equation 5.4 for the phase difference between the MZI-arms:

$$\Delta\phi = \phi_0 + \alpha I^2 \tag{5.4}$$

In equation 5.4, ϕ_0 is the phase difference at zero current and α is a proportionality constant. The proportionality constant α can be determined by fitting a cosine squared interference pattern to the MZI intensity for different heater currents. The result is shown in figure 5.8. The quadratic relationship between heater current and phase change is determined as $\phi = 0.4\,\mathrm{rad/mA^2} \times I^2$. This confirms the phase change in the heated waveguide is proportional to the dis-

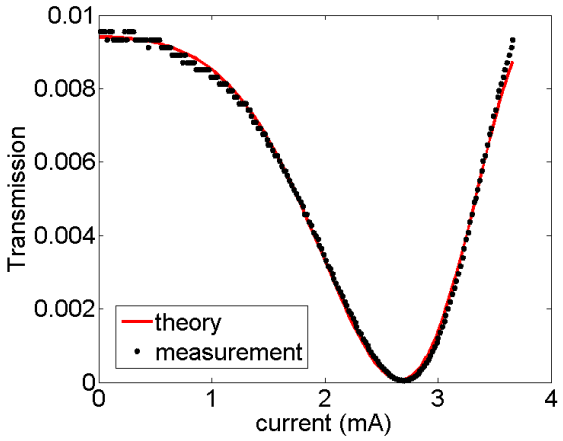

Figure 5.8: Phase dependent interference pattern of the MZI for different heater currents.

sipated power in the metallic heater. The resulting calibration curve is shown in figure 5.9. A phase range of 2π is obtained for heater currents from 0 to 4 mA.

Because the microring on the chip is separated from the heater by only a couple of micrometers, the microring experiences a thermal tuning effect. This results in a positive wavelength shift for increasing current values. Just like the phase change in the MZI-arm, the resonance wavelength shift in the ring is also quadratically dependent on the current through the heater. As a consequence, the resonance wavelengths have to be corrected when recording the output spectra of the interferometric circuit at different heater currents. Figure 5.10 shows the observed resonance wavelengths in outputs 2 and 3 together with their theoretically predicted value, based on a quadratic dependence on the heater current. Notice that a temperature change of 1°C corresponds to a resonance wavelength shift of approximately 60 pm in a microring. Because all spectra are recorded sequentially, the observed small wavelength variations fall withing reasonable distances of the theoretical predictions.

5.5 Experimental results

The fabricated chip with integrated interferometric circuit is mounted on a vertical optical setup for fiber-to-fiber characterization. To obtain the measured spectra, a TUNICS tunable laser source is used to generate the input signals. Output intensities are measured by a HP-8153 optical power meter. The laser wavelength is swept in 5 pm steps while the optical power is recorded. By

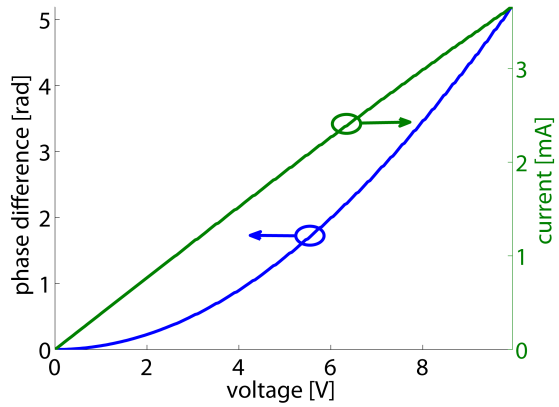

Figure 5.9: Calibration curve for tuning heater. A phase range of 2π is obtained for heater currents from 0 to 4 mA.

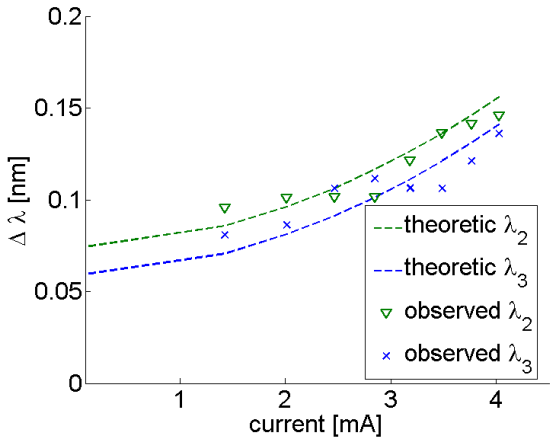

Figure 5.10: Variation in microring resonance wavelength due to parasitic heating of the resonator.

fitting a 4th-oder polynomial to a reference spectrum of a straight waveguide, the effect of the vertical grating couplers can be substracted from the data. The remaining oscillations in the measured spectra can be attributed to the wavelength dependency of the splitters and the MMI coupler. The output spectra are recorded for different heater currents. Since the relation between heater current and phase change is known thanks to the calibration, the spectra can be recorded at $\Delta\phi = \pi/4$ phase intervals. The entire phase range of 2π is available. Comparison of a recorded spectrum to the theoretical predictions provides us with a reference to determine the heater current (and heater phase shift) that corresponds to a total phase difference of 0. Setting the heater current gives us the ability to change the resonance state in the output signals from one normal mode, over the severely split intermediate state to the other normal mode.

This is demonstrated in figure 5.11 where recorded spectra of the output couplers are shown for different phase differences between the interfering waves. In this figure, the theoretically predicted output signals according to equation 5.3 are also provided. The values for the model parameters are given by table 5.1. The correspondence between theory and experiment shows we have a good understanding of the physical effects in the microring resonator. We have to remark the 2x2 MMI is particularly sensitive to processing variations that affect its transmission characteristics. The proximity of the BCB layer to one edge of the MMI, which can be seen on figure 5.7, generates an assymetric coupler transmission. This results in an extra phase shift of approximately $\pi/2$ in the transmission from input port 2 to output port 3, which was determined by fitting. This phase change has been accounted for in the theoretical model.

The relation between the extinction ratios of the different ouput signals depends on the coupling from the microring to the waveguide. The critical coupling condition for the normal modes is achieved at a lower coupling ratio than that for the transmitted signal. In this working regime, the normal modes are overcoupled and the transmitted signal is undercoupled. If the coupling is reduced, the normal modes in the resonator approach the critical coupling condition and the extinction ratio increases. At the same time, the extinction ratio in the transmitted signal is recuded because the resonator becomes more undercoupled for the pass configuration.

The width and corresponding quality factors of the recorded eigenmode spectra compare favourably to those of the resonance signal in output 1, as can be seen from figure 5.12. When determined based on the fitted model of equation 5.1, we obtain a width of 50 pm for the unsplit eigenmodes and one of 130 pm for the split all-pass transmission. Since the limit of detection (LOD) scales with the square root of the resonance width, this technique provides a potential LOD improvement with a factor 1.6. One could argue that the total width of the transmission resonance is not a good measure for estimating de-

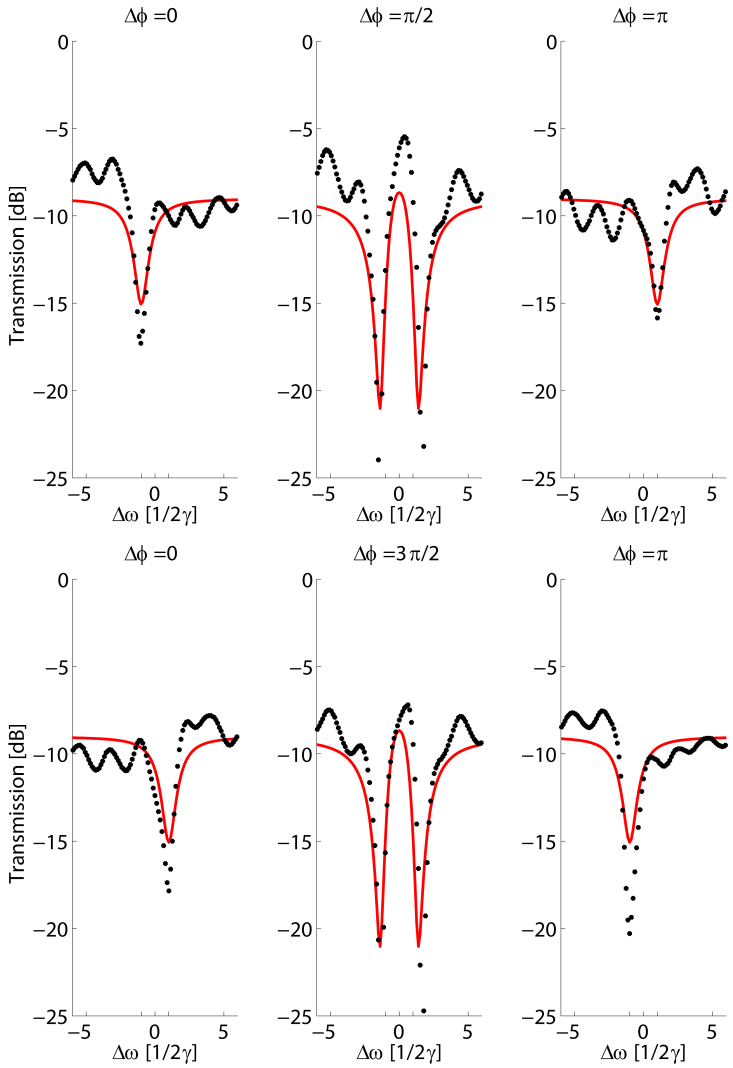

Figure 5.11: Interferometric output signals for different phase difference between reflected and transmitted field: (top) output 2 (bottom) output 3. The full line gives the theoretically predicted signals and the dotted line gives the experimentally recorded power.

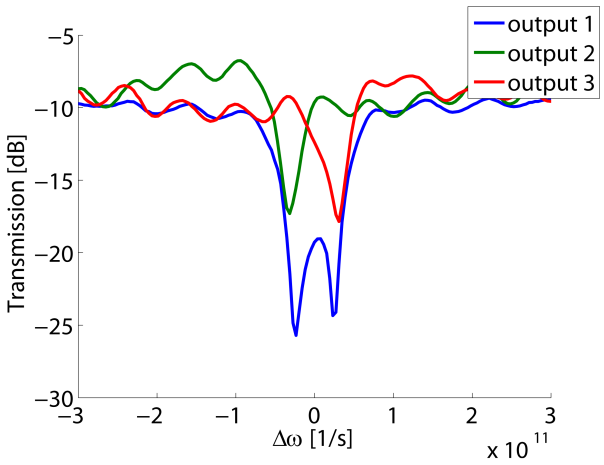

Figure 5.12: Split all-pass transmission and interferometric output signals showing unsplit modes for a phase difference $\Delta\phi = 0$. Output power of output 1 has been scaled for clarity.

tection limits. However, when the resonance splitting $\Delta\lambda$ is less than or equal to the width of the individual normal modes, splitting will be obscured while still causing significant broadening of the resonance dip. In that case, a fit to the more narrow unsplit mode revealed by this interferometric approach will always be more accurate and provide limit of detection improvements up to a factor $\sqrt{2}$, while at the same time eliminating the chance of false positive or negative detections due to intrinsic microring effects.

5.6 Conclusion

In this chapter, we demonstrate the successful integration of an interferometric circuit to resolve resonance splitting on a SOI-chip. A detailed discussion of the effect contributing to resonance splitting in microring resonators is given. We also show that a simple theoretical model of coupled harmonic oscillators can adequately describe the microring mode splitting. Using a tuning heater, we can sweep the phase difference between the combining reflected and transmitted fields of the microring and change the output signals from a severely split spectrum to the unsplit microring modes with high quality factors. The theoretical predictions are confirmed by the experiment. When comparing the output signals of the interferometric circuit to the split resonance of the all-pass microring, the resonance width is reduced by approximately a factor 3. This can

result in a limit of detection improvement by a factor 1.6, while at the same time eliminating the chance of false positive or negative detections due to intrinsic splitting of the microring resonance.

References

[1] W. Bogaerts, P. D. Heyn, T. V. Vaerenbergh, K. D. Vos, S. Kumar, T. Claes, P. Dumon, P. Bienstman, D. V. Thourhout, and R. Baets. *Silicon Microring Resonators.* Laser & Photonics Reviews, 6(1):47–73, 2011.

[2] T. Claes, J. Molera, K. De Vos, E. Schacht, R. Baets, and P. Bienstman. *Label-Free Biosensing With a Slot-Waveguide-Based Ring Resonator in Silicon on Insulator.* IEEE Photonics Journal, 1(3):197–204, September 2009.

[3] B. E. Little, J. P. Laine, and S. T. Chu. *Surface-roughness-induced contradirectional coupling in ring and disk resonators.* Optics Letters, 22(1):4–6, January 1997.

[4] J. Ctyroky, I. Richter, and M. Sinor. *Dual resonance in a waveguide-coupled ring microresonator.* Optical and Quantum Electronics, 38(9-11):781–797, 2006.

[5] Z. Zhang, M. Dainese, L. Wosinski, and M. Qiu. *Resonance-splitting and enhanced notch depth in SOI ring resonators with mutual mode coupling.* Optics Express, 16(7):4621–4630, Mar 2008.

[6] X. Yi, Y.-F. Xiao, Y.-C. Liu, B.-B. Li, Y.-L. Chen, Y. Li, and Q. Gong. *Multiple-Rayleigh-scatterer-induced mode splitting in a high-Q whispering-gallery-mode microresonator.* Phys. Rev. A, 83:023803, Feb 2011.

[7] J. Zhu, S. K. Ozdemir, Y.-F. Xiao, L. Li, L. He, D.-R. Chen, and L. Yang. *On-chip single nanoparticle detection and sizing by mode splitting in an ultrahigh-Q microresonator.* Nature Photonics, 4(1):46–49, January 10 2010.

[8] J. Knittel, T. G. McRae, K. H. Lee, and W. P. Bowen. *Interferometric detection of mode splitting for whispering gallery mode biosensors.* Applied Physics Letters, 97(12):123704, 2010.

[9] J. Hu, X. Sun, A. Agarwal, and L. C. Kimerling. *Design guidelines for optical resonator biochemical sensors.* J. Opt. Soc. Am. B, 26(5):1032–1041, 2009.

[10] G. Roelkens, D. Vermeulen, S. Selvaraja, R. Halir, W. Bogaerts, and D. V. Thourhout. *Grating-Based Optical Fiber Interfaces for Silicon-on-Insulator Photonic Integrated Circuits.* IEEE J. Quantum Electron., 17(3):571–580, 2011.

[11] T. D. C. Company, *http://www.dow.com/cyclotene/prod/402235.htm.* May 2013.

[12] S. Stankovic, R. Jones, J. Heck, M. Sysak, D. Van Thourhout, and G. Roelkens. *Die-to-Die Adhesive Bonding Procedure for Evanescently-Coupled Photonic Devices.* Electrochemical and Solid-State Letters, 14(8):H326, 2011.

[13] K. V. Acoleyen, K. Komorowska, and W. Bogaerts. *One-Dimensional Off-Chip Beam Steering and Shaping Using Optical Phased Arrays on Silicon-on-Insulator.* Journal of Lightwave Technology, 29(23):3500–3505, 2011.

[14] P. Dumon, G. Priem, L. R. Nunes, W. Bogaerts, D. V. Thourhout, P. Bienstman, T. K. Liang, M. Tsuchiya, P. Jaenen, S. Beckx, J. Wouters, and R. Baets. *Linear and Nonlinear Nanophotonic Devices Based on Silicon-on-Insulator Wire Waveguides.* Japanese Journal of Applied Physics, 45(8S):6589, 2006.

6

Microring resonators with integrated vertical coupling grating

The small size of SOI microring resonator biosensors is one of their key advantages, especially for multiplexed applications. However, classical photonic biosensor setups rely on access waveguides on the chip surface to couple optical signals to the microring resonators. These waveguides enable straightforward coupling of the optical signals in and out of the chip using vertical grating couplers while at the same time guiding the signals on the chip surface to the sensors with very low losses. When the number of sensors increases, the grating couplers and waveguide routing quickly take up more chip surface than the actual rings. For densly multiplexed applications, with several hundreds or even thousands of sensors in parallel, this on-chip waveguide routing takes up so much space that it becomes practically impossible to combine such a high number of sensors on a chip. Therefore, we suggest in this chapter to combine microring resonators with local weak gratings to read out light directly from the microring while still maintaining high quality factors that are required for sensing applications. In section 6.2, the design of the microring with grating is discussed. Section 6.3 analyzes the theoretical performance of the component based on simulation results. Finally, the section 6.4 focuses on the characterization and proof-of-principle experiments of microring resonators with integrated weak gratings.

6.1 Motivation

Silicon-on-insulator photonic microring resonators have proven to be excellent components for sensing applications partly because of their ability to perform multiplexed assays. This is demonstrated in [1] by combining the detection of different antibodies with negative controls on a single chip. In recent years, faster read-out techniques [2] and higher degrees of multiplexing have been demonstrated [3], with chips containing up to 128 sensors in a single microarray [4]. In that design, it becomes clear that the waveguide routing starts to take up significant surface on the chip, even with the relatively large microring configuration that is adopted for the sensor. Our own microarray design of 64 parallel sensors in figure 6.1 also clearly shows the large surface fraction taken up by waveguide routing and grating couplers. For next-generation applications like on chip DNA-sequencing, several hundreds or even thousands of microring sensors are required to operate in parallel [5]. For such high levels of multiplexing, the waveguide routing on the chip surface remains challenging. By combining a microring resonator with a weak grating, part of the light resonating in the microring is diffracted out of the chip and can be read out directly, while still maintaining a high quality factor in the ring which is required for most applications. Some configurations of microrings with gratings have been investigated for various applications like improved filter characteristics or higher quality factors [6, 7]. But in this chapter, we investigate in detail a microring with grating for direct interrogation, without the need for output waveguides and output grating couplers on the chip surface, similar to the one described in [8]. However, by adopting a weak grating approach, the resonance maintains a much higher quality factor. Through future research and optimizations, this technique could be further developed to use the same grating for both in- and outcoupling of the microdisk and eliminate surface consuming waveguide routing alltogether.

6.2 Ring design and fabrication

We have designed microring resonators combined with a weak grating that couples light directly out of the ring. The microring consist of a 450 nm wide waveguide. The grating is created by etching slits in the silicon top layer of 220 nm until the buried oxide layer is reached, and is defined in the same lithographical step as the microring resonator. The weak grating effect is obtained by spatially separating the grating region from the silicon waveguide. This way only the evanescent tail of the waveguide mode interacts with the grating and we can assume a weak interaction between both. Diffraction in the vertical direction is chosen because the grating will couple both resonator modes (clockwise and

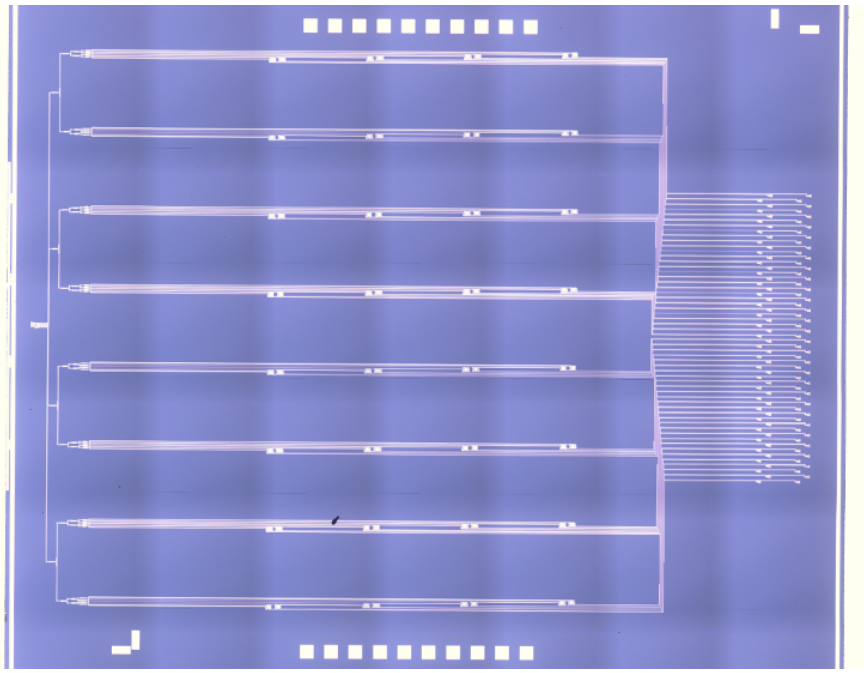

Figure 6.1: Sensor array of 64 parallel sensors. The waveguide routing and grating couplers take up significant chip surface.

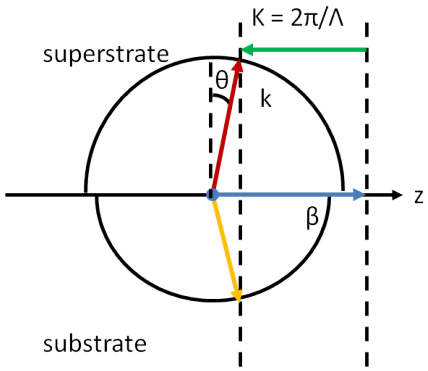

Figure 6.2: Bragg diagram for vertical coupling from a waveguide mode.

counterclockwise) equally strong and to the same direction. From the previous chapter we know both modes are present in the microring due to backreflection. The additional refractive index steps at the grating edges will most likely

increase this reflection. It is thus best to design the grating such that both modes are coupled out of the ring together, to avoid losing half of the power when both modes are diffracted in opposite directions. To design the grating period for vertical coupling around a working wavelength of 1550 nm, the Bragg condition 6.1 is used, as depicted in figure 6.2.

$$\beta + mK = k\sin(\theta) \tag{6.1}$$

β is the propagation constant of the waveguide mode, $K = \frac{2\pi}{\Lambda}$ the reciprocal lattice constant of the grating and k is the wavevector of the diffracted light with an angle θ. Because of the weak interaction of the waveguide mode with the grating, we will first assume the waveguide propagation constant $\beta = \frac{2\pi}{\lambda} n_{eff}$ in the grating region to be approximately equal to that of the fundamental TE-mode with an effective index of $n_{eff} = 2.84$. For first order diffraction in the vertical direction, the integer $m = \pm 1$ and $\theta = 0$. This results in equation 6.2 for the period of the grating Λ.

$$\Lambda = \frac{\lambda}{n_{eff}} = 547\,nm \tag{6.2}$$

By using a fill factor of 50% and a grating period of 547 nm we create a first order grating that maximizes diffraction from the waveguide to the vertical direction. For experimental characterization, devices with different grating parameters such as grating period, grating length and grating-to-waveguide gap are fabricated on SOI chips in a complementary metal-oxide-semiconductor (CMOS) pilot line [9] at imec.

A Scanning Electron Micrograph (SEM) of the microring resonator waveguide with weak grating on both sides of the waveguide is shown in figure 6.3. For this proof-of-principle demonstration, we use microrings in the all-pass configuration for easy characterization of different grating parameters on a vertical fiber setup. The weak gratings are located in the vicinity of the ring waveguide on the opposite side of the ring with respect to the coupling waveguide. The grating functions as a drop port for the microring and diffracts light upward, where it can be collected by a camera.

The CMOS fabrication of the components results in some undesired deviations from the original design. Proximity effects as a result of the lithographic grating definition cause corrugations on the waveguide width, as can be seen on figure 6.4. These effects are stronger for devices with narrower grating-to-waveguide spacing. The edges of the grating teeth are significantly overetched. Width corrugations can result in an amplification of the diffractive effect of the gratings with narrow gaps separating them from the waveguide.

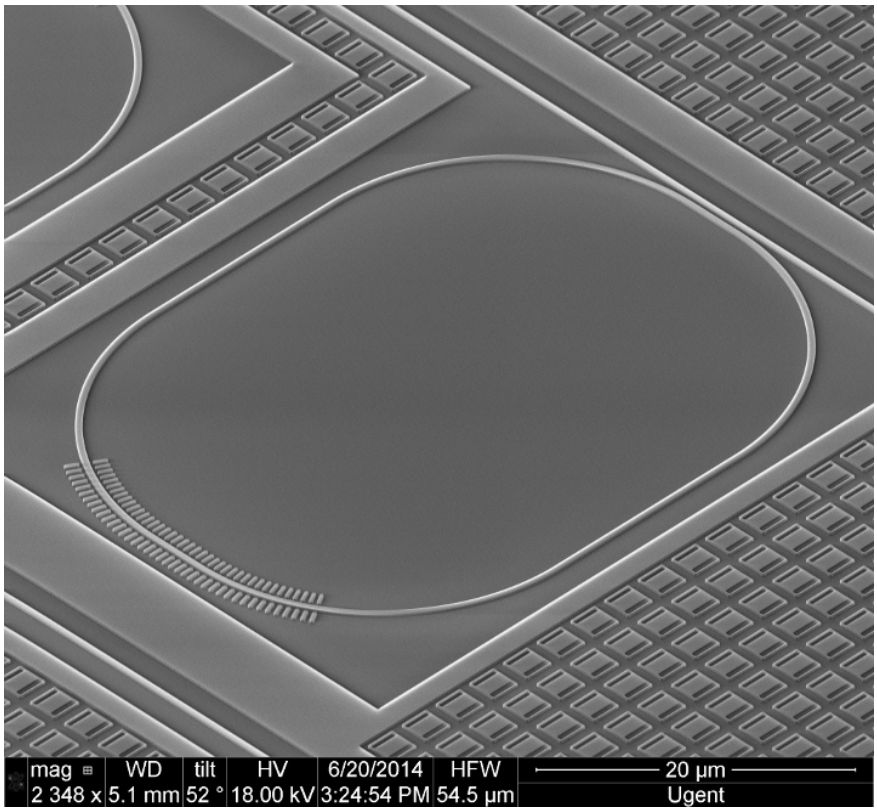

Figure 6.3: SEM-picture of a microring resonator with weak grating in the vicinity of the waveguide.

6.3 Simulations

The microring resonators combined with weak gratings are simulated using the three-dimensional finite-difference time-domain (3D-FDTD) simulation tool Meep3D [10, 11]. For these simulations, a simple model of a silicon wire microring on a buried oxide layer with air as top cladding is used. The very high index contrast allows us to limit the device dimensions which significantly reduces simulation time. The microring has 5 μm bends and a directional coupler section of 2 μm long. We use Harminv [12, 13] to perform a harmonic inversion of the time-dependent field values recorded in the resonator to determine the quality factor of the different resonator modes. By comparing the simulation results to the reference microring without grating, the influence of the weak grating on the resonator mode and the grating-associated losses can be ex-

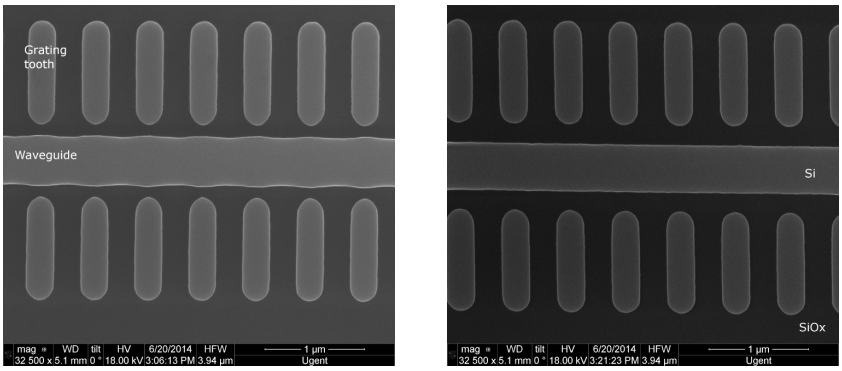

Figure 6.4: SEM-picture of the corrugations on the waveguide width as a result of the grating vicinity for (a) a grating-to-waveguide gap of 130 nm and (b) a grating-to-waveguide gap of 200 nm.

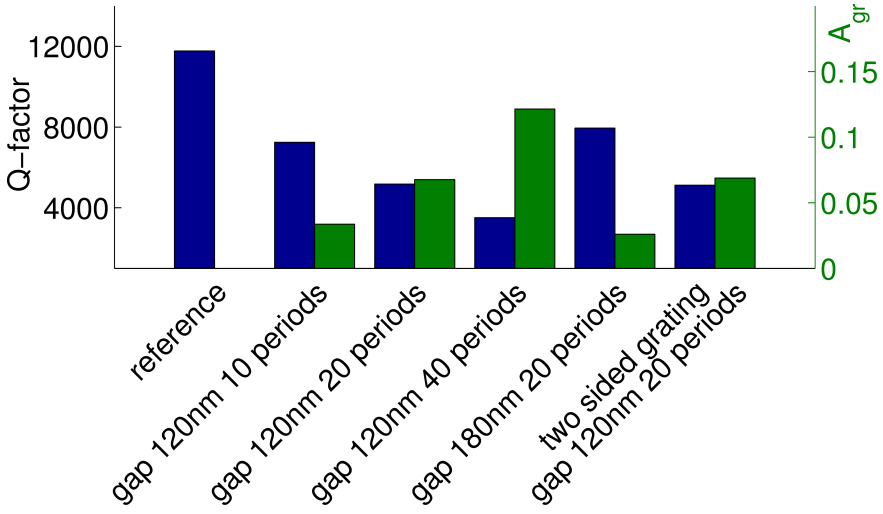

Figure 6.5: Simulated quality factors and grating associated losses for microring resonators with different grating configurations.

tracted. We have simulated the microring with weak grating for different grating lengths and different gaps between waveguide and grating. The influence of a weak grating on both sides of the ring waveguide has also been investigated. The grating loss A_{gr}, which is in fact the only extra loss mechanism after taking into account the reference ring simulation, is defined as $A_{gr} = 1 - \exp(-\alpha_{gr} L)$, with

α_{gr} the attenuation coefficient associated with the grating. The factor α_{gr} can be determined from the simulated quality factors by using the relations (6.3).

$$\frac{1}{Q} = \frac{1}{Q_{ref}} + \frac{1}{Q_{gr}} \text{ and } \frac{\omega}{Q} = \frac{\alpha c}{n_g} \tag{6.3}$$

Here, Q is the simulated quality factor of the microring with grating while Q_{ref} corresponds to the reference situation. ω and n_g are the angular frequency and the group index of the resonator mode, respectively. These results for the resonance around 1550 nm are summarized in figure 6.5. The simulations show a significant effect of the weak grating on the resonator losses, while still maintaining a reasonable quality factor. For a spacing between grating and waveguide of 120 nm, the simulations show the ring losses are increasing linearly with increasing grating length. When the spacing is increased to 180 nm, the resonator losses are significantly reduced, as can be expected by the reduced overlap between the waveguide mode and the grating. If a two sided grating is used, with a second grating placed at the inner radius of the bend in an attempt to increase the outcoupling, we notice only very limited extra losses. This can be explained by the fact that the mode is concentrated at the outer edge of the waveguide in the bend sections. The effect of the grating period on the grating losses has also been investigated. This is simulated for a gap of 120 nm and 20 periods by varying the grating period. The resulting grating losses for the different resonator modes are given in figure 6.6. Increased losses around the theoretical grating wavelength are not visible and only a small reduction in losses is noted for decreasing grating periods. We do see, for a fixed period, an increasing grating loss with increasing wavelength. This can most likely be attributed to the reduced confinement of the waveguide mode for larger wavelengths and consecutive increased interaction with the grating, rather than a wavelength dependency of the grating losses. Although a change in grating period causes a small shift in resonance wavelength. But more importantly, we will demonstrate that the period has an important effect on the diffraction angle of the grating.

Using a commercial-grade simulator based on the finite-difference time-domain method [14], the radiating fields for a microring with a two-sided grating with gap 120 nm and 20 periods of 547 nm are calculated. A near field image of the microring obtained by plotting the real part of the out-of-plane or z-component of the Poynting vector right above the waveguide is given by figure 6.7a. The microring is oriented with the directional coupler section along the x direction and the waveguide with weak grating on the opposite side of the microring, at the top of the image. Figure 6.7a shows a strong increase in power in the region right above the grating, indicating it does act as a diffracting element sending light upward out of the waveguide. By integrating the Poynting vector over the area above the grating, the vertical transmission out of the

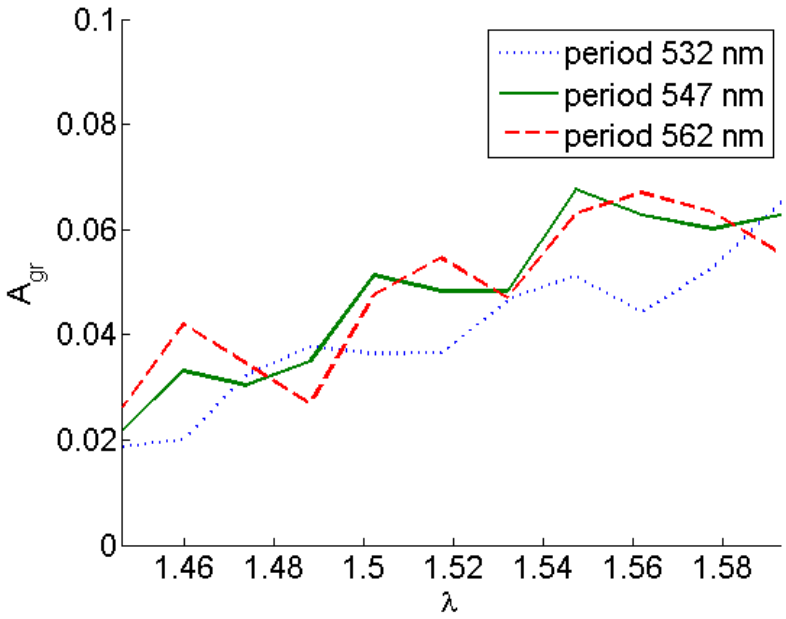

Figure 6.6: Simulated grating losses for varying grating periods. The losses are given as a function of the wavelength of the corresponding resonator mode.

waveguide is depicted in figure 6.7b. The transmission spectrum clearly shows a strong peak around the resonance wavelength of the microring, again showing the grating acts as a drop port to couple light out of the ring vertically. The transmitted power is of the same order of magnitude as the grating losses we obtained using the harmonic inversion method and the Meep3D FDTD simulator.

The far-field response of the grating is also simulated. The resulting projection on the hemisphere 1 m above the two-sided grating is plotted in figure 6.8. The figure shows the intensities of the optical field for the different directions (θ,ϕ), with the propagation of the counterclockwise mode in the waveguide along the negative x direction, or $\phi = 180°$. The majority of the light is emitted in the $\phi = 0°$ direction, at a polar angle θ of approximately 30° from the surface normal. The opening angle along the azimuthal ϕ direction is approximately 60°, which is expected for diffraction from a 450 nm wide waveguide. Wavelength-dependent resonance splitting causes some resonator modes to show an equally strong far-field lobe in the opposite x direction, corresponding to the clockwise mode in the resonator (not shown in the figure). The diffraction

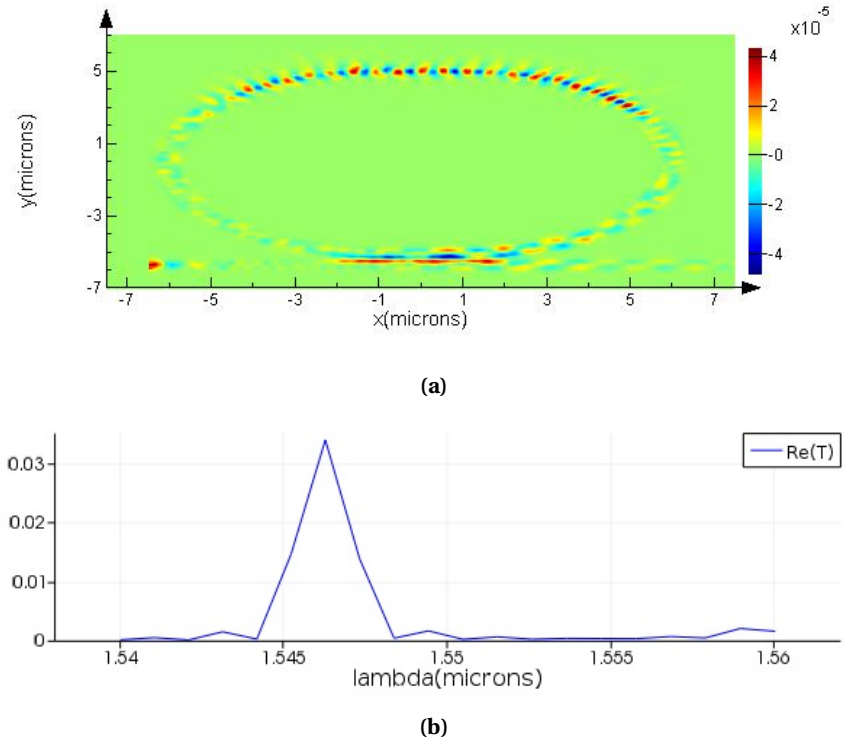

Figure 6.7: (a) Simulated vertical power flux above the microring with weak grating on resonance. The grating region shows an increase in vertically radiated power. (b) The vertical transmission spectrum of the microring obtained by integration the real part of the Poynting over the area above the grating.

angle of 30° differs significantly from the desired angle of 0°.

By adjusting the grating period, we are able to correct the diffraction angle of the grating. Because the assumption of an unchanged propagation constant β results in an overestimation of the diffraction angle by 30°, the required grating period is obtained by substituting an angle of $-30°$ in the Bragg condition 6.1. This results in a grating period $\Lambda = 660\,\text{nm}$. This is verified by simulation and the resulting far-field pattern is given in figure 6.9. For a grating period of 660 nm we find that the diffraction angle of the grating has indeed changed to the vertical direction. However, no devices with this grating period are fabricated for experimental verification.

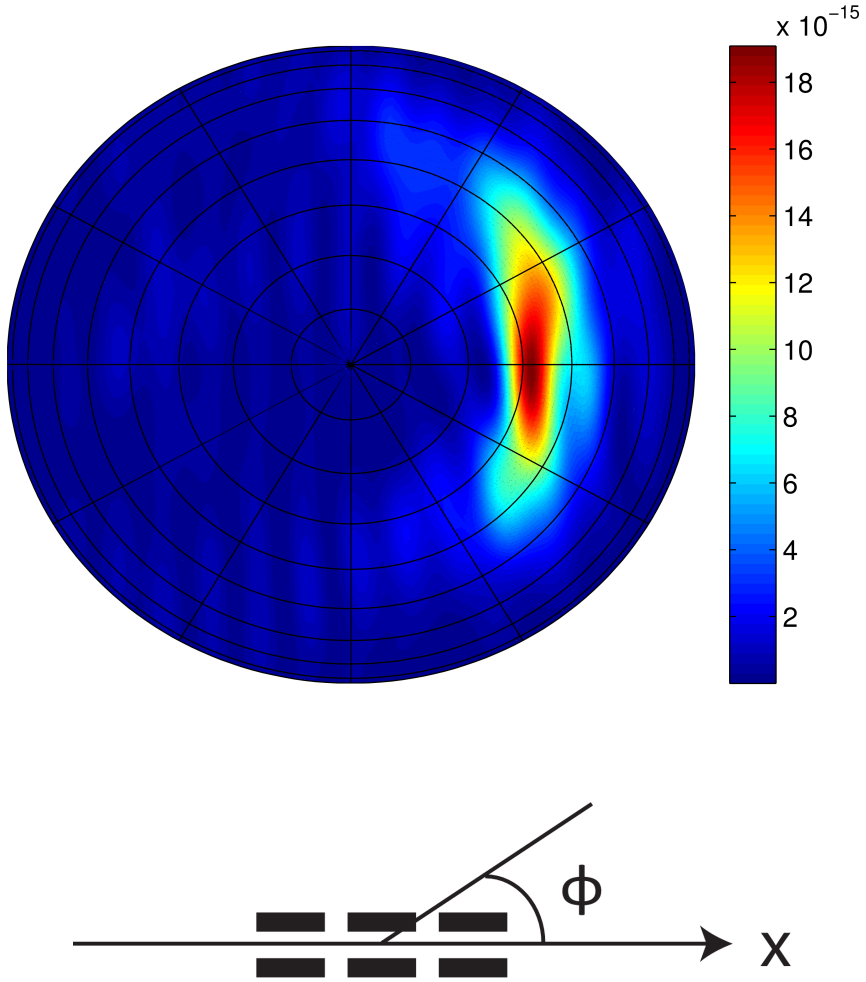

Figure 6.8: Simulated far-field response on the hemisphere above the grating with period 547 nm. The center of the grating coincides with the origin of the coordinate system, as indicated by the schematic top view. Concentric circles represent increments of 10° in the polar angle θ, while radial lines correspond to steps of 30° in the azimuthal angle ϕ. The color scale represents the optical intensity. The highest intensity optical field is found around the direction $\theta = 30°, \phi = 0°$.

6.4 Experiments

For the experimental characterization of the microrings with weak gratings, the devices are clad with silicon oxide. This cladding material approaches the

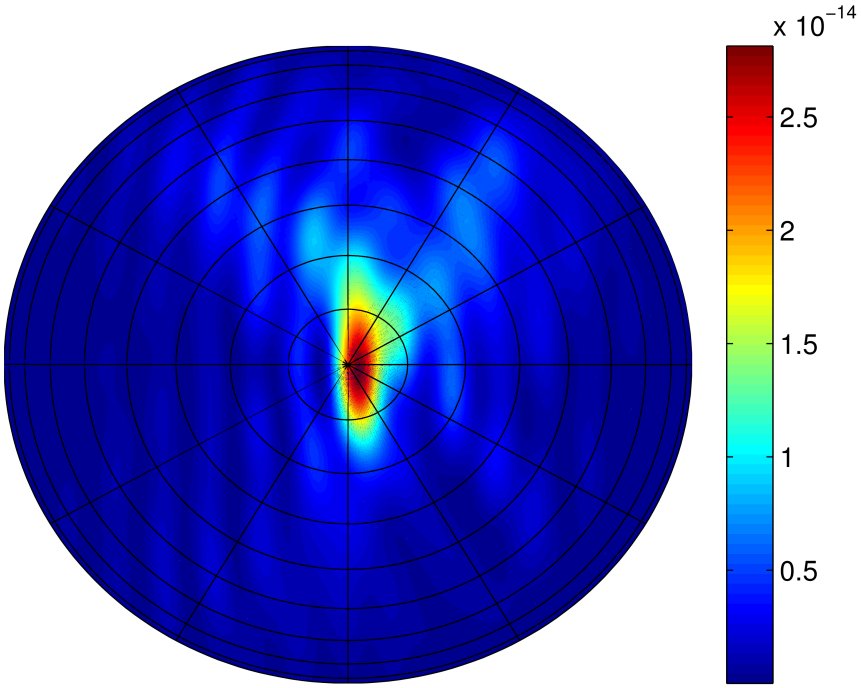

Figure 6.9: Simulated far-field response on the hemisphere above the grating with period 660 nm. Concentric circles represent increments of 10° in the polar angle θ, while radial lines correspond to steps of 30° in the azimuthal angle ϕ. The color scale represents the optical intensity. The highest intensity optical field is found in the vertical direction.

index contrast of a water cladding which will most likely be used in a biomedical sensing application. The microrings consist of silicon wire waveguides of 450 nm with 16 μm bends. The directional coupler with the pass waveguide has a directional coupler spacing of 250 nm and 4 μm-long straight sections. The microrings with gratings are measured in the pass configuration on a vertical fiber setup to obtain the transmission characteristics discussed in section 6.4.1. To monitor the microring directly by recording the light vertically diffracted by the grating, an image of the integrated chip with microring resonators is recorded by a camera. A SEM-picture of the microring with grating that is used for these experiments is shown in figure 6.10. The light emitted from the microring is recorded for two angles. In section 6.4.2, the camera is mounted under an angle of 30° to pick up the grating emission in correspondence with the simulated far-field response. Section 6.4.3 discusses the vertical signature of the grating, for a camera mounted exactly above the microring. Finally, both configurations

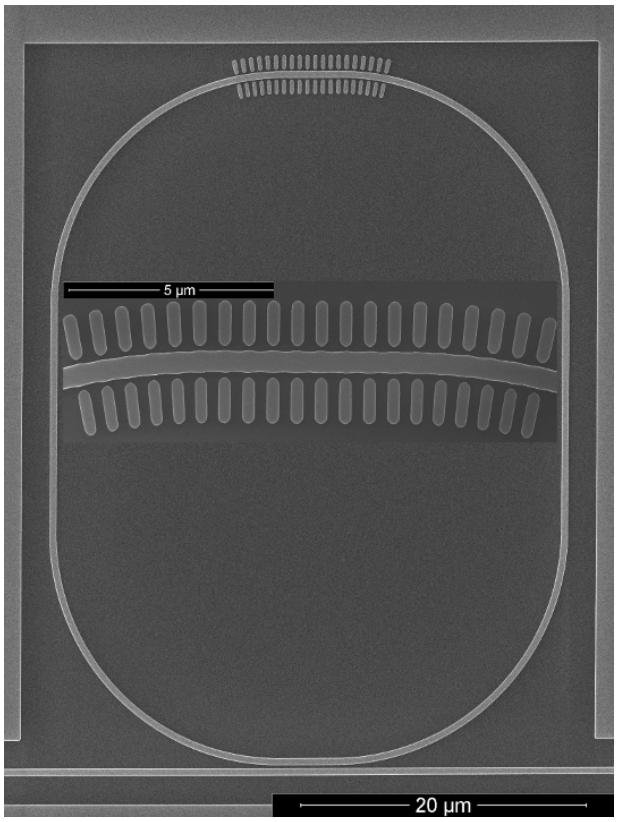

Figure 6.10: SEM-picture of the microring resonator with weak grating in the vicinity of the waveguide. The inset shows a magnification of the grating region. Grating parameters are a gap of 130 nm and 20 periods of 547 nm.

are compared to each other.

6.4.1 Microring transmission on a fiber setup

The fiber-to-fiber transmission of microrings with different grating configurations is recorded on an optical setup. An Agilent 81980A tunable laser is swept over a wavelength range of 60 nm and an Agilent 81635A optical powermeter records the optical power with a 1 pm wavelength resolution. The resulting microring spectra can be used to extract resonance characteristics for different grating configurations such as quality factor and losses by fitting a Lorentzian lineshape to the resonance dips. The round-trip and coupling loss of the micro-

ring resonances can be extracted from the parameters of the Lorentzian approximation for the transmission (6.4).

$$T = \frac{a^2 - 2ar\cos(\phi) + r^2}{1 - 2ar\cos(\phi) + (ar)^2} \tag{6.4}$$

The round-trip loss for a microring resonator with attenuation coefficient α and round-trip length L is represented by the amplitude reduction coefficient $a = \exp(-\alpha L)$, while ϕ equals the round-trip phase change. The directional coupler amplitude self-coupling coefficient $r = \sqrt{1-k^2}$ represents the coupling losses corresponding to a field coupling coefficient k. The method described in [15] returns a set (a,r) and by comparing the behaviour of the solutions for different devices, the trends in a and r can be identified. The resulting a and r of the microring resonators with a weak grating are given in figure 6.11 as a function of wavelength for different grating lengths. The plotted results are for a grating-to-waveguide gap of 130 nm and a grating period of 547 nm with 50% filling factor. The quality factors of the resonances around 1550 nm are indicated in the legend.

The method in [15] can not distinguish a from r, but since the dashed lines do not vary for different grating lengths, they have to correspond to the coupling coefficients. The full lines represent round-trip losses that increase with increasing grating length, which is in good agreement with the simulation results. Broadening of some resonances by resonance splitting results in poorly-fit parameters which causes the particularities in the graph. In general, round-trip and coupling losses increase slightly with increasing wavelength. Changing the period of the fabricated grating does not result in changes in the recorded losses of the resonator mode. For a gap of 200 nm, increasing the grating length no longer has any effect on the losses of the microring resonance. This indicates the grating has only a very limited effect for such large gaps. The quality factor recorded for a resonance around 1550 nm is 23000 for a gap of 200 nm and 20 grating periods of 547 nm, which is indeed significantly higher than the quality factor of 15000 reported in figure 6.11 for a 130 nm gap. Recalling the waveguide corrugations we have noticed on the SEM images in figure 6.4 as a result of fabrication imperfections, we must also consider the possibility that the grating effect in narrow gaps is enhanced by the diffractive effect of the waveguide width variations, which form a grating with the same period.

6.4.2 Grating image for a 30° angle.

A microring combined with a weak grating with a gap of 130 nm and 20 periods of 547 nm as depicted in figure 6.10 is used to experimentally detect the vertical grating diffraction. Figure 6.12 shows the image of the microring with

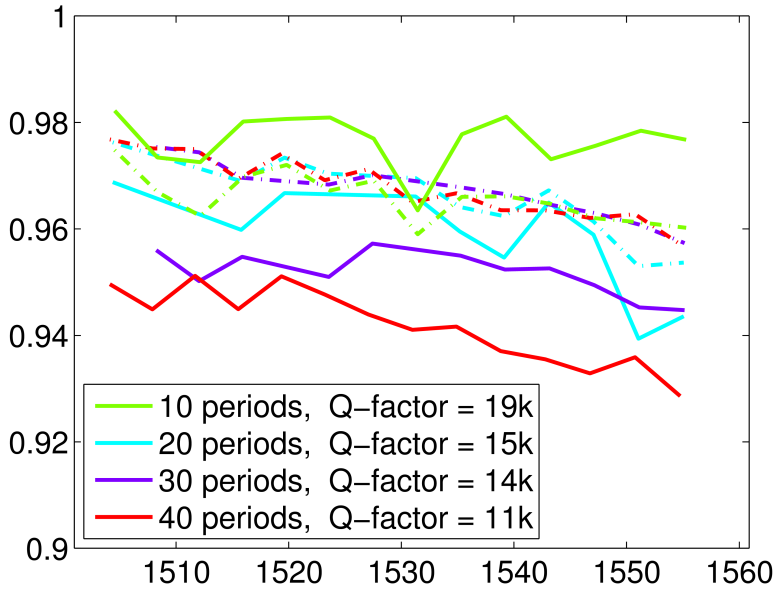

Figure 6.11: Device and wavelength dependent coupling and round-trip loss for microrings with different number of weak grating periods. Dashed lines represent the coupling coefficient r while the full lines show the round-trip amplitude reduction coefficient a. The weak grating periods are 547 nm with 50% filling factor while the waveguide-grating gap is 130 nm.

weak grating on resonance as recorded by a Xenics Xeva-1.7-320 infrared camera mounted on a magnifying objective under an angle of 30°. The numerical aperture of the camera lens is 0.28. The microring grating is imaged on the camera array as a bright spot with some low intensity fringes due to focusing issues. The power integrated over the spot size can be used as a transmission characteristic of the microring. By sweeping a Tunics Plus CL tunable laser and recording the transmission at every wavelength, a spectral response of the microring is obtained. This is represented in figure 6.13. A Lorentzian shape can be fitted to the microring spectrum to obtain the resonance parameters. This results in a resonance quality factor of 20000 at a wavelength of 1523.5 nm, which corresponds very well to the quality factor of 19000 that we obtain for the same resonance by investigating the pass transmission on the vertical fiber setup. This indicates the transmission of the weak grating represents the same resonance of the microring and confirms the ability to record the microring resonance without using

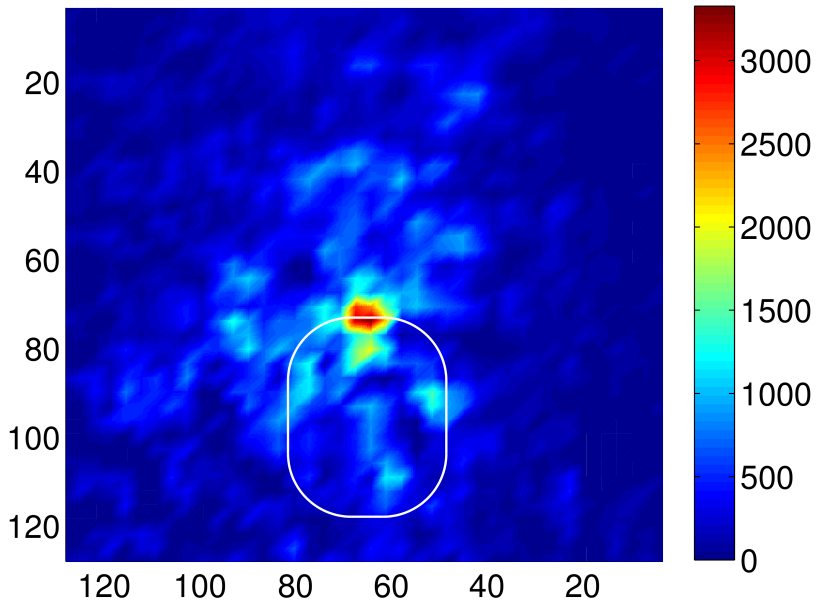

Figure 6.12: Microring and weak grating image as recorded by an infrared camera picking up the emission at 30°. Axes are expressed in μm. The color scale represents the counts per individual pixel.

an output waveguide.

The integrated power on resonance can also be used to estimate the efficiency of this technique to collect the resonant light from the microring. With a reported sensitivity of the Xenics camera of 305 photons per count, we estimate that the power recorded by the camera corresponds to a fraction of $7 \cdot 10^{-5}$ of the power present in the optical bus waveguide. This may seem low, but it is easily picked up by the camera in this proof-of-principle demonstration.

6.4.3 Grating image for a 0° angle.

The vertically emitted light from the microring combined with a weak grating with a gap of 130 nm and 20 periods of 547 nm is again recorded by a Xenics Xeva-1.7-320 infrared camera mounted on a magnifying objective. This time with the camera mounted vertically above the ring. The recorded image is shown in figure 6.14. The shape of the ring can be made out from the image because some light radiates out of the waveguide in the bend sections, but also because of scattering on the rough waveguide edges. The grating region

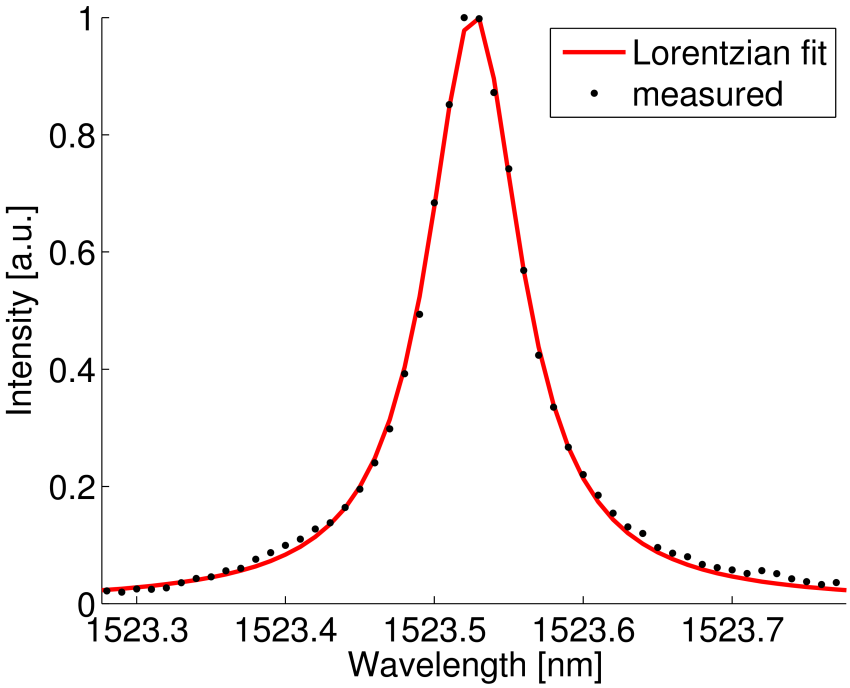

Figure 6.13: Microring spectrum and resulting Lorentzian fit obtained by recording the vertical emission of the grating using an infrared camera.

however, lights up very brightly, with especially bright grating edges. That we indeed monitor the edges is confirmed by imaging microrings with longer gratings, which results in a larger separation of the bright spots. The bright edges suggest the grating effect in the vertical direction is dominated by refractive index scattering on the transitions between the waveguide sections with and without grating. When integrating the total power emitted from the microring on resonance at 1523.5 nm, we obtain an intensity reduction by a factor 7 compared to the setup with a 30° angle. This significant difference in intensity can only be attributed to the fact that the diffracted light does not propagate vertically out of the chip, but under an angle. This is also suggested by the FDTD simulations in section 6.3. However, the vertically scattered power is still considerable. This corresponds to the simulation results where we have noticed that the wavelength dependency of the grating losses is limited to a steadily increasing loss with increasing grating wavelength. Such a behaviour can indeed be explained by refractive index scattering, which is expected to increase in strength if the optical mode is less confined to the waveguide.

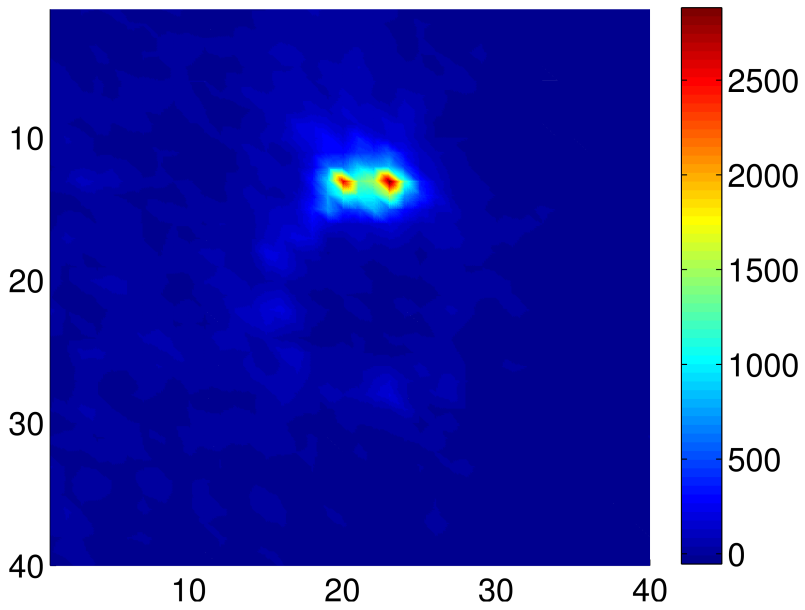

Figure 6.14: Microring and weak grating image as recorded by an infrared camera picking up the emission at 0°, with bright spots corresponding to the grating edges. The color scale represents the counts per individual pixel.

An interesting observation can be made by comparing the signals recorded from the individual bright spots for a split microring resonance. The transmission spectra for the grating edges are given in figure 6.15. We notice the different grating edges show a different spectral response. One grating edge shows significant resonance splitting while the other edge returns a nicely unsplit Lorentzian shape. This difference can be explained by recalling that under split resonance conditions, the unsplit normal modes of the microring resonator are standing waves with slightly different resonance wavelength, depending on their power distribution in the ring. The grating edge that emits a split spectral signal must be at a position in the ring where both normal modes are almost equally strong, resulting in a superposition of both modes and a split characteristic in the scattered light. The second grating edge on the other hand, shows no split spectrum. This means it is located at a node of one normal mode and an antinode of the other normal mode. There is no power present in the node, and only light from a single normal mode is scattered out of the ring, at a single resonance wavelength. This demonstrates the weak grating allows us to

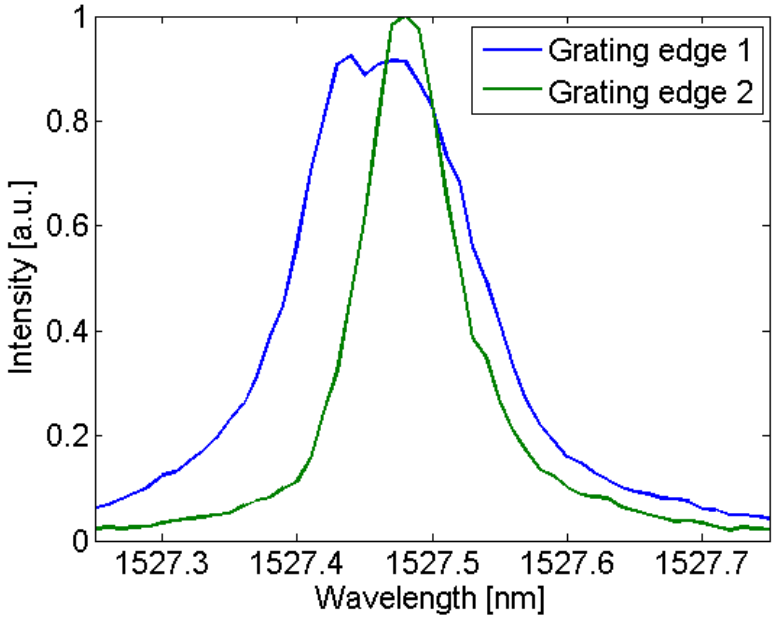

Figure 6.15: Spectral response of the grating edges. One edge shows a clearly split resonance while the other exhibits a Lorentzian shape.

sample the intensity distribution in the microring on a wavelength scale.

6.5 Conclusion

In this chapter we have simulated and experimentally characterized the combination of a microring resonator with a weak grating for direct interrogation of the microring. The effect of different grating parameters is evaluated. Both simulation and experiment show vertical emission from a microring can be achieved, while still maintaining high quality factors of 19000. Simulations show the diffraction angle of the grating can be tuned by adjusting the grating period. Using an infrared camera to collect the diffracted light, the resonance spectrum is recovered. We also show the intensity distribution in the microring can be sampled on a wavelength scale. In future work, the use of similar gratings to couple light both in and out of the microring can be investigated.

References

[1] K. De Vos, J. Girones, T. Claes, Y. De Koninck, S. Popelka, E. Schacht, R. Baets, and P. Bienstman. *Multiplexed Antibody Detection With an Array of Silicon-on-Insulator Microring Resonators*. IEEE Photonics Journal, 1(4):225–235, October 2009.

[2] M. Iqbal, M. A. Gleeson, B. Spaugh, F. Tybor, W. G. Gunn, M. Hochberg, T. Baehr-Jones, R. C. Bailey, and L. C. Gunn. *Label-Free Biosensor Arrays Based on Silicon Ring Resonators and High-Speed Optical Scanning Instrumentation*. IEEE Journal of Selected Topics in Quantum Electronics, 16(3):654–661, 2010.

[3] A. Densmore, D. Xu, N. A. Sabourin, H. Mcintosh, P. Cheben, J. H. Schmid, R. Ma, M. Vachon, A. Delâge, W. Sinclair, J. Lapointe, Y. Li, G. Lopinski, B. Lamontagne, and S. Janz. *A Fully Integrated Silicon Photonic Wire Sensor Array Chip and Reader Instrument*. Optics Express, pages 350–352, 2011.

[4] S. Janz, D. X. Xu, M. Vachon, N. Sabourin, P. Cheben, H. McIntosh, H. Ding, S. Wang, J. H. Schmid, A. Delage, J. Lapointe, A. Densmore, R. Ma, W. Sinclair, S. M. Logan, R. MacKenzie, Q. Y. Liu, D. Zhang, G. Lopinski, O. Mozenson, M. Gilmour, and H. Tabor. *Photonic wire biosensor microarray chip and instrumentation with application to serotyping of Escherichia coli isolates*. Optics Express, 21(4):4623–4637, February 25 2013.

[5] T. T. Torres, M. Metta, B. Ottenwälder, and C. Schlötterer. *Gene expression profiling by massively parallel sequencing*. Genome research, 18(1):172–7, January 2008.

[6] A. Samarelli, A. Canciamilla, G. Morea, F. Morichetti, R. D. L. Rue, A. Melloni, and M. Sorel. *Grating-assisted micro-ring resonators for silicon dual mode filters*. In CLEO/Europe and EQEC 2011 Conference Digest, pages 1–1. Optical Society of America, 2011.

[7] S. Iijima, Y. Ohtera, and H. Yamada. *High-Q microdisk resonator having sub-wavelength grating on its sidewall*. In 2013 Conference on Lasers and Electro-Optics Pacific Rim (CLEO-PR), pages 1–2, June 2013.

[8] C. Qiu and Q. Xu. *Controlling normal incident optical waves with an integrated resonator*. Optics Express, 19(27):26905–26910, Dec 2011.

[9] http://www.epixfab.eu/. 2014.

[10] A. Oskooi, D. Roundy, M. Ibanescu, P. A. Bermel, J. D. Joannopoulos, and S. G. Johnson. *Meep: A flexible free-software package for electromagnetic simulations by the FDTD method*. Computer Physics Communications, 181(3):687–702, 2010.

[11] www.ipkiss.org/www.lucedaphotonics.com. 2014.

[12] http://ab-initio.mit.edu/wiki/index.php/Harminv. 2006.

[13] H. S. Taylor and V. A. Mandelshtam. *Harmonic inversion of time signals.* J. Chem. Phys., 107(17):6756–6769, 1997. Erratum, *ibid*, vol. 109, no. 10, pp. 4128, 1998.

[14] http://www.lumerical.com/tcad-products/fdtd/. 2014.

[15] W. R. McKinnon, D. X. Xu, C. Storey, E. Post, A. Densmore, A. Delâge, P. Waldron, J. H. Schmid, and S. Janz. *Extracting coupling and loss coefficients from a ring resonator.* Optics Express, 17(21):18971–82, October 2009.

7 Conclusions and perspectives

7.1 Conclusions

Silicon-on-insulator microring resonators have proven to be an excellent candidates for photonic biosensor transducers. Their applicability in multiplexed label-free assays has led to a variety of applications, especially in the field of antibody or protein detection. In this work, we have investigated and optimized a microring resonator platform for the application in DNA detection. A label-free microring resonator has many advantages in this field. It can provide real-time information on the binding kinetics of a DNA sequence to a probe on the sensor surface. Quantitative concentration information can also be obtained from a detection event. An additional advantage of label-free detection in lab-on-a-chip applications in the reduction of reagents and assay steps. This significantly simplifies the chip layout and reduces the costs. The silicon-on-insulator technology also allows easy integration of the sensor microarray with microfluidics and readout equipment.

The multidisciplinary character of the topic is apparent from chapter 3, where we describe how different technical fields are combined to create a successful sensor platform. The optical setup, microfluidic integration and measurement software are discussed. The chemical modifications to the chip surface that enable complementary DNA detection are also described and DNA detection experiments are reported. We successfully detect complementary

DNA sequences down to a 1 nM concentration. This is the same order of magnitude as the lowest detected concentration using label-free microrings reported in literature. By considering a series of different concentration measurements and the noise floor of the setup, we extrapolate an experimental detection limit as low as 0.2 nM.

To ensure robust performance with tolerant alignment requirements, the optical signals reach the sensor array by coupling a collimated laser beam into the optical waveguides using vertical grating couplers. This relaxes the design requirements and cuts the costs of the readout instrument. A drawback of this light coupling technique are the parasitic light paths that induce unwanted interferences in the optical signals, compromizing the performance of the optical sensors. In chapter 4, we describe the design of anti-transmission gratings to block these parasitic light paths. By implementing a high-contrast reflection grating, the parasitic light is reflected on the chip surface which results in a suppression up to 20 dB over a wavelength range of more than 20 nm.

While silicon-on-insulator offers many of the key advantages for microring resonator transducers, it also comes with a significant drawback. The high index contrast between the waveguide core and cladding regions makes the optical mode sensitive to waveguide imperfections that cause reflections. The backreflection of optical power enables a coupling between counterpropagation modes in the microring resonator, which results in splitting of the resonances. A split resonance significantly deteriorates the shape of the resonance spectrum, which has a negative effect on the performance of the ring. Not only in sensing, but for all applications that require consistantly narrow resonances. The integrated interferometric circuit introduced in chapter 5 gives access to the high-quality normal modes of the resonator, which results in a reduction of the width in the output signal by a factor of 3.

Because of their small size, ring resonator sensors are very suited to create highly multiplexed microarrays. However, for applications that require massive parallelization of the detections, the grating couplers and waveguide routing on the optical chip start taking up too much chip surface to be practically feasible. To circumvent this limitation, we have investigated the combination of microring resonators with gratings to couple light directly from the microring. By limiting the interaction between the grating and the optical mode, the diffracted power is limited and the resonances maintain the high quality factors required for sensing. We demonstrate the vertically emitted power from the ring is easily picked up by an infrared camera and the resonance spectrum can be recorded without using output waveguides and grating couplers.

7.2 Perspectives

In this work, it was demonstrated that implementing reference sensors to eliminate collective effects like bulk index changes or temperature oscillations, provides the most stable sensor signals. Chemical passivation of the reference sensors by coating their surface with molecules such as PEG or BSA should be investigated in future work, because a cladding with a polymer such as BCB results in slowly drifting reference signals. These chemical functionalizations should also be investigated for the reduction of non-specific signal of the DNA detection sensors. After immobilization of the receptors, the non-specific adsorption to the sensor surface is still too strong for implementation of the sensors in practical applications. Also in view of signal amplification using streptavidin coated beads, the non-specific interaction between the beads and the surface has to be eliminated to ensure only specific binding events amplify the DNA duplexes on the surface.

To achieve the DNA detection limits required for practical applications that demand a yes or no answer, like antibiotics resistance screening, detection limits beyond 100 pM are required and the current label-free detection is not sensitive enough. To establish an experimental detection limit for complementary sequence detection using microring resonator sensors, signal amplification by labelling has to be investigated. Although it remains to be seen if the limit of detection improvement can be sufficiently strong to offer an advantage over fluorescently labelled microarrays. At the same time, the field of microfluidics is still under development and it is not unimaginable that future developments in microfluidics relax the requirements for the detection array. In that case, label-free detection with microresonators could still become competitive to perform highly sensitive DNA assays. In applications that require the monitoring of transient nucleotide reactions on the surface, the microring resonator already has a key advantage over labelled microarray assays.

For future microarray designs, the high-contrast gratings described in this work should be implemented together with the grating couplers to eliminate parasitic signals and improve the sensor performance. To open the possibility of massive mutliplexing using thousands of microrings on a single chip, it would also be interesting to continue the research into direct microring coupling using a local grating. When light can be collected from the microring using the local grating, it is fair to assume the grating can also be used to couple light into the ring. Although this is someting that should still be demonstrated experimentally.